TR diss 2193 S

Stellingen

behorende bij het proefschrift

Calculation and Control of Heat Transfer in Injection Moulding

1 Niet de afstand vanaf de aanspuiting maar de afstand tot het einde van de vloeiweg is de relevante parameter voor de hoeveelheid ingevroren oriëntatie in een spuitgietprodukt.

2 'Constrained quenching' van een 'elastic-solid' materiaal veroorzaakt geen thermisch geïnduceerde restspanningen.
Paragraaf 4.4 van dit proefschrift.

3 Het vermelden van Melt Index en kerfslagwaarde (Izod, Charpy) in verkoopbrochures van kunststofleveranciers moet worden tegengegaan.
J.L.S. Throne (1979), Plastics Process Engineering, p.288.

4 De beste methode om een heterogene kunststofafvalstroom te herverwerken is vooralsnog via pyrolyse.

5 Er bestaat een bewijs dat: $2M(\frac{1}{3},\frac{2}{3},z).M(\frac{5}{3},\frac{4}{3},z) - M(\frac{2}{3},\frac{4}{3},z).M(\frac{4}{3},\frac{2}{3},z) = e^{z}$, waarin de Kummerfunktie $M(a,b,z)$ gedefiniëerd is als in Abramowitz en Stegun (1972) en $z \in \mathbb{C}$.

6 De lengte van een vertaalde tekst is omgekeerd evenredig met de mate waarin de vertaler de doeltaal beheerst.

7 Het is moreel niet verantwoord verzekeringsmaatschappijen zelf hun verzekeringsvoorwaarden te laten vaststellen.

8 Het verbieden van het nasynchroniseren van tv-programma's zal de kulturele integratie in Europa ten goede komen.

9 Ambtelijk taalgebruik mag geen geheimtaal worden (zie b.v. de tekst in het rijbewijs deel B).

10 Hoe korter de stelling hoe beter.

Kaspar Jansen

Delft, 15 maart 1993.

571744
3176207
TR diss 2193

TR diss
2193

CALCULATION AND CONTROL OF HEAT TRANSFER IN INJECTION MOULDING

The work described in this thesis was part of the IOP PCBP program of the Dutch Ministry of Economic Affairs.

Front cover: Measured orientation distribution in injection moulded polystyrene strip;

Back cover: Orientation distribution after a heating pulse of two seconds.

CALCULATION AND CONTROL OF HEAT TRANSFER IN INJECTION MOULDING

BIBLIOTHEEK TECHNISCHE UNIVERSITEIT
DELFT

PROEFSCHRIFT

ter verkrijging van de graad van doctor
aan de Technische Universiteit Delft,
op gezag van de Rector Magnificus,
prof. drs. P.A. Schenck,
in het openbaar te verdedigen
ten overstaan van een commissie
aangewezen door het College van Dekanen
op maandag 15 maart 1993 te 14.00 uur

door

KASPAR MARIA BONAVENTURA JANSEN,

scheikundig Ingenieur,

geboren te Oss

Dit proefschrift is goedgekeurd door

promotor:

Prof. dr. ir. A. Posthuma de Boer

overige leden:

Prof. Dr. H. Janeschitz-Kriegl (Universität Linz)
Prof. dr. ir. C.J. Hoogendoorn (TUD)
Prof. dr. ir. L.C.E. Struik (Universiteit Twente)
Prof. dr. ir. H.E.H. Meijer (Technishe Universiteit Eindhoven)
Dr. ir. A.A.M. Flaman (Philips Eindhoven)
Dr. ir. J. van Dam (TUD)

Published and distributed by:

Delft University Press
Stevinweg 1
2628 CN Delft
The Netherlands

Telephone +31 15 783254
Fax +31 15 781661

ISBN 90-6275-868-1 / CIP

Copyright © 1993 by K.M.B. Jansen

All rights reserved.
No part of the material protected by this copyright notice may be reproduced or utilized in any form or by any means, electronic or mechanical, including photocopying, recording or by any information storage and retrieval system, without permission from the publisher: Delft University Press, Stevingweg 1, 2628 CN Delft, The Netherlands.

Printed in The Netherlands

Aan Alice

CONTENTS

LIST OF SYMBOLS *xi*
LIST OF PUBLICATIONS *xiii*

1 INTRODUCTION 1
1.1 Scope and outline of this thesis 1
1.2 Injection moulding process and product properties 2
    1.2.1 The moulding process 2
    1.2.2 Process-properties relationships 4
1.3 Literature review on temperature control in injection moulding 7
1.4 The energy equation 9

2 HEAT TRANSFER IN QUIESCENT MELT LIMIT 15
2.1 Maximum growth of solidified layer 15
    2.1.1 Fixed wall temperature 15
    2.1.2 Effect of contact temperature between melt and mould 17
2.2 Effect of an insulation layer on cooling 18
    2.2.1 Initial cooling stage 18
    2.2.2 Further cooling and moment of solidification 21
    2.2.3 Solidified layer thickness 23
2.3 Effect of an external heating source on cooling 24
    2.3.1 Heating stage 24
    2.3.2 Effect of boundary conditions 27
    2.3.3 Cooling after heating 28
    2.3.4 Comparison with numerical calculations 28
    2.3.5 Solidified layer thickness with heating 30
Appendix A: Solution of $\beta \tan\beta = Bi$ 31

3 TEMPERATURE DURING AND AFTER FLOW 33
3.1 Stationary temperature during filling 33
    3.1.1 Convection-conduction contribution 34
    3.1.2 Viscous dissipation part 35
    3.1.3 Comparison with core flow solution and numerical solution 37
    3.1.4 Position of maximum temperature and solidified layer boundary 41
    3.1.5 Other heat sources (compression and chemical reaction) 43
    3.1.6 Other geometries (pipe flow and divergent flow) 44
    3.1.7 Conclusion 49
3.2 Instationary temperature during filling 50

3.2.1 Classical instationary models 50
3.2.2 Semi-instationary model 51
3.2.3 Solidified layer thickness prediction 53
3.2.4 Comparison with measurements 55
3.3 Temperature after filling 57
3.3.1 Temperature profile and cooling time 57
3.3.2 Solidified layer thickness 58
Appendix B: Perturbation solution of the diffusion equation 59

4 EFFECT OF TEMPERATURE ON ORIENTATION AND FROZEN-IN STRESSES 65
4.1 Introduction 65
4.1.1 A short note on orientation and stresses 66
4.2 Effect of heater on orientation relaxation 66
4.2.1 Relaxation model 66
4.2.2 Predictions and discussion 70
4.3 Thermal stresses (constant pressure) 73
4.3.1 Stress calculation 73
4.3.2 Warpage due to asymmetrical cooling 75
4.4 Pressure-induced stresses in injection moulded products 77
4.4.1 Stress calculation 77
4.4.2 Warpage due to asymmetrical cooling 85

5 REDUCTION OF FROZEN-IN ORIENTATION AND RESIDUAL STRESS 87
5.1 Heater design 87
5.2 Verification of heating curves 90
5.3 Injection moulding experiments 94
5.3.1 Material data and characterization 94
5.3.2 Injection moulding machine and mould geometry 98
5.3.3 Processing conditions 99
5.3.4 Moulding experiments with heater 102
5.4 Orientation measurements 108
5.4.1 Birefringence contributions 108
5.4.2 The different components of the birefringence tensor 109
5.4.3 Sample preparation and measurement technique 112
5.4.4 Orientation perpendicular to flow direction 113
5.4.5 Orientation distribution with passive layer 116
5.4.6 Orientation distribution with active heater 116
5.4.7 Interpretation of the results 122
5.5 Stress measurements 124

5.5.1 The Layer-Removal technique 124
5.5.2 Effect of heating element on stress distribution 127

6 GENERAL CONCLUSIONS 131
6.1 Conclusions concerning heat transfer models 131
6.2 Conclusions concerning effects of processing historry on product quality 132
6.3 Conclusions concerning experimental results with heating elements 132
6.4 Checks for numerical models 134

LITERATURE 136
SUMMARY 140
SAMENVATTING 142
CURRICULUM VITAE 144
DANKWOORD 146

LIST OF SYMBOLS

a	thermal diffusivity, $\lambda/\rho c_p$ [m^2/s]
a_1	$\partial\tilde{T}/\partial\hat{x}$ at the wall ($\hat{x}=0$)
A	rate of surface change (§3.1.6)
b	heat penetration coefficient, $\sqrt{\lambda\rho c_p}$
Bi	Biot number; thermal resistance ratio, R_{23}/R_1
Br	Brinkman number, see section 1.4
C	a constant
c_p	specific heat [J/kgK]
D	channel half-thickness [m]
D_i	thickness of layer i [m]
D_s	solidified layer thickness [m]
E	modulus of elasticity [Pa]
Gz_m	$v_{max}D^2/aL$, Graetz number
h	heat transfer coefficient [W/m^2K]
K_i	$(D_i/D_1).\sqrt{a_1/a_i}$
L	channel length [m]
M	(bending) moment
Nu	Nusselt number, hD/λ
N_h	heater number, $P_AR_{23}/(T_m-T_w)$
$O()$	is of order ...
P	pressure [Pa]
P_A	Power per unit area [W/m^2]
Q	dimensionless heater source, P_AR_2/T^*
r	radial coordinate [m]
R	radius (of pipe or curvature) [m]
R_i	thermal resistance, D_i/λ_i [W/m^2K]
R_{23}	R_2+R_3
s	transformed axial coordinate [m^2]
$\tilde{t}$	dimensionless time, a_1t/D_1^2
T_L	temperature due to passive layer [K]
T_h	temperature rise due to heater [K]
T_{in}	initial melt temperature [K]
T_w	initial wall temperature [K]
T^*	typical heater temperature rise, P_AR_{23}
$\tilde{T}_L$	dimensionless T_L, $(T_L-T_w)/(T_m-T_w)$
$\hat{T}_h$	dimensionless heater temperature, T_h/T^*
v_z	axial velocity [m/s]
W	channel half width [m]
$\tilde{x}_i$	dimensionless thickness coordinate, x_i/D_i
$\hat{x}$	$1-\tilde{x}$
$\tilde{z}$	dimensionless axial coordinate, z/L
$\hat{z}$	$\tilde{z}/Gz_m$

	Greek symbols
α	$1/\nu + 1$
α_v	volumetric expansion
β_n	eigenvalues
$\dot{\gamma}$	shear rate [1/s]
ε	small parameter
ε_{ij}	$(b_i-b_j)/(b_i+b_j)$
$\mathcal{E}$	$(1-\varepsilon_{31})\varepsilon_{43}$
$\vartheta(\chi)$	temperature function
κ	curvature [m^{-1}]
λ	thermal conductivity [W/mK]
μ	viscosity [Pa.s]
μ_0	consistency index [$Pa.s^{\nu}$]
ν_p	Poisson constant
ν	power-law exponent
ρ	density [kg/m^3]
σ_{xx}	elongation stress [Pa]
σ_{xz}	shear stress [Pa]
σ_{ij}	b_i/b_j (Ch.2, 3)
$\phi(\chi_i,\Omega)$	function in §2.3
τ_R	relaxation time [s]
χ	similarity variable (Ch.3)
χ_i	$K_i\hat{x}_i/2\sqrt{\tilde{t}}$ (§2.3)
ω	divergence angle
Ω	$Bi^{-1}(1+\sigma_{14})\sqrt{\tilde{t}}$ (§2.3)
	superscripts
tf	end of filling
t	transient
t∞	stationary
x∞	core flow (Ch.3)
	subscripts
1	layer 1, polymer
2	layer 2, heater
3	layer 3, insulation
4	layer 4, mould
c	contact
h	heater
in	initial
ℓ	left side
L	layer
m	max
P	pressure induced
r	relaxation
𝓇	right side
s	solidification
T	Thermally induced
v	volume(etric)
w	wall

LIST OF PUBLICATIONS

1 Jansen KMB and Flaman AAM (1991), Injection moulding with thin heating elements, Proceedings of the European PPS meeting in Palermo, Italy

2 Jansen KMB and van Dam J (1992), An analytical solution for the temperature profiles during injection molding, including dissipation effects, Rheol Acta 31:592-602

3 Jansen KMB and Flaman AAM (1992), Reduction of orientation in injection moulded products, Proceedings of the ATPS third AIM conference on advanced topics in polymer science, Gargnano Italy

4 Jansen KMB and Flaman AAM (1992), Reduction of orientation in injection moulded products by means of fast heating elements, Part 1: Heater construction, Nat.Lab. technical note 174/92

5 Jansen KMB and Flaman AAM (1992), Reduction of orientation in injection moulded products by means of fast heating elements, Part 2: Injection moulding experiments, Nat.Lab. technical note 175/92

6 Jansen KMB (1993), Heat transfer in injection moulding systems with insulation layers and heating elements, Int J Heat Mass Transfer (Submitted for publication)

7 Jansen KMB and Flaman AAM (1993), Construction of fast response heating elements for injection moulding applications, Polym Eng Sci (accepted for publication)

8 Jansen KMB and Flaman AAM (1993), The influence of surface heating on the birefringence distribution in injection moulded parts. Polym Eng Sci (accepted for publication)

9 Jansen KMB and Flaman AAM (1992), Reduction of orientation in injection moulding, Proceedings of the regional PPS meeting for the Americas, Knoxville

10 Jansen KMB (1993), Effect of geometry on steady state heat transfer for laminar flow of power law fluids, Rheol Acta (submitted for publication)

11 Jansen KMB (1993), Residual stresses in quenched and injection moulded products, Intern Polym Processing (submitted)

CHAPTER 1

INTRODUCTION

1.1 Scope and outline of this thesis

Injection moulding is a flexible production technique for manufacturing complex shaped, thin walled polymer products, such as boxes, buckets, crates and computer housings. Originally, injection moulding was used to manufacture simple products upon which no high demands were made with regard to mechanical properties. In the last decade, however, there is a tendency to mould more complex products with high demands for dimensional accuracy, optical and mechanical properties (e.g. optical lenses, compact disks and small gear wheels). It then turned out that plastic materials differ from conventional construction materials such as metal and concrete, in the sense that the shaping process itself has a considerable influence on the properties of the finished part. At first, this was insufficiently recognized, often leading to undesired deformations and premature rupture of plastic products. The key issue of these problems is the combination of fluid flow and heat transfer, occurring during the filling of the product cavity.

The aim of this thesis is therefore to understand and, if possible, control the heat transfer during the moulding process.

The understanding of the heat transfer is done by seeking representative analytical solutions rather than developing a, more flexible, numerical model. Such analytical solutions are assumed to provide more understanding in the scaling behaviour of the most important physical quantities and enable rapid calculations in special cases. Therefore they may prove a helpful tool in product optimization. In addition, analytical solutions can serve as a guide for writing and testing numerical programs.

Outline of the thesis

The structure of this thesis is simple. First, the principles of the injection moulding process and its effects on the product properties are given. This is followed by a literature survey on the modification of heat transfer in injection moulding. This first chapter is concluded with a discussion about the energy equation, used in chapters 2 and 3 to calculate temperature distributions in various limiting cases. Special attention will be paid to the derivation of solidification isotherms from the temperature distributions, since these prove to be important in obtaining process-properties relationships. The complexity of the solutions in chapters 2 and 3 gradually increases. First, in chapter 2, the quiescent melt limit is considered and used to predict the effect of coatings and heating elements on the temperatures in the polymer part. Then, in chapter 3, the heat transfer in combination with fluid flow is studied. The solutions for the stationary case, obtained in section 3.1, are used in section 3.2 and 3.3 to investigate the instationary effect during and after filling. Furthermore, in paragraph 3.1.6 it is shown how the solutions obtained for the flow in a simple rectangular channel, can be adapted for other geometries (pipe flow, disk flow and diverging flow).

The knowledge of the heat transfer, gained in chapters 2 and 3, is used in chapter 4 to estimate the effect the processing conditions on frozen-in orientation and stresses. As an example, in section 4.4 the warpage of an inhomogeneously cooled injection moulded product will be calculated.

Next, in chapter 5, a new type of heating elements is developed and used to study their effect on the frozen-in orientation and stress distributions.

In chapter 6 a few concluding remarks and recommendations are given. Finally, a few, relatively simple, tests are given, which are useful for checking the heat transfer part of numerical programs.

1.2 Injection moulding process and product properties

1.2.1 The moulding process

The two essential components of an injection moulding machine are the injection unit and the mould system. The injection unit consists of a heated barrel with a screw inside (see fig.1.1). This screw can both rotate and move as a plunger. The mould usually consists of two halves, which are clamped together during the moulding process. In order to generate the high clamping pressures, necessary to prevent leakage of the polymer melt, a large and complex clamping unit is needed. For a more detailed description of the mechanical construction of injection moulding machines, the reader is referred to e.g. Johannaber (1985) or Throne (1979).

In this thesis we will focus on what happens to the plastic material during the moulding process, rather than on the moulding machine itself. The moulding process essentially involves the following sequence of operations:

i) Plasticization of the polymer. The raw material is fed into the heated barrel, where it is melted, pressurized and mixed to form a homogeneous melt with uniform temperature. During the plasticization stage the screw rotates and moves backwards.

ii) Injection of the polymer melt (see fig.1.1). The screw moves forward like a plunger and forces the melt into the cavity where it solidifies upon cooling. During this injection stage the polymer undergoes simultaneous mechanical and thermal treatment, which has serious consequences for the properties of the finished part (see paragraph 1.1.2).

iii) Holding stage. Once the mould is filled, the material is held under pressure in order to compensate for shrinkage. In this stage sometimes some additional melt is added in the cavity. The velocity of the additional flow is usually much smaller than the filling velocity and stops completely as soon as the delivery channel (the runner) or the gate freezes off.

iv) Further cooling and ejection. The solidification process continues until the product is rigid enough to be ejected. In this stage the melt pressure decreases due to thermal contraction.

v) After complete solidification the cavity opens and the product is ejected.

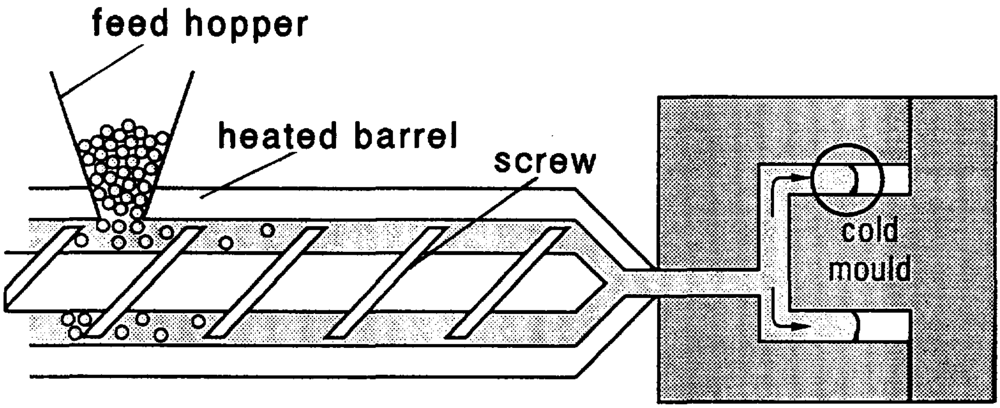

fig.1.1: Schematic representation of the filling stage during injection moulding .

As was said before, in injection moulding the process has a rather large influence on the product quality. The subject of the next paragraph is therefore to provide a general overview of how the different processing operations interfere with the properties of the as-moulded product.

1.2.2 Process-properties relationships

The fact that part of the processing history is reflected upon the product properties is mainly due to the visco-elastic nature of the polymer melt. The molecules "remember" what happened to them in the past. This memory is strongly temperature dependent. At temperatures far above the melting temperature the molecules soon loose their memory, whereas below the melting temperature the past history is effectively "frozen-in". Because of these considerations the processing history in the injection unit (high temperatures) is not very important and most analyses start when the melt enters the cold cavity and the cooling process begins. However, before discussing the effects of this cooling process on the product properties, we need to specify what we mean with "product properties" or the "quality of a product".

Practical injection moulders often talk about the quality of an injection moulded part when referring to a certain set of requirements (such as surface roughness, rupture strength and dimensional stability) which apply for one specific product. Clearly, a general definition of what is exactly understood by product quality is impossible.

Here we will mainly pay attention to the *mechanical and optical properties* of injection moulded products. These are conveniently characterized by three parameters, being (Wimberger-Friedl 1991):

A) the state of orientation;
B) the state of stress;
C) the state of density.

It is important to distinguish between "orientation" and "stresses". Orientation only provides information about the direction of preference of the molecules, whereas stress refers to the forces acting upon a group of molecules (see also Chapter 4). An (unloaded) polymer fiber, for example, is usually strongly oriented and (almost) stress free, while a loaded glass fiber is not oriented and under tensional stress.

Once the three states are known, it is possible to accurately predict the response of a product to e.g. ageing or an imposed loading situation. One should be aware that ageing (changes in the state of a moulded part with time) always occurs. Below the solidification temperature, however, these changes occur at a large time scale. Thus the state of an as-moulded part (viz. just after the moulding process) can be considered as a first indication of the properties during its product life. Obviously, such ageing predictions are not trivial and require thorough investigation. Since it is not the objective of this thesis, we will leave this for future researchers and concentrate on the relations between the moulding process and the as-moulded state. These relations are depicted schematically in fig.1.2 (upper part) and will be discussed below.

Formation of inhomogeneous orientation distribution

The shear (and elongational) flow, present during the injection and holding stage, tends to orient (stretch) the individual polymer molecules. This orientation process is counteracted by the thermal movement of the chain segments (entropic force). In essence, it is this interaction between the force of the flow field (contribution A_1 in fig.1.2) and the temperature dependent relaxation (A_2) which determines the state of frozen-in orientation. Measurements of the orientation distribution (see Chapter 5 and e.g. Wales 1972) typically show two maxima near the product surface and a low orientation level in the product center. The (first) surface peak is due to the elongational flow at the flow front (fountain effect). This effect is confined to a zone of about 50 μm below the surface. The second peak (200-300μm below the surface) is due to the effect of the solidifying layer on the shear stress. The orientation level in the product center is low, both because there the shear stresses vanish and because the orientation relaxation is strongest (highest temperatures).

In addition to this so called "flow-induced orientation" also a small contribution due to the formation of stresses is frozen-in (A_3). The existence of such a "stress-induced orientation" contribution was only recently demonstrated by Wimberger-Friedl (1991).

Stress distribution

In a fast cooling polymer melt large thermal stresses develop. If shrinkage is not prevented this may lead to a residual thermal stress distribution which is compressive at the surface and tensile in the interior (contribution B_1; e.g. Struik 1990, Isayev 1987).

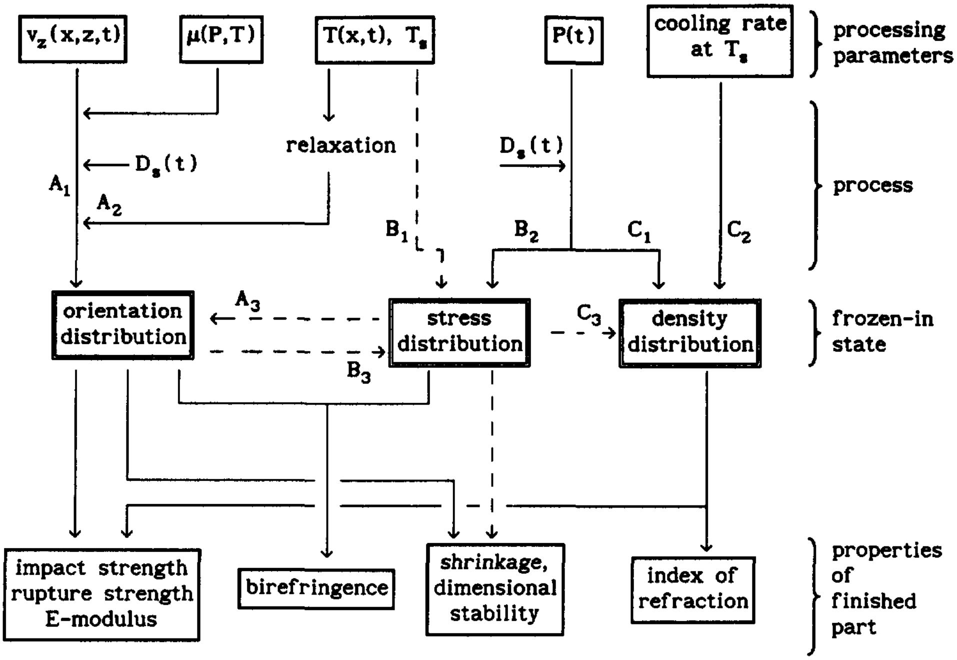
$v_z(x,z,t)$
$\mu(P,T)$
$T(x,t)$, T_s
$P(t)$
cooling rate at T_s
processing parameters
relaxation
$D_s(t)$
$D_s(t)$
A_1
A_2
B_1
B_2
C_1
C_2
process
orientation distribution
A_3
B_3
stress distribution
C_3
density distribution
frozen-in state
impact strength rupture strength E-modulus
birefringence
shrinkage, dimensional stability
index of refraction
properties of finished part

Fig.1.2: Schematic representation of relations between process parameters and product properties. v_z, μ, P, T, T_s *and* D_s *denote the axial velocity, viscosity, pressure, temperature, solidification temperature and solidified layer respectively.*

During injection moulding, however, this shrinkage is prevented due to the melt pressure and the adhesion to the mould wall. Therefore a different kind of stress distribution develops (B_2, section 4.4), which is tensile at the surface, shows a compressive subsurface minimum and is again tensile in the interior. Such a stress distribution is determined by the pressure curve and the solidified layer growth only. It is probably the cause of much of the problems concerning product failure and stress cracking.

Density distribution

Part of the density distribution is, similar to the stress formation, determined by the pressure curve and the solidified layer growth (contribution C_1, Greener 1986). In addition to this, a fast cooling rate at the moment of solidification may decrease the frozen-in density, since then the time is too short to reach a certain (pressure dependent) equilibrium density (contribution C_2).

Only if lateral movements are prevented, an existing or imposed stress may cause an additional density change. If, for example, a polystyrene sample (E=3400 MPa) is unilateral compressed with a stress of 10 MPa, then its change in length and density are both about 0.2%.

Solidified layer thickness

The considerations above clearly show the importance of the solidified layer thickness, D_s. The calculation of this layer thickness in the different stages of the injection moulding process, will therefore be an important issue of this thesis.

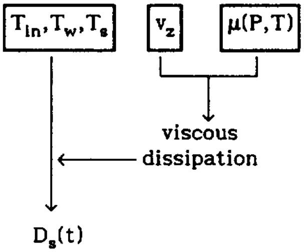

fig.1.3: Influence of process parameters on solidified layer thickness, D_s.

In fig.1.3 the parameters influencing the solidified layer thickness are depicted schematically. The most important effect is the driving force due to the temperature differences $T_{in}-T_w$ and T_s-T_w. Here T_{in}, T_w and T_s denote the initial temperature, wall temperature and solidification temperature. This will be worked out in more detail in section 2.1. Other effects such as viscous heating will delay the solid layer growth and are treated in Chapter 3.

1.3 Literature review on temperature control in injection moulding

In the past various modifications for influencing the heat transfer of the standard injection moulding process were suggested. They may be classified into three mayor categories: 1 Control of the heat transfer by means of the mould cooling fluid (Johnson 1963, Delphy 1972); 2 Use of a thin coating or a (locally) different mould material to elevate the contact temperature between melt and mould (Wübken 1974, Menges 1974, Liou 1987, Wimberger-Friedl 1990, Flaman 1990), or 3 Use of a heating element to actively regulate the cooling process (Kim et al. 1986, Liou 1987, Wadhwa et al. 1988, Flaman 1990). The first proposal was indeed seen to be capable of improving the product quality (e.g. Johnson 1963), but is rather impractical since it involves the time consuming heating and cooling of large parts of the mould system. The suggestion to use a thin coating is in fact the most elegant one, since it is most effective at the right time (during the filling stage) and at the right spot (near the mould wall, where the orientation level is highest). Several investigators indeed reported a decrease of the frozen-in orientation level when using these coatings (Wübken 1974, Liou 1987, Wimberger-Friedl 1990). The last mentioned category enables active control of the surface temperature and is therefore the most promising one.

The construction of such active heating elements and their effect on orientation and stress relaxation will be the subject of chapter 5. Here we only discuss some of the results of previously reported work. The earliest study of the injection moulding process in combination with heating elements, is probably that of Zonneveld (1969). He used thermocoax heating wires inserted into grooves, 4 mm below the mould surface. Therefore, the temperature response at this mould surface was relatively slow. The heating elements showed a marked effect on the flow length and product weight. More recently Kim and Suh (1986) constructed heating elements consisting of layers of graphite fibers in silicon rubber, zirconium oxide and teflon. These heating elements showed an initial heating rate of about 21 ^{o}C/s. They studied the effects on the flow length and the pressure drop during filling and called their process: "Low Thermal Inertia Molding" (LTIM). Wadhwa and Kim (1988) used a "Teledyne thermoelectric Device" and Kim and Roth (1988) showed that a modified version of this device is capable of operating at temperatures up to 350 ^{o}C. They reported a 16% lower critical J-integral for LTIM parts and a lower average amount of birefringence, as compared to conventional moulded parts.

Liou (1987) investigated the effect of insulation layers on the frozen-in orientation both numerically and experimentally. His study of (LTIM) heating elements on thermally induced stresses, however, is purely numerical. He predicted an optimum cooling history, resulting in relatively low residual thermal stresses. According to this author the cooling should be initially fast, followed by a short heating pulse at the end of the cooling process. It should be noted that his study concerns thermal stresses only, which is probably not representative for the injection moulding situation (see section 4.4). Flaman (1990) studied the effect of surface heaters on the orientation distribution numerically. He reported a considerable decrease of the orientation maxima near the wall.

In table 1.1 the most important characteristics of the different heating elements, used during the injection moulding process, are summarized. Instead of the initial heating rate, we prefer to use the temperature increase at the mould surface (ΔT_p) after one second. This one second is a typical time scale for the injection stage of the injection moulding process. Orientation and stress relaxation most effectively occur at temperatures well above the solidification temperature. In practical injection moulding situations this corresponds to a temperature increase of the mould wall of roughly 100 ^oC. Considering this, all previously reported heaters need relatively long heating (and cooling) times, which results in inattractively long cycle times.

year	power density P_A [W/cm^2]	ΔT_p(1 sec) [^oC]	main effects studied	source
1969	48	10	flow length	Zonneveld
1986	7.5	21	heating rate	Kim and Suh
1988	18	11	fracture energy (J_c), mean birefringence	Kim and Roth "
1988	?	10	flow length/pressure	Wadhwa and Kim
1992	25	100	heating rate, birefringence distr., stress distribution	this work " "

table 1.1: Characteristics of heaters in several earlier reported papers in comparison with this work. ΔT_p(1 sec.) *is the maximum reported temperature rise after 1 second.*

1.4 The energy equation

The description given here will be restricted to a long, thin rectangular cavity equipped with a film gate (see fig.1.4). As will be demonstrated in section 3.1, only minor changes are required to adapt the solution for a rectangular geometry to other geometries such as pipe- or diverging (disk) flow. The effect of the solidifying layer on the velocity profile will not be taken into account. Richardson (1983), however, showed that the solution of the temperature field can easily be adapted to include this effect. Furthermore, solutions for film-gated cavities can be transformed into solutions for cavities with a point gate (Ryan and Chung 1980).

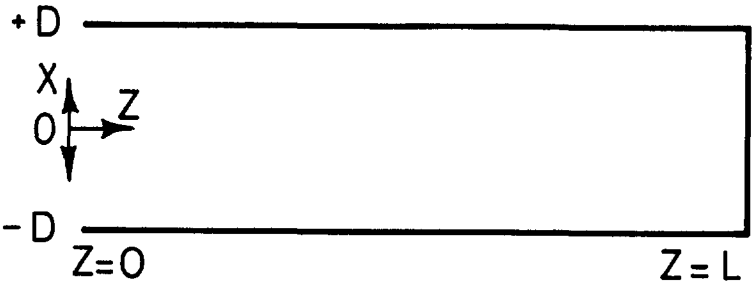

fig.1.4: Schematic representation of the mould geometry

Assumptions and equations

In polymer melt flow temperature is influenced by velocity and vice versa. This means that the momentum and energy equations are coupled and numerical techniques seem to be the only way of obtaining a complete set of solutions. However, an analytical solution which retains all the relevant aspects can be obtained by making the following approximating assumptions:

1 The flow is laminar and fully developed;

2 The height of the channel, 2D, is small with respect to its width, 2W, so that the flow in the cavity can be approximated by the flow between two flat plates;

3 Thermal properties and viscosity are temperature and pressure independent;

4 The viscosity obeys the power-law:

$$\mu = \mu_o \left(\frac{\partial v_z}{\partial x} \right)^{\nu - 1},$$

Here μ, ν, v_z and μ_o denote the viscosity, power-law index, axial velocity and consistency index respectively.

5 Heat conduction in the flow direction is neglected.

The power-law is an empirical model which works quite well in the higher shear rate regime, but overestimates the viscosity in the lower shear rate region. An estimate of the error introduced by this approximation can be obtained by comparing the results of the truncated power-law (Bird et al. 1987, p.227) with those of the power-law. The error in the velocity (and the viscous dissipation) turns out to be negligible if $\dot{\gamma}_N \mu_N / \sigma_w \ll 1$. Here $\dot{\gamma}_N$, μ_N and

σ_w denote the shear rate below which the viscosity is truncated, maximum (Newtonian) viscosity and the wall shear stress, respectively. In injection moulding problems this ratio is usually of order 10^{-2}, which justifies the use of the power-law in those cases.

With the assumptions above we obtain for the momentum and energy equations

$$\text{momentum:} -\left(\frac{\partial P}{\partial z}\right) + \frac{\partial}{\partial x}\left(\mu\frac{\partial v_z}{\partial x}\right) = 0 \tag{1.1}$$

$$\text{energy:} \quad \rho c_p\left(\frac{\partial T}{\partial t_c} + v_z(x)\frac{\partial T}{\partial z}\right) = \lambda\frac{\partial^2 T}{\partial x^2} + \mu\left(\frac{\partial v_z}{\partial x}\right)^2 + P_v(x,t_c) \tag{1.2}$$

where z denotes the axial coordinate, x the transverse coordinate, t_c the contact time, T the temperature, P the pressure, λ the thermal conductivity, ρc_p the specific heat per volume and $P_v(x,t_c)$ an internal heat generation term other than the viscous dissipation. Note that in case of constant filling velocity, the contact time is directly related to the axial position of the melt front, z_f:

$$t_c = (z_f - z)/\langle v_z \rangle = t_p - z/\langle v_z \rangle, \tag{1.3}$$

Here t_p stands for the process time, starting as the melt front passes z=0. For convenience we introduce the following dimensionless variables:

$$\tilde{T}(x,z,t) = \frac{T(x,z,t)-T_w}{T_{in}-T_w}, \quad \tilde{x} = \frac{x}{D}, \quad \tilde{z} = \frac{z}{L}, \quad \hat{z} = \frac{\tilde{z}}{Gz_m} = \frac{az}{v_m D^2}$$

$$\phi_z(x) = \frac{v_z(x)}{v_{max}}, \quad v_{max} = \frac{\alpha+1}{\alpha}\langle v_z \rangle, \quad \alpha = \frac{1}{\nu} + 1, \quad \tilde{t}_c = \frac{a t_c}{D^2}$$

$$\dot{\gamma}_w = \frac{v_{max}}{D}, \quad \hat{P} = \frac{D}{L}\cdot\frac{P}{\mu_0 \dot{\gamma}_w{}^{\nu}},$$

$$Gz_m = \frac{v_{max}D^2}{aL}, \quad Br = \frac{\mu_0 D^2}{\lambda(T_{in}-T_w)}\left[\frac{\alpha v_{max}}{D}\right]^{\nu+1}, \quad Q = \frac{P_v(x,t_c)D^2}{\lambda(T_{in}-T_w)},$$

yielding for the momentum and energy equations

$$\frac{\partial\hat{P}}{\partial\tilde{z}} + \frac{\partial}{\partial\tilde{x}}\left(\frac{\partial\phi_z}{\partial\tilde{x}}\right)^{\nu} = 0 \tag{1.4}$$

$$\underbrace{\frac{\partial\tilde{T}}{\partial\tilde{t}_c}}_{\substack{\text{instationary}\\ \text{term (1)}}} + \underbrace{\phi_z(\tilde{x})\frac{\partial\tilde{T}}{\partial\hat{z}}}_{\substack{\text{convection}\\ \text{(2)}}} = \underbrace{\frac{\partial^2\tilde{T}}{\partial\tilde{x}^2}}_{\substack{\text{conduction}\\ \text{(3)}}} + \underbrace{\mathrm{Br}|\tilde{x}|^{\alpha}}_{\substack{\text{dissipation}\\ \text{(4)}}} + \underbrace{Q(\tilde{x},\tilde{t}_c)}_{\substack{\text{generation}\\ \text{(5)}}} \tag{1.5}$$

Because the viscosity was assumed to be independent of the temperature, the velocity distribution can be calculated directly from eq.(1.4) (e.g. Bird et al. 1987, p.175):

$$\phi_z(\tilde{x}) = 1-|\tilde{x}|^{\alpha} \tag{1.6}$$

Note that the axial variable $\hat{z}$ is independent of the length of the cavity.

Initial and boundary conditions

Usually the temperature at the inlet (T_{in}) and the mould wall temperature (T_w) are assumed to be uniform and constant during the moulding process. The situation at the flow front is somewhat less clear. Directly behind this flow front, the hot core spills out towards the walls. It seems thus reasonable to assume the temperature at the flow front to be equal to T_{in}. We then obtain for the dimensionless initial and boundary conditions:

$$\begin{array}{ll} \text{initial condition:} & \tilde{T}(\hat{z}=0) = 1 \\ \text{boundary condition:} & \tilde{T}(\tilde{x}=\pm 1) = 0 \\ \text{flow front condition:} & \tilde{T}(\tilde{t}_c=0) = 1. \end{array} \tag{1.7}$$

The aim of chapter 2 and 3 of this thesis is the solution of equations (1.4) and (1.5) subject to initial and boundary conditions (1.7).

Governing terms during different injection moulding stages

Directly behind the flow front the axial velocity is about equal to the front velocity. To a first approximation, this situation can therefore be considered as that of a melt, initially at T_{in}, and moving with *uniform* velocity between two cold walls. Since the corresponding differential equation is identical with that of the cooling of a quiescent melt, this will be referred to as "the quiescent melt limit" (Chapter 2). In this limit the instationary (1) term balances the conduction term (3).

After a certain lapse of time, the instationary term vanishes and the cooling process will be completely governed by the conduction, convection and heat generation terms. This will be called the "stationary limit". It provides a useful estimate of the maximum temperature which can be expected at some distance behind the flow front and is used in section 3.2 to approximate the complete (instationary) solution of eq.(1.5) during filling.

After the cavity is completely filled, flow stops abruptly. In the next stage (the holding stage) the fluid velocity is much lower than the filling velocity. Subsequently, the convection and dissipation contributions will be small, compared with the filling stage (see table 1.2). After the gate freezes off, the terms (2) and (4) of eq.(1.5) completely vanish and the energy equation is (again) governed by the instationary and the conduction terms. In section 3.3 the temperatures during cooling are calculated, starting with the temperature at the end of the filling stage. From the expression for the moment of complete solidification, t_s, it follows that the influence of the filling stage on this t_s is small.

stage	duration [s]	instationary+convection=conduction+dissipation			
injection	$O(1)$	$O(0..1)$	$O(1..10^4)$	$O(1)$	$O(10^{-3}..10^2)$
holding	$O(10)$	$O(1)$	$O(10^{-1}..1)$	$O(1)$	$O(10^{-4}..1)$
cooling	$O(10)$	$O(1)$	-	$O(1)$	-

table 1.2: Order of magnitude of the different terms in the dimensionless energy equation (eq.1.5) during the three stages of the injection moulding process.

In chapter 5 some moulding experiments with modified heat transfer (passive insulation layers and active heating elements) are discussed. Their effect on the temperature distribution and the time for complete solidification is treated theoretically in section 2.2 and 2.3. The results of these calculations were in fact used to design the heating elements (see section 5.1).

Solidification and no-flow temperature

As was shown in section 1.2, knowledge of the solidification isotherms is crucial for understanding process-properties relationships. The exact value of the solidification temperature (here denoted as T_s), however depends on the issue studied. If one, for example, aims at the prediction of the pressure drop during filling, the solidification temperature is related to the fluid flow. A possible definition of this flow-related solidification temperature is (Janeschitz-Kriegl 1977): "The temperature below which the viscosity is a factor e(=2.718) smaller than the initial melt temperature". On the other hand, for orientation relaxation, the definition should be something like: "The orientation relaxation related T_s is the temperature below which no more orientation occurs at a time scale comparable to the processing (cycle) time". For stress relaxation a similar definition may prove useful.

In addition, there is often much discussion about the exact value of each of these solidification temperatures. For the orientation related T_s often the so-called glass transition temperature (T_g) is substituted. This is not a unique temperature, but depends for example on the cooling rate and the pressure used. Tabulated values of the T_g of polystyrene differ from 80 °C to 100 °C, while for the no-flow temperature (T_{nf}) of this material values of 130 °C or 140°C are used.

CHAPTER 2

HEAT TRANSFER IN QUIESCENT MELT LIMIT

2.1 Maximum growth of solidified layer

The energy equation under consideration in this section is one of the most simple forms which still retains some relevance with injection moulding (see also section 1.4). We assume the hot melt to move with uniform velocity v_z, i.e. as a coherent slab of material, into the cold mould. The time during which the melt is in contact with a certain distance z, downstream of the gate, is called the contact time, t_c

$$t_c = (z_f - z)/v_z \tag{2.1}$$

where z_f denotes the position of the flow front. If thermal effects due to friction with the mould wall are neglected the differential equation becomes in dimensionless form

$$\frac{\partial \tilde{T}}{\partial \tilde{t}_c} = \frac{\partial^2 \tilde{T}}{\partial \tilde{x}^2}, \qquad \tilde{T}(\tilde{x},\tilde{t}_c=0)=1 \tag{2.2}$$

This equation is solved with two different boundary conditions. In the most simple case (paragraph 2.1.1) the wall temperatures are uniform and constant in time. In paragraph 2.1.2 we account for the finite thermal diffusivity of the mould. All terms of eq.(1.2) which are neglected in eq.(2.2) tend to increase the local temperature. This even holds if the viscosity is allowed to depend on temperature and pressure and does not follow a power-law behaviour. Therefore, the solutions obtained from eq.(2.2) constitute a lower limit for the temperature profiles of the full energy equation. Subsequently, the corresponding solidified layer thickness is the fastest possible layer growth (thermal diffusion limit).

2.1.1 Fixed wall temperature

In this case we have $\tilde{T}(\tilde{x}=\pm 1,\tilde{t}_c)=0$ as a boundary condition. The solutions are found in every textbook on diffusion (e.g. Carslaw and Jaeger 1988 p.97). The result especially suited for short contact times is

$$\tilde{T}(\tilde{x},\tilde{t}_c) = 1 - \sum_{n=0}^{\infty} (-1)^n \left(\operatorname{erfc}\left[\frac{(2n+1)-\tilde{x}}{2\sqrt{\tilde{t}_c}}\right] + \operatorname{erfc}\left[\frac{(2n+1)+\tilde{x}}{2\sqrt{\tilde{t}_c}}\right] \right) \tag{2.3}$$

$$\cong \mathrm{erf}\left[\frac{\hat{x}}{2\sqrt{\tilde{t}_c}}\right], \qquad \tilde{t}_c<1, \quad \hat{x} = 1-\tilde{x} \qquad (2.3a)$$

whereas the solution especially suited for longer contact times turns out to be

$$\tilde{T}(\tilde{x},\tilde{t}_c) = \sum_{n=0}^{\infty} C_n\cos(\beta_n\tilde{x})e^{-\beta_n^2\tilde{t}_c}, \qquad \beta_n=(n+0.5)\pi, \quad C_n=\frac{2(-1)^n}{\beta_n} \qquad (2.4)$$

$$\cong \frac{4}{\pi}\cos(0.5\pi\tilde{x})e^{-(\pi^2/4)\tilde{t}_c}, \qquad \tilde{t}_c>1. \qquad (2.4a)$$

Here erf(x) denotes the error function (Abramowitz and Stegun 1972).

Let $\hat{D}_s$ be the dimensionless distance between the position of a certain specified temperature $\tilde{T}_s$ and the wall, then $\hat{D}_s$ immediately follows from the inversion of eqs.(2.3a) and (2.4a) (see e.g. Abramowitz and Stegun 1972, p.16 for the inversion of power series):

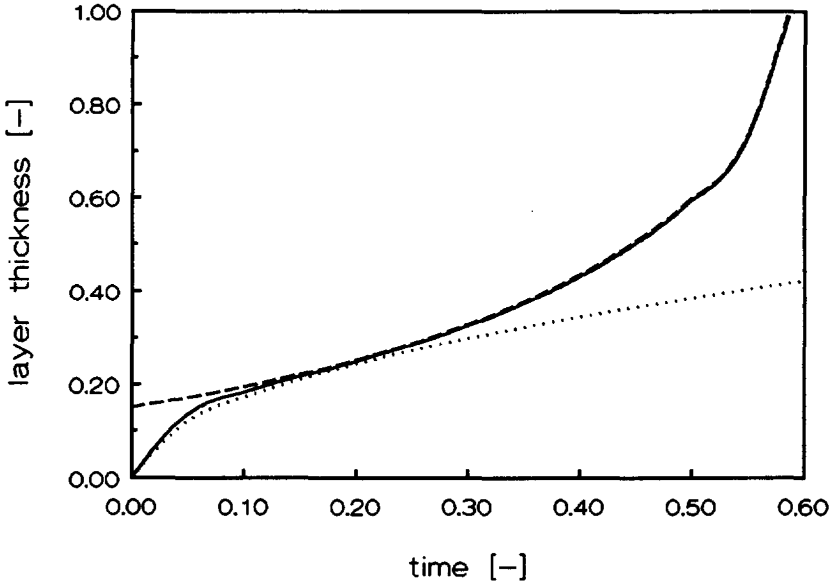

fig.2.1: Dimensionless solidified layer growth for $\tilde{T}_s=0.3$. Dotted line: eq.(2.5), dashed line: eq.(2.6) and full line eq.(2.7).

$$\hat{D}_s = \sqrt{\pi\tilde{t}_c}.\tilde{T}_s\left\{ 1 + \frac{\pi}{12}\tilde{T}_s^2 + \frac{7\pi^2}{480}\tilde{T}_s^4 + \frac{127\pi^3}{40320}\tilde{T}_s^6 + \dots \right\}, \qquad \tilde{t}_c<1 \tag{2.5}$$

and

$$\hat{D}_s = \frac{2}{\pi}\arcsin(u), \qquad \tilde{t}_c>1, \quad \text{where } u \equiv \frac{\tilde{T}_s}{C_0}e^{\beta_0^2.\tilde{t}_c} = \frac{\pi}{4}\tilde{T}_s e^{(\pi^2/4)\tilde{t}_c} \tag{2.6}$$

A better approximation of eq.(2.6) can be obtained by also taking into account the term with n=1 in eq.(2.4). Using the same iterative method as applied in appendix A, results in a correction term of $O(u.e^{-8\beta_0^2.\tilde{t}_c})$. Therefore we propose as an approximate solution which is valid for all t_c

$$\hat{D}_s = \frac{2}{\pi}\arcsin(u) + \left(\sqrt{\pi\tilde{t}_c}.\tilde{T}_s - \frac{2}{\pi}\arcsin(u)\right) e^{-c\tilde{t}_c} \tag{2.7}$$

As may be verified, this solution is fairly independent of the value of the constant "c". A value of c=8 seems to give the best fit and will be used for further calculations. In fig.2.1 an example of the solidified layer thickness $\hat{D}_s$ according to eqs.(2.5), (2.6) and (2.7) is given for $\tilde{T}_s$=0.3.

2.1.2 Effect of contact temperature between melt and mould

If two media with different, but uniform, initial temperatures are brought in close contact, the surface temperature "jumps"[1] to a certain value which lies between the initial temperatures. This contact temperature, $\tilde{T}_c$, is only determined by the thermal properties of the two materials and is given by

$$\tilde{T}_c = \frac{\sigma_{14}}{1+\sigma_{14}}, \quad \sigma_{14}=b_1/b_4, \quad b_i=\sqrt{\lambda_i\rho_i c_{p,i}} \tag{2.8}$$

Here subscripts 1 and 4 denote the polymer melt and the mould material respectively (for further details the reader is referred to section 2.2 and Carslaw and Jaeger p.88).

The effect of this jump in wall temperature on the solidified layer thickness is most easily found by substituting $\tilde{T}_s^\# = \tilde{T}_s-\sigma_{14}(1-\tilde{T}_s)$ for $\tilde{T}_s$ in eq.(2.5). The corresponding change in layer thickness then becomes in first approximation

---

[1] Note that this infinitely fast change in temperature (a direct result of eq.(2.2)) is physically certainly incorrect. The heat diffusion is always limited by the diffusion coefficient $a=\lambda/\rho c_p$ of the material under consideration. The reason for this apparent discrepancy is the presence of a term proportional to $\partial^2T/\partial t^2$ in the differential equation, which can no longer be neglected in the limit $t\searrow 0$.

$$\hat{D}_s^{\#}/\hat{D}_s = 1 - \sigma_{14}(\tilde{T}_s^{-1} - 1) \tag{2.9}$$

We remark that σ_{14} usually is of $O(0.1)$ and $\tilde{T}_s \approx 0.3$. Thus the effect on the initial layer growth is a reduction of about 10%.

2.2 Effect of an insulation layer on cooling[2]

In this section the effects of a coating on the heat transfer of injection moulding systems will be discussed. Explicit expressions are derived, describing the temperature distributions and the effect of the coating thickness on the cooling time. In section 5.2 heating curves, measured in the mould and directly at the heater surface, are compared with their predictions. The results derived for the coated mould wall are also applicable to the so called in-mould-coating process. In this process a thin decorative sheet is attached to the mould walls, sticks to the subsequently injected polymer and is ejected from the mould as part of the finished product.

2.2.1 Initial cooling stage

The system essentially consists of several slabs of material, i.e. a hot polymer melt, a cold mould wall and a thin coating in perfect contact with this mould. Each of these layers is labeled with a number as is shown in fig.2.2.

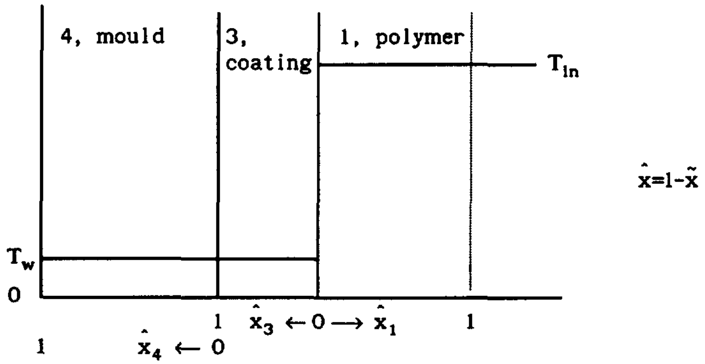

fig.2.2: System consisting of a hot melt layer (1), a coating (3) and a cold mould wall (4).

---

[2] KMB Jansen, submitted to Int J Heat Mass Transfer

This number will be used in the subscripts to distinguish between the different layers. Thus T_{in}, x_i and D_i denote the temperature, x coordinate respectively thickness of layer i. Layer 2, the "heater layer", will not be used until the next section.

For simplicity, we will only consider the quiescent melt limit (see section 1.4). The dimensionless differential equation and initial conditions for each layer i are then given by

$$K_i^2 \frac{\partial \tilde{T}_i}{\partial \tilde{t}} = \frac{\partial^2 \tilde{T}_i}{\partial \hat{x}_i^2}, \qquad \tilde{T}_i(\hat{x}_i,0) = \begin{cases} 1 \text{ if } i=1 \\ 0 \text{ if } i=2,3,4 \end{cases} \tag{2.10}$$

The coefficient K_i and the dimensionless temperature, time and thickness coordinate are defined as

$$K_i = \frac{D_i}{D_1}\sqrt{\frac{a_1}{a_i}}, \quad \tilde{T} = \frac{T-T_w}{T_{in}-T_w}, \ \tilde{t} = \frac{a_1 t}{D_1^2}, \ \hat{x}_i = 1-\frac{x_i}{D_i}$$

Here a, T_{in} and T_w denote the thermal diffusivity, initial melt- and wall temperature respectively. "a_1", a_2" etc. should not be confused with the dimensionless $a_k(\hat{z})$ used in the previous sections. Further note that D_1 is taken as the half-thickness of layer 1. During the first instants of cooling both layer 1 and 4 may be treated as semi-infinite, resulting in the boundary conditions:

$$\begin{aligned} &\tilde{T}_1(\hat{x}_1 \to\infty,\tilde{t})=1 \\ &\tilde{T}_4(\hat{x}_4 \to\infty,\tilde{t})=0 \end{aligned} \tag{2.11}$$

At the mould-coating and the coating-polymer interfaces, both temperature and heat flux are taken to be continuous. The solution of the three coupled differential equations with corresponding initial and boundary conditions is obtained by using the standard Laplace transform technique (Carslaw and Jaeger 1988, Ch 12.8). This yields

$$\tilde{T}_{1L} = 1 - \frac{1}{1+\sigma_{13}}\left\{\mathrm{erfc}(\chi_1) + (1-\varepsilon_{31})\varepsilon_{43}\sum_{n=0}^{\infty}(-\varepsilon_{431})^n \mathrm{erfc}\left[\chi_1 + \frac{(n+1)K_3}{\sqrt{\tilde{t}}}\right]\right\} \tag{2.12}$$

$$\tilde{T}_{3L} = \frac{\sigma_{13}}{1+\sigma_{13}}\left\{ \mathrm{erfc}(\chi_3) - \varepsilon_{43}\sum_{n=0}^{\infty}(-\varepsilon_{431})^n\left(\qquad \mathrm{erfc}\left[\chi_3 - \frac{(n+1)K_3}{\sqrt{\tilde{t}}}\right]\right.\right.$$

$$+ \; \varepsilon_{31}\mathrm{erfc}\left[\chi_3 + \frac{(n+1)K_3}{\sqrt{\tilde{t}}}\right] \Bigg] \Bigg\} \qquad (2.13)$$

$$\tilde{T}_{4L} = \frac{2\sigma_{14}}{(1+\sigma_{13})(1+\sigma_{34})} \sum_{n=0}^{\infty} (-\varepsilon_{431})^n \mathrm{erfc}\left[\chi_4 + \frac{(2n+1)K_3}{\sqrt{\tilde{t}}}\right] \qquad (2.14)$$

with

$$\chi_i = \frac{K_i\hat{x}_i}{2\sqrt{\tilde{t}}}, \quad b = \sqrt{\lambda\rho c_p}, \quad \sigma_{ij} = \frac{b_i}{b_j}, \quad \varepsilon_{ij} = \frac{b_i-b_j}{b_i+b_j}, \quad \varepsilon_{431} = \varepsilon_{31}\cdot\varepsilon_{43}$$

Here b and erfc(χ) again denote the so called "heat penetration coefficient" and the complementary error function. Note that the subscript "L" is added to distinguish these solutions from the solutions in the next section.

The solutions above remain valid until the heat penetrates to the center of the polymer slab or the mould wall ($\hat{x}_1$, $\hat{x}_4=1$). These situations are reached for $\tilde{t}>0.1$ and $0.1K_4^2$ respectively. For small $\hat{x}_1$, the melt temperature may be approximated by eq.(2.12) with n=0. The error then remains below 1%, provided $\hat{x}_1 \le 0.2$ and $\tilde{t} \le 0.2$.

In the case of injection moulding the equations further simplify since the mould wall (layer 4) is a much better conductor than layer 1 (polymer) and does not yet influence the heat transfer of layer 1 and 3 during the first instants of cooling. Eqs.(2.12) and (2.13) are then completely governed by their first error function terms. The contact temperature between layer 1 and 3, $\tilde{T}_{c13}$, is then constant and equal to

$$\tilde{T}_{c13} = \sigma_{13}/(1+\sigma_{13}). \qquad (2.15)$$

For $\tilde{t}>0.3K_3^2$, the heat starts to penetrate into layer 4 and $\tilde{T}_{c13}$ will decrease. Usually the initial cooling stage is very short ($\tilde{t}\sim10^{-3}$). For $\tilde{t}>K_3^2$, the transients in layer 3 vanish, resulting in a linear temperature profile, the slope and level of which still change with time. Furthermore, the contact temperature between layer 3 and 4 then becomes constant and equal to (compare with paragraph 2.1.2)

$$\tilde{T}_{c34} = \sigma_{14}/(1+\sigma_{14}) \qquad (2.16)$$

2.2.2 Further cooling and moment of solidification

As was stated before, the model above fails as soon as the assumed boundary conditions are violated. Therefore an alternative model will be developed, suited for larger time scales. Because of the symmetry, the boundary condition at the center of layer 1 (i.e. at $\hat{x}_1=1$) becomes:

$$\frac{\partial \tilde{T}_1}{\partial \tilde{x}_1} = 0 \text{ at } \tilde{x}_1=0, \qquad \text{with } \tilde{x}_1=1-\hat{x}_1$$

For convenience $\tilde{x}_1$ is used instead of $\hat{x}_1$ in the derivation below. Secondly, since the temperature in layer 3 turned out to be linear for larger times, the heat flux at the surfaces of layer 1 is proportional to the temperature difference over layer 3:

$$\frac{\partial \tilde{T}_1}{\partial \tilde{x}_1} = -\,Bi[\,\tilde{T}_1(t) - \tilde{T}_{c34}\,] \quad \text{at } \tilde{x}_1=1$$

with

$$Bi = \frac{R_2+R_3}{R_1}; \quad R_1 = \frac{\lambda_1}{D_1} \quad (\text{here } R_2=0) \tag{2.17}$$

Note that the Biot number, Bi, is defined as the ratio between the thermal resistance, R, outside and inside the polymer melt layer, which is analogous to the classical definition. For $\tilde{T}_{c34}$ we may use the value obtained from eq.(2.16). Admittedly, this temperature should decrease with time due to the finiteness of layer 1 and 4. However since σ_{14} is small, $\tilde{T}_{c34}$ tends towards zero and its effect on the temperature distribution in layer 1 may safely be neglected.

The set of equations and boundary conditions thus reduces to a standard problem with the following solution (Carslaw and Jaeger 1988, pp.121):

$$\tilde{T}_{1L} = \sum_{n=0}^{\infty} C_n \cos(\beta_n \tilde{x}_1) e^{-\beta_n^2 . \tilde{t}} \tag{2.18}$$

$$\text{with } C_n = \frac{4\sin(\beta_n)}{2\beta_n+\sin(2\beta_n)}, \qquad \tilde{t} = \frac{a_1 t}{D_1^2}$$

The roots β_n follow from the boundary condition at $\tilde{x}_1=1$ (in this case this reduces to $\beta_n \tan\beta_n = Bi$). This equation can be solved easily for both small and large values of Bi (see Appendix A). Here, the coating thickness is thin compared to that of the polymer layer and, since $\lambda_3 \approx \lambda_1$, $Bi \gg 1$. From a Taylor series expansion of α_0 near $\pi/2$ then easily follows that

$$\beta_0 = \frac{\pi}{2}\,\frac{Bi}{Bi+1} + O(Bi^{-2}),$$

and

$$C_0 = \frac{4}{\pi}\left[1-\frac{\pi^2/8}{(1+Bi)^2}\right] + O(Bi^{-3}),$$

thus

$$\tilde{T}_{1L} \cong \frac{4}{\pi}\left[1-\frac{\pi^2/8}{(1+Bi)^2}\right]\cos\left[\frac{\pi}{2}\,\frac{Bi}{1+Bi}\,\tilde{x}_1\right] e^{-\frac{\pi^2}{4}\left(\frac{Bi}{1+Bi}\right)^2\tilde{t}} \tag{2.19}$$

The symbol $O()$ is used to denote the order of magnitude of the remaining terms. In fig.2.3 some temperature profiles corresponding to real injection moulding conditions, calculated with eqs. (2.12, 13 and 14) are plotted for t=0.1 and 1.0 s., whereas eq.(2.18) is used to calculate the temperature after 2.0 seconds of cooling. All relevant parameters are listed in table 2.1.

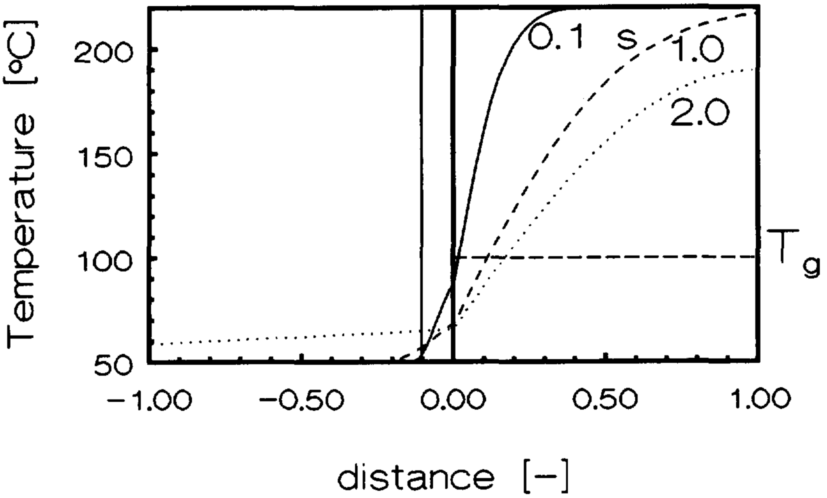

fig.2.3: Temperature distributions of a hot polystyrene sheet in contact with a cold, coated mould after 0.1, 1.0 and 2.0 seconds. The material properties are listed in table 2.1.

layer	materiaal	T(t=0) °C	λ W/mK	ρ kg/m³	c_p J/kgK	D mm	source
1	polystyrene	220	0.17	1050	1300	1.0	a)
2	carbon resin	50	1.41	1520	1510	0.025	own
3	PI (bulk)	50	0.375	1410	1340	0.087	own
4	steel	50	15.0	7900	500	36	b)

[a] D' Ans Lax (1967)

[b] Suppliers data (Steel X6CrNi 18-10)

table 2.1: Temperatures, thicknesses and thermal properties of the different heating element layers as used for the calculation of fig.2.3.

In the injection moulding process it is important to keep the cooling time as short as possible and we will therefore try to estimate the influence of the coating layer on the cooling behaviour. The cooling time is defined here as the moment at which the polymer layer is completely solidified. Since the injection temperature is usually far above the solidification temperature (T_s), this cooling time is so large that eq.(2.19) provides a fair approximation of eq.(2.18). Inverting eq.(2.19) yields for the temperature in the center ($\tilde{x}_1=0$):

$$\tilde{t}_{s,L} \cong (1+\frac{1}{Bi})^2 \frac{4}{\pi^2} \ln\left[\frac{4}{\pi} \left(1- \frac{\pi^2/8}{(1+Bi)^2}\right) / \tilde{T}_s \right] \tag{2.20}$$

where $\tilde{t}_{s,L}$ denotes the dimensionless cooling time with a coating layer present. For Bi→∞ this reduces to the well known cooling time expression in the case that no insulation layer is present. This cooling time will be referred to as $\tilde{t}_{s,0}$. Further simplification of eq.(2.20) then leads to

$$\frac{t_{s,L}}{t_{s,0}} \cong (1+\frac{1}{Bi})^2, \qquad \text{for } Bi \gg 1 \tag{2.21}$$

This expression thus gives the relative cooling time increment, which is a factor 1.2 for typical Bi-values of about 10.

2.2.3 Solidified layer thickness

The solidified layer thickness is obtained by inversion of eq.(2.12) and is given by

$$\hat{D}_{s,L} = \left([(1+\sigma_{13})\tilde{T}_s+\mathcal{E}-\sigma_{13}]\sqrt{\pi\tilde{t}_c} - 2\mathcal{E}K_3\right)/(1+\mathcal{E}), \qquad \mathcal{E}\equiv(1-\varepsilon_{31})\varepsilon_{43} \tag{2.22}$$

Note that if material 3, the insulation layer, is absent, $b_3=b_4$ or $\mathcal{E}=0$ and the results of paragraph 2.1.2 are retained. The term containing K_3 expresses the effect of the insulation layer thickness on the solidified layer growth. If $\tilde{T}_{c13}$ (as given by eq.(2.15)) is larger than $\tilde{T}_s$, clearly no layer growth occurs. The contact temperature drops below the solidification temperature as

$$t_c \geq \frac{D_3^2}{\pi a_3}\left(\frac{2\mathcal{E}}{(1+\sigma_{13})\tilde{T}_s+\mathcal{E}-\sigma_{13}}\right)^2 \tag{2.23}$$

In this dimensional expression the last term is of order unity, thus the initial layer growth delay is about $D_3^2/\pi a_3$ seconds.

2.3 Effect of an external heating source on cooling[3]

2.3.1 Heating stage

In this section the system as analyzed in the previous section will be extended with a thin heat producing layer attached to the coating (layer 3), in direct contact with the melt (layer 1). This heating layer may consist of an electrically conducting layer, uniformly heated by an electrical current. Layer 3 then serves as both an electrical and thermal insulation layer. As will be shown below, the thickness of this layer turns out to be the most important design parameter.

The problem to solve is as follows. A hot polymer melt layer, initially at T_{in} is at both sides in close contact with a heater layer (2), an insulation layer (3) and a mould wall layer (4), all initially at T_w. Then, after a certain delay time, layer 2 is heated with a uniform power density $P_A(=P_vD_2)$ during t_h seconds. Due to the linearity of the differential eqs., this problem can be split up in a cooling part and a heating part. The cooling part is in fact very similar to the one treated in the previous section and may be solved in an analogous way. However, since in practice the heater layer (2) is thin and has a high thermal conductivity with respect to layer 3 (and 1), its presence will hardly change the temperature distribution. Thus the results of section 2.2 may serve as an excellent approximation of the temperature field of the cooling part during the initial cooling period. The solutions for larger times are still given by eqs.(2.18) and (2.19), but now with $R_2 \neq 0$.

---

[3] KMB Jansen, submitted to Int J Heat Mass Transfer

In the heating problem a source term is present in layer 2. For convenience, all initial dimensionless temperatures are set to zero. What is calculated, is in fact the temperature *difference* caused by the heating layer. The total temperature field is simply obtained by adding the cooling part as given above. The differential equation and initial conditions of layer 2 now become

$$K_2^2 \cdot \frac{\partial \hat{T}_{2h}}{\partial \tilde{t}} = \frac{\partial^2 \hat{T}_{2h}}{\partial \hat{x}_2^{\,2}} + Q_h, \qquad \hat{T}_{2h}(\hat{x}_2,0)=0 \tag{2.24}$$

where Q_h denotes the dimensionless source term:

$$Q_h = \frac{P_v D_2^{\,2}}{\lambda_2 T^*}$$

In all other layers this source term is absent. The temperatures are made dimensionless using T^*, the stationary temperature difference over layers 2 and 3 due to a power density P_A: $T^*=P_A R_{23}$. The origin of the $\hat{x}_2$ coordinate is taken at the 1-2 interface.

The solution of this system of differential equations is straightforward but rather tedious. A quick calculation however, shows that a 0.1 mm thick polymer coating at 100 ^{0}C has an energy content of about 2 J/cm^2 and will delay the heating process only about 0.1 second (if heated with 20 W/cm^2). Therefore, the heat capacity of layer 2 and 3 may be neglected (see also paragraph 2.3.4). Assuming further that $T_{4h}(\hat{x}_4 \rightarrow \infty)=0$ and $T_{1h}(\hat{x}_1 \rightarrow \infty)=0$ and that the temperatures and fluxes at the interfaces are continuous, the system of equations finally yields

$$\hat{T}_{1h} = \frac{2\sigma_{14}\Omega}{(1+\sigma_{14})^2}.\mathrm{ierfc}(\chi_1) + C_1.\phi(\chi_1,\Omega) \tag{2.25}$$

$$\hat{T}_{2h} = \hat{T}_{1h}(\hat{x}_1=0,\tilde{t}) + \frac{\hat{x}_2 R_2}{R_{23}}\left\{\frac{\sigma_{14}}{1+\sigma_{14}} - \frac{\hat{x}_2}{2} + C_2\mathrm{erfc}(\Omega)e^{\Omega^2}\right\} \tag{2.26}$$

$$\hat{T}_{3h} = \hat{T}_{2h} + \hat{x}_3(\hat{T}_{4h}-\hat{T}_{2h}) \tag{2.27}$$

$$\hat{T}_{4h} = \frac{2\sigma_{14}\Omega}{(1+\sigma_{14})^2}.\mathrm{ierfc}(\chi_4) - \sigma_{14}C_1.\phi(\chi_4,\Omega) \tag{2.28}$$

with

$$\Omega = \frac{1+\sigma_{14}}{Bi}\sqrt{\tilde{t}}, \quad C_1 = \frac{1}{1+\sigma_{14}} - \frac{R_2}{2R_1}, \quad C_2 = \frac{1}{1+\sigma_{14}} - \frac{R_2}{2R_{23}}$$

and

$$\phi(\chi,\Omega) \equiv \mathrm{erfc}(\chi) - \mathrm{erfc}(\chi+\Omega).e^{2\chi\Omega+\Omega^2} \qquad (2.29)$$

Here ierfc denotes the integrated error function (Abramowitz and Stegun 1972). The function ϕ increases monotonically with time and ranges from zero to unity. Soon after the start-up, the second term of eq.(2.29) vanishes and ϕ reduces to a simple error function. The polymer surface temperature, $\hat{T}_{1h}(0,\tilde{t})$, then consists of a part which increases with the square root of time, and a part equal to C_1. This is exactly the kind of behaviour which was observed experimentally (see section 5.2). In order to better understand this kind of heating behaviour, we assume that $\sigma_{14} \ll 1$ and $R_2 < R_1$ and obtain for the (dimensional) temperatures near the surface

$$T_{1h}(x_1,t) \cong P_A\left\{\frac{2\sqrt{t}}{b_4\sqrt{\pi}} + R_{23} - \sigma_{14}\frac{x_1}{\lambda_1}\right\} \qquad \text{for } t > \frac{6D_3^2}{a_3} \qquad (2.25a)$$

$$T_{4h}(x_4,t) \cong P_A\left\{\frac{2\sqrt{t}}{b_4\sqrt{\pi}} - \frac{x_4}{\lambda_4}\right\} \qquad (2.28a)$$

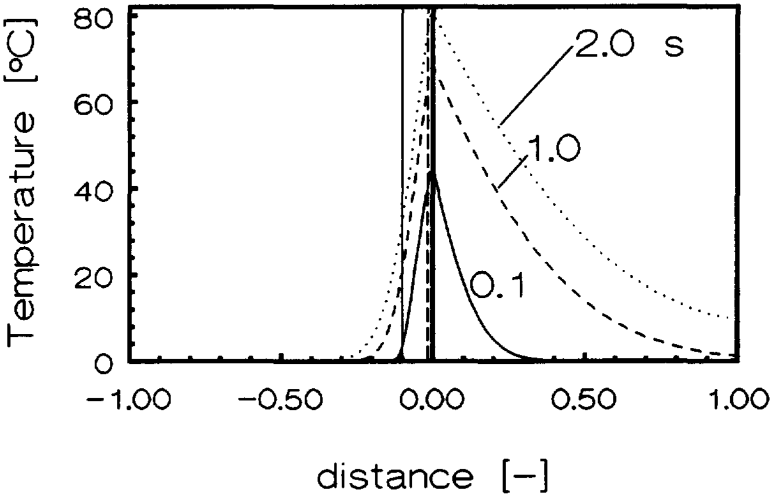

fig.2.4: Calculated temperature distributions of a cold polystyrene sheet in contact with an initially cold heating element after 0.1, 1.0 and 2.0 seconds of heating with 20 W/cm^2. Material properties and initial temperatures are listed in table 2.1.

This means that due to the thermal resistance of layer 3 (and 2), the polymer surface temperature initially "jumps" to $P_A R_{23}$ (=*O*(50 ^oC), see chapter 5) and subsequently increases with the square root of time. This second heating stage is only governed by the thermal properties of the mould material, indicating that most of the energy then flows into the mould instead of to the polymer layer (1).

An example of the temperature distributions after several periods of heating is given in fig.2.4. This clearly shows that the largest temperature rise occurs during the first half second.

2.3.2 Effect of boundary conditions

After some time one or both of the boundary conditions used in the previous derivation will be violated. Physically this corresponds to the situation that the heat front arrives at $x_1=D_1$ or at $x_4=D_4$. The subject of this paragraph is the calculation of correction terms for this effect.

Finite depth of cooling channels

If the condition $\hat{T}_{4h}=0$ is used at $\hat{x}_4=1$ then the correction terms for the polymer melt layer and the mould layer become, respectively

$$\hat{T}^{cc}_{1h}(\hat{x}_1,\tilde{t}) = -\frac{2\sigma_{14}}{(1+\sigma_{14})^2}\left(2\Omega\,\mathrm{ierfc}[\chi_1+K_{14}/\sqrt{\tilde{t}}] - \phi(\chi_1+K_{14}/\sqrt{\tilde{t}},\Omega)\right), \qquad \sigma_{14}\ll 1 \qquad (2.30)$$

$$\hat{T}^{cc}_{4h}(\hat{x}_4,\tilde{t}) = -\hat{T}_{4h}(2-\hat{x}_4,\tilde{t}) - \hat{T}_{4h}(2+\hat{x}_4,\tilde{t}) + \ldots , \qquad \sigma_{14}\ll 1 \qquad (2.31)$$

Here the superscript "cc" (cooling channel) is added to distinguish these solutions from the ones obtained previously. In case of a situation corresponding to the one in fig.2.4, the contribution of the cooling channels to the contact temperatures between layers 1-2 and 3-4 is less than -0.1 ^oC after 5 seconds and can thus safely be neglected.

Finite thickness of layer 1

If the symmetry condition (derivative equals zero) is applied at $\hat{x}_1=1$ then the solution yields the terms calculated in paragraph 2.3.1 plus some correction terms. Instead of solving the complete system of differential equations with these new boundary condition, the correction terms are more easily obtained with the method of images (Carslaw and Jaeger 1988, p.273), which yields

$$\hat{T}^{sym}_{1h} = \hat{T}_{1h}(2-\hat{x}_1,\tilde{t}) \qquad (2.32)$$

$$\hat{T}^{sym}_{4h} = \hat{T}_{4h}(2K_{14}+\hat{x}_4,\tilde{t}) \qquad (2.33)$$

2.3.3 Cooling after heating

A first estimate of the cooling of a system after a heating period of t_h seconds may be obtained by linearizing the temperature distribution at the end of the heating period and using this as a starting condition for the cooling stage. After solving the system of differential equations it turns out that the solutions can be written as the new starting temperature plus a term which reflects the (negative) heating from t_h onwards, plus a correction term:

$$\hat{T}^{cool}_{1h}(\hat{x}_1,\tilde{t}) \approx \hat{T}_{1h}(\hat{x}_1,\tilde{t}_h) \quad - \hat{T}_{1h}(\hat{x}_1,\tilde{t}-\tilde{t}_h) \quad + \text{rest} \ , \qquad \tilde{t}-\tilde{t}_h \ll 1 \qquad (2.34)$$

$$\hat{T}^{cool}_{4h}(\hat{x}_4,\tilde{t}) \approx \hat{T}_{4h}(\hat{x}_4,\tilde{t}_h) \quad - \hat{T}_{4h}(\hat{x}_4,\tilde{t}-\tilde{t}_h) \quad + \text{rest} \ , \qquad \tilde{t}-\tilde{t}_h \ll 1 \qquad (2.35)$$

This is in fact an interesting result since it means that the cooling after heating proceeds with roughly the same speed as the start-up of the heating period.

2.3.4 Comparison with numerical calculations

In this paragraph the analytical model developed so far will be compared with a numerical model (developed by A.A.M. Flaman) using a fully implicit central difference scheme. This model, essentially, solves the same set of differential equations (2.10) as the analytical model does.

Check of numerical model

Before using this numerical model a check on its internal consistency is made by verifying the relationship

$$T(\Delta T_{in},Q_h) - T(\Delta T_{in},0) - T(0,Q_h) = 0 \qquad (2.36)$$

where ΔT_{in} denotes the initial temperature difference ($T_{in}-T_w$). Eq.2.36 can be proved from the sets of differential equations with initial and boundary conditions eqs.(2.10) and (2.24). I says that the temperature field due to an initial temperature difference in combination with a heat source is equal to the temperature field caused by the temperature difference plus the temperature field caused by the heat source (see also §2.3.1). The material parameters and heating conditions used, are listed in table 2.2.

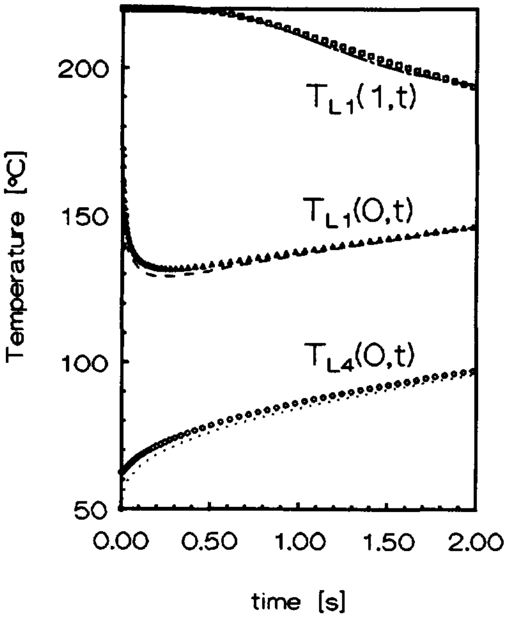

fig.2.5: *Check of numerical model after 1 second heating. Conditions as in table 2.2*

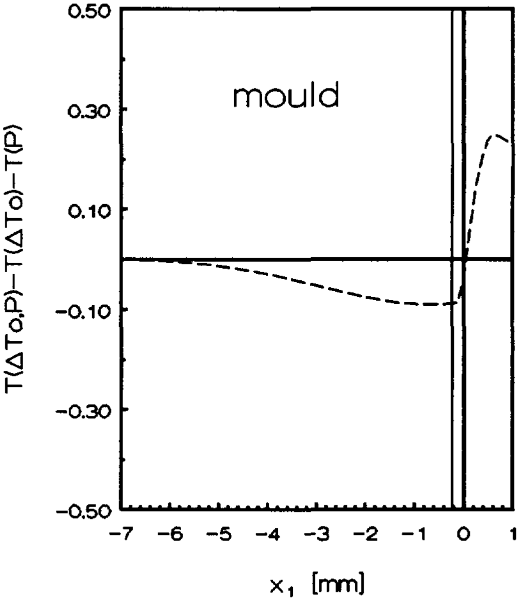

fig.2.6: *Comparison between analytical (lines) and numerical (symbols) solution. Data as in table 2.2.*

material	initial temperature [°C]	λ [W/mK]	ρ [kg/m^3]	c_p [J/kgK]	D [mm]	number of elements	P_A [W/cm^2]
Polystyrene	220	0.17	1050	1300	1.0	50	-
carbon resin	50	1.41	-	-	0.030	30	20
Polyimide	50	0.375	-	-	0.086	43	-
steel	50	15.0	7900	500	40	140	-

table 2.2: parameters used for comparison between numerical and analytical models

It turns out that after 1 second heating the maximum deviation is about 0.3 °C (see fig.2.5), which seems reasonably accurate and occurs near the heater-polymer interface. This is probably due to the grid sizes and time steps used in the numerical model and may be a subject of further investigation.

Effect of heat capacity of layer 2 and 3

In order to enable the analytical calculation of the temperatures due to the heating-up of layer 2, the heat capacities of layer 2 and 3 were neglected. The error introduced by these assumptions is easily estimated numerically. Neglecting the heat capacities causes the temperature to be about 3 ^{o}C too high after 0.2 s. After 1 second the difference reduces to 1.7 ^{o}C. From there on a good (less than 1 ^{o}C) agreement between numerical and analytical predictions is observed.

Direct comparison between numerical and analytical calculations

In fig.2.6 the temperatures due to a combined heating (20 W/cm^2) and cooling (ΔT_{in}=170 ^{o}C) history are plotted. The lines and symbols denote the analytical and numerical approximations respectively. The numerical approximation was performed with zero heat capacity of layers 2 and 3 and should therefore coincide with the analytical prediction. For short times (t<0.05 s), however, this is clearly not the case, whereas for larger times the agreement is better. The reason for these discrepancies is not completely clear yet, although it is expected that they are partly due to numerical discretization errors.

2.3.5 Solidified layer thickness with heating

The solidified layer thickness is obtained in the usual way from eqs.(2.12) and (2.25a). The result is

$$\hat{D}_{s,h} = \frac{\hat{D}_{s,L} - N_h^{\#}\left(2\sigma_{14}\tilde{t}_c/Bi + \sqrt{\pi\tilde{t}_c}\right)}{1 - N_h^{\#}\cdot\sqrt{\pi\tilde{t}_c}/Bi}, \qquad N_h^{\#} = \frac{1+\sigma_{13}}{1+\sigma_{14}}N_h/(1+\mathcal{E}) \tag{2.37}$$

Here $\hat{D}_{s,L}$ is the result given by eq.(2.22).

Appendix A: The roots of $\beta\tan\beta$ = Bi

The roots of

$$\beta\tan\beta = \mathrm{Bi} \tag{A1}$$

and

$$\alpha\cot\alpha + \mathrm{Bi} = 0 \tag{A2}$$

occur in the solutions of problems involving the cooling of an infinitely wide slab of which the heat flux at the surfaces depends linearly on the surface temperature (Carslaw and Jaeger 1988, p.121). This boundary condition may be applied in the case of radiation into a medium with constant temperature and cooling against an infinite medium with contact resistance. If the initial temperature is an even function of position we have to determine the roots of eq.(A1), whereas an uneven starting function demands the solution of eq.(A2).

Although the solution techniques for the transcendental equations are quite standard (e.g. Olver 1974, section 1.5), a brief outline is given below. We start with eq.(A1) for small values of Bi. In this case $\tan\beta$ has to be small and thus β will be near $n\pi$, where $n=0,1,2,\ldots$ We therefore introduce $c_n \equiv n\pi$ and $\beta_n = c_n + \varepsilon$, with $|\varepsilon| \ll 1$. After substituting β_n and developing $\tan(c_n+\varepsilon)$ as a power series of ε, (A1) becomes:

$$c_n\varepsilon + \varepsilon^2 + \frac{1}{3}c_n\varepsilon^3 + \frac{1}{3}\varepsilon^4 + \frac{2}{15}c_n\varepsilon^5 + \frac{2}{15}\varepsilon^6 + \ldots = \mathrm{Bi}.$$

This expression is easily inverted (Abramowitz 1972, pp.16) to obtain ε as a function of Bi and c_n. After introducing this ε, β_n becomes

$$\beta_n = c_n\left\{1 + y - y^2 + (2 - \frac{1}{3}c_n^{\,2})y^3 - (5 - \frac{4}{3}c_n^{\,2})y^4 + (14 - 5c_n^{\,2} + \frac{1}{5}c_n^{\,4})y^5 \right.$$
$$\left. -(42 - \frac{56}{3}c_n^{\,2} + \frac{23}{15}c_n^{\,4})y^6 + \ldots \right\} \qquad \text{for } \mathrm{Bi} < n\pi \tag{A3}$$

with

$$y \equiv \frac{\mathrm{Bi}}{c_n^{\,2}} \tag{A4}$$

For large values of Bi, the root will be near $(n+0.5)\pi \equiv k_n$. A similar analysis, now with $\beta_n = k_n + \varepsilon'$, leads to

$$\beta_n = k_n\left\{1 - \frac{1}{\mathrm{Bi}+1}\left(1 - \frac{1}{3}z + \frac{1}{5}(1 - \frac{2}{3}/\mathrm{Bi})z^2 - \frac{1}{7}(1 - \frac{26}{15}/\mathrm{Bi} + \frac{17}{45}/\mathrm{Bi}^2)z^3 + \ldots\right)\right\} \tag{A5}$$

with

$$z = \frac{k_n^2 Bi}{(Bi+1)^3} \quad \text{and for } Bi>n\pi \tag{A6}$$

Note that for $Bi<0.1$ and $n=0$, β_0 may be approximated by $\sqrt{Bi}$. The first four roots of eq.(A1) for values of Bi between 0.1 and 100 are compared with tabulated solutions (Carslaw and Jaeger 1988, Abramowitz 1972), as is shown in table A1.

Bi	n=0	n=1	n=2	n=3
0.1	0[1]	0	0	0
0.5	-0.0037	0	0	0
1.0	-0.0012	0.0005	0	0
2.0	-0.0001	0.0151	-0.0001	-0.0001
5.0	0	0.0014	0.0031	-0.0030
10.0	0	0	0.0017	0.0304
15.0	0	0	0.0001	0.0016
20.0	0	0	0	0.0001
100	0	0	0	0

[1] Here "0" means smaller than $\pm 5.10^{-5}$

table A.1: Difference between approximate solution (eq.A3 or eq.A5) and exact solution (Carslaw and Jaeger 1988) of eq.(A1).

The solution of eq.(A2) proceeds in a completely analogous way and is given by eq.(A3) and eq.(A5) with c_n and k_n interchanged.

Acknowledgement

The numerical calculations in paragraph 2.3.4 were performed by A.A.M. Flaman (Philips Research Laboratories, The Netherlands).

CHAPTER 3

TEMPERATURE DURING AND AFTER FLOW

3.1 Stationary temperature during filling[1]

During the filling stage of the injection moulding process a hot melt is forced into a narrow channel, which temperature is far below the solidification temperature of the melt. Due to the relatively high viscosity of the melt, the flow is laminar and the velocity profile is fully developed. After a certain lapse of time, the temperature distribution, initially uniform, will reach its steady state value. The calculation of this stationary temperature distribution is the subject of this paragraph. The corresponding differential equation is obtained by dropping the instationary term in eq.(1.5):

$$\phi_z(\tilde{x})\frac{\partial \tilde{T}}{\partial \hat{z}} = \frac{\partial^2 \tilde{T}}{\partial \tilde{x}^2} + \mathrm{Br}|\tilde{x}|^{\alpha} + Q(\tilde{x}) \tag{3.1}$$

It is convenient to split up the solution in separate parts. The first (and most important) part, is the contribution of the convection and conduction terms (paragraph 3.1.1). The second part, the contribution due to the source terms $\mathrm{Br}|\tilde{x}|^{\alpha}$ and $Q(\tilde{x})$ (compression heating or chemical reaction), is treated in paragraph 3.1.2 and 3.1.6, respectively. The emphasis lies on the regions near the mould walls where the largest degrees of orientation are created. As the trend in industry today is to moulding with moderate to high injection speeds, only situations are considered where the ratio of heat convection to heat conduction is large ($Gz_m > 50$).

A review of the solutions of the problems concerning the cooling of a flowing viscous melt is given by Pearson (1985). Perturbation solutions without the viscous dissipation effects were first obtained by Lévêque (1928) and Newman (1969). It is clear that in the case of large flow rates heating by dissipation can no longer be disregarded. A first term approximation of the viscous heating contribution was presented by Richardson (1979, 1983).

---

[1] Reprinted from: KMB Jansen and J van Dam (1992), Rheol Acta 31:592-602

However, this solution tends to give too high an estimate of the temperatures in situations where $Gz_m=O(100)$ and the viscous dissipation is high ($Br>10$), corresponding to common injection moulding conditions. In the present work a more extended expression for the viscous dissipation part will be derived, the first term of which corresponds to Richardson's solution. The solution presented here agrees quite well with numerical solutions. It also converges to the solution valid for the region far from the wall and is thus able to describe the maximum temperature due to viscous heating.

3.1.1 Convection-conduction contribution

As was stated before, the solution of the energy equation can be split up into a part due to the convection and conduction terms, $\tilde{T}_A$, and a part containing the dissipation effect, $Br\tilde{T}_B$:

$$\tilde{T}(\hat{x},\hat{z}) = \tilde{T}_A(\hat{x},\hat{z}) + Br\tilde{T}_B(\hat{x},\hat{z}) \tag{3.2}$$

$$\begin{array}{lll} \text{initial conditions} & \tilde{T}_A(\hat{x},0)=1, & \tilde{T}_B(\hat{x},0)=0 \\ \text{boundary conditions} & \tilde{T}_A(0,\hat{z})=0, & \tilde{T}_B(0,\hat{z})=0 \end{array} \tag{3.3}$$

In the equations above $\hat{x}$ is introduced for $1-|\tilde{x}|$. After expanding the velocity distribution in terms of $\hat{x}$, the energy equation of the $\tilde{T}_A$ part becomes

$$\alpha\hat{x}\left[1 - \frac{1}{2}(\alpha-1)\hat{x} + \frac{1}{6}(\alpha-1)(\alpha-2)\hat{x}^2 - ..\right]\frac{\partial\tilde{T}_A}{\partial\hat{z}} = \frac{\partial^2\tilde{T}_A}{\partial\hat{x}^2} \tag{3.4}$$

Eq.(3.4) can be solved with the method described in appendix B. In our case the solution can be written as a function of the following similarity parameters (see also appendix B):

$$\chi \equiv \frac{\alpha\hat{x}^3}{9\hat{z}}, \quad \varepsilon \equiv \left(\frac{9\hat{z}}{\alpha}\right)^{1/3}$$

Applying the results derived in appendix B gives for $\tilde{T}_A$:

$$\tilde{T}_A = v_{A,0}(\chi) - \frac{\varepsilon(\alpha-1)}{10}v_{A,1}(\chi) - \varepsilon^2\left(K_2 v_{A,2}(\chi) + K_3\chi^2 e^{-\chi}\right) + \dots \tag{3.5}$$

The functions $v_A(\chi)$ and constants K_2, K_3 are defined as:

$$v_{A,0}(\chi) = \frac{\gamma(1/3,\chi)}{\Gamma(1/3)}$$

$$v_{A,1}(\chi) = \chi^{1/3}\left[1 - \frac{\gamma(4/3,\chi)}{\Gamma(4/3)}\right]$$

$$= v_{A,0}(\chi) - \chi^{1/3}e^{-\chi}/\Gamma(4/3)$$

$$v_{A,2}(\chi) = \frac{\Gamma(5/3)}{\Gamma(4/3)}\chi^{1/3}e^{-\chi}M\left(\frac{5}{3},\frac{4}{3},\chi\right) - \frac{\Gamma(4/3)}{\Gamma(2/3)}e^{-\chi}\left[M\left(\frac{4}{3},\frac{2}{3},\chi\right) - 2\chi - 1\right],$$

$$K_2 = \frac{\Gamma(2/3)}{\Gamma^2(4/3)}.\frac{(\alpha-1)(11-\alpha)}{840}, \quad K_3 = \frac{3(\alpha-1)^2}{200\Gamma(4/3)},$$

and $\Gamma(4/3)=0.8930$, $\Gamma(5/3)=0.9027$,

$$M(a,b,\chi) = \sum_{n=0}^{\infty}\frac{a(a+1)..(a+n-1)\chi^n}{b(b+1)..(b+n-1)n!}, \qquad \gamma(a,\chi) = \frac{1}{a}\chi^a e^{-\chi}.M(1,a+1,\chi)$$

denote two complete gamma functions, the Kummer function and the incomplete gamma function, respectively (see Abramowitz and Stegun 1972).

Evaluation of the relative importance of the different order terms of $\tilde{T}_A$ shows that, for $Gz_m = O(100)$, the contribution of the second order term to $\tilde{T}_A$ is less than 0.01. Thus for practical purposes a first order approximation is sufficiently accurate. In order to enhance calculation speed $v_{A,0}$ and $v_{A,2}$ can be fitted by the following simple expressions:

$$\tilde{v}_{A,0}(\chi) \approx 1-(1-1.18\chi^{1/3}+0.44\chi^{2/3})e^{-\chi} \qquad \text{(absolute error} \leq 0.003) \tag{3.6}$$

$$\tilde{v}_{A,2}(\chi) \approx (0.71\chi^{0.25}+1.2\chi)e^{-\chi} \qquad \text{(absolute error} < 0.01\text{)}$$

3.1.2 Viscous dissipation part

Eq.(B12) directly yields for the $\tilde{T}_B$ part:

$$\tilde{T}_B = \varepsilon^2 v_{B,00}(\chi) - \frac{\alpha}{6}\varepsilon^3 v_{B,10}(\chi) + \frac{\alpha(\alpha-1)}{24}\varepsilon^4 v_{B,20}(\chi) - \frac{(\alpha-3)_3}{5!}\varepsilon^5 v_{B,30}(\chi) + \dots \tag{3.7}$$

where

$$v_{B,00}(\chi) = \frac{\Gamma(5/3)}{\Gamma(4/3)}\chi^{1/3}e^{-\chi}M\left(\frac{5}{3},\frac{4}{3},\chi\right) - \chi^{2/3} \tag{3.7a}$$

$$v_{B,10}(\chi) = \frac{1}{\Gamma(4/3)}\chi^{1/3}e^{-\chi}M\left(2,\frac{4}{3},\chi\right) - \chi \tag{3.7b}$$

$$= (\chi+\frac{2}{3})v_{A,0} - \chi^{1/3}e^{-\chi}/\Gamma(1/3) - \chi$$

$$v_{B,20}(\chi) = \frac{4}{3}\chi^{1/3} \tag{3.7c}$$

$$v_{B,30}(\chi) = \frac{\Gamma(8/3)}{\Gamma(4/3)}\chi^{1/3}e^{-\chi}M\left(\frac{8}{3},\frac{4}{3},\chi\right) - \chi^{5/3} \tag{3.7d}$$

The first term of eq.(3.7) equals Richardson's expression (1979) for the Br-dependent part of the solution. In eq.(3.7), all $v_{B,ki}$ terms with i>0, as given in appendix A by eq.(B20), are neglected since the contribution of their sum turns out to be small. In physical terms this means that for the viscous dissipation contribution, a linear velocity distribution in the convection part of the energy equation is assumed, whereas the source term is completely evaluated.

For small values of χ the first few terms of the series development of the Kummer functions constitute an excellent approximation of the $v_{B,k0}$ terms, whereas for larger χ, approximations of the form given by eq.(3.8) can be found by fitting the asymptotic solution (eq.B14) to $\tilde{v}_{B,00}$ (eq.(3.7a))

$$\tilde{v}_{B,00}(\chi) \approx \frac{2}{9}\left(1-e^{-6.7\chi}\right)\chi^{-1/3} \qquad \text{(abs. error < 0.01 for } \chi\text{>0.15)} \tag{3.8}$$

Equation (3.7) is especially suited for small $\hat{x}$, whereas eq.(3.10) (see paragraph 3.1.3) gives the solution for large values of $\hat{x}$ ($\hat{x}$>0.2). This suggests trying a hybrid form which matches $\tilde{T}_B$ for both small and large $\hat{x}$. Therefore the trial function $(1-\exp[-c\hat{x}^a\varepsilon^b])\tilde{T}_B^{core}$ is expanded for small $\hat{x}$ and compared with eq.(3.7). It then follows that the argument of the exponential function becomes equal to $-4.5\hat{x}^2/\varepsilon^2$. However, a somewhat smaller value of c appears to result in an better estimation of $\tilde{T}_B$ over the whole $\hat{x}$-region. We therefore write:

$$\tilde{T}_B \simeq (1-\exp[-2.9\hat{x}^2/\varepsilon^2]).\tilde{T}_B^{core} \qquad \text{(absolute error<2.10}^{-4}\text{)} \tag{3.9}$$

In fig.3.1 the viscous dissipation contribution according to eq.(3.7) is given for several values of $\hat{z}$.

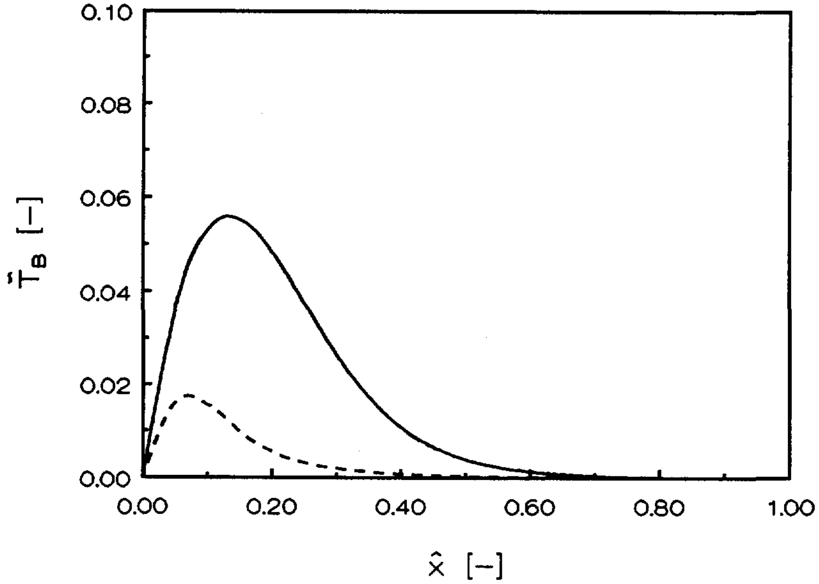

fig.3.1: Viscous dissipation contribution, $\tilde{T}_B$, according to eq.(3.7) for Br=10, α=4. Dashed curve: $\hat{z}=10^{-3}$; solid curve: $\hat{z}=10^{-2}$.

3.1.3 Comparison with core flow solution and numerical solution

Core flow solution

Near $\hat{x}=1$, χ will be large since Gz_m is large. Therefore, the temperature in the core will not differ largely from its initial value and the dependence on χ is small. If the χ dependence is omitted, the solution of the stationary energy equation reads:

$$\tilde{T}^{core}(\hat{x},\tilde{z}) = \tilde{T}^{core}_A + Br\tilde{T}^{core}_B = 1 + \frac{Br\hat{z}(1-\hat{x})^\alpha}{1-(1-\hat{x})^\alpha} \tag{3.10}$$

In the limit of $\hat{x}\rightarrow 1$ eq.(3.5)+eq.(3.7) must yield eq.(3.10). Indeed, using eq.(A14) and $\varepsilon\chi^{1/3}=\hat{x}$ we obtain:

$$\tilde{T}(\varepsilon,\chi\rightarrow 1/\varepsilon^3) = 1 - O(\varepsilon^2\chi^2 e^{-\chi}) + \frac{Br\hat{z}(1-\hat{x})^\alpha}{\alpha\hat{x}}\{1 + O(\chi^{-1})\} \tag{3.11}$$

Consequently, the Br-dependent part of eq.(3.10) is the leading term of $\hat{T}_B^{core}$.

Numerical calculations

In order to further check the validity of the analytical solution, a comparison is made with the numerical solution of eq.(3.1), which was obtained by a finite difference technique based on Saul'yevs iteration scheme (see Pearson and Richardson 1983).

As a representative injection moulding material PS DOW 678 is chosen with λ=0.13 [W/mK], a=7.10^{-8} [m^2/s], μ_0=6700 [Pa.s$^\nu$], α=3.81. In table 3.1 all relevant injection moulding conditions are summarized.

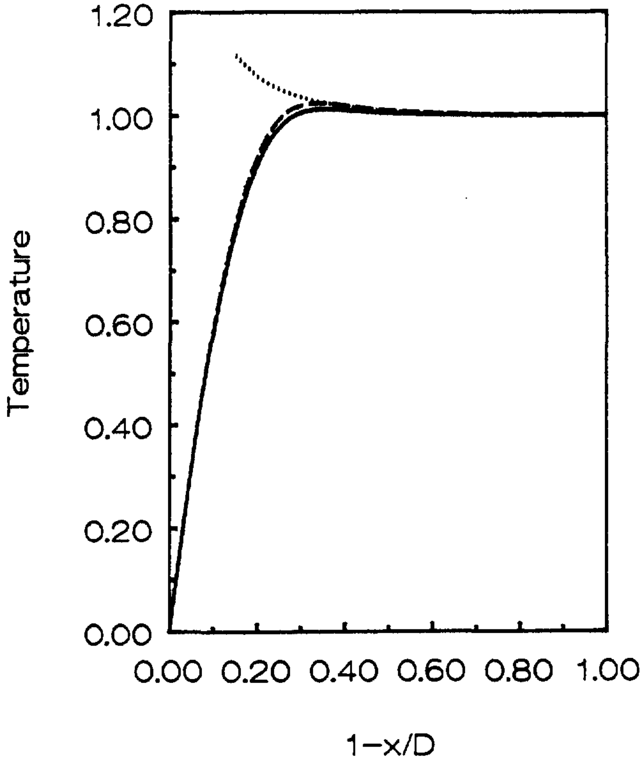

fig.3.2: Comparison of analytically predicted and numerically calculated dimensionless temperature profiles for $\hat{z}$=4.2x10^{-3}, Br=25.3 and α=3.81. The solid, dotted and dashed lines represent the analytical, core flow and the numerical solution of eq.(3.1), respectively.

figure	L [m]	2W [m]	2D [mm]	T_l [°C]	T_w [°C]	$\langle v_z \rangle$ [m/s]	Gz_m [-]	Br [-]	source
3.2	0.30	0.035	2.0	250	50	1.0	60	25.3	-
3.3	0.30	0.035	2.0	250	50	3.6	216	144	van Wijngaarden et al. 1982
3.4	0.30	0.050	2.0	256	56	1.15	104	30.8	Alles et al. 1986

***table 3.1**: Injection moulding parameters*

In figure 3.2 the solutions (3.5) and (3.7) are compared with the numerical solution of eq.(3.1) for a rather low Gz_m value of 60 and several axial positions. Near the mould wall as well as in the mid plane the numerical and analytical solutions coincide, whereas the core flow solution joins both numerical and analytical solution for $\hat{x}>0.6$. The analytical solution underestimates the maximum temperature by about 1%. Still better predictions can be obtained for larger Gz_m numbers and smaller $\tilde{z}$ and Br

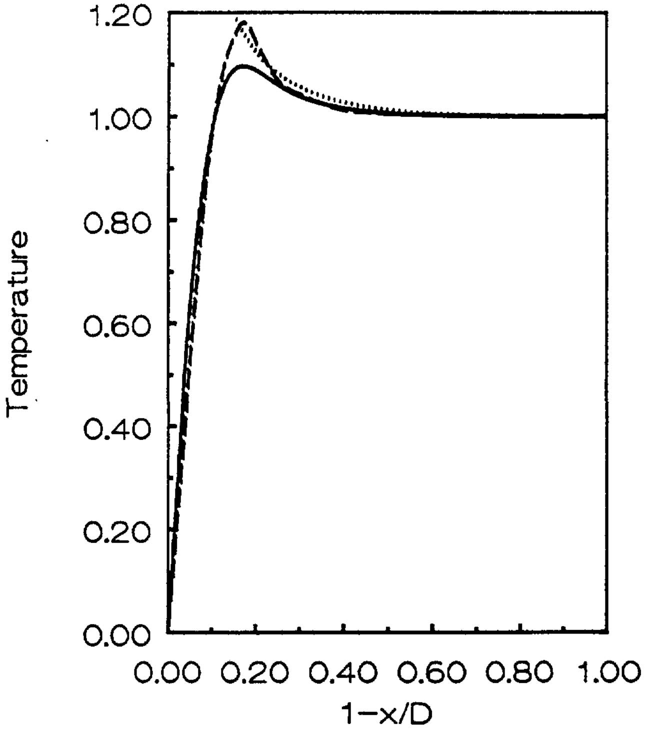

fig.3.3: Comparison of the dimensionless temperature profiles at the end of filling, predicted by the analytical approximation and the model used by Flaman (1990). The dimensionless quantities are: $\hat{z}=1.16\times10^{-3}$, Br=144 and $\alpha=3.81$. The solid, dotted and dashed lines represent the analytical, core flow and numerical predictions, respectively.

values. We thus conclude that eqs.(3.5 and (3.7)) are an accurate solution of the simplified model used.

More realistic models (van Wijngaarden et al. 1982, Flaman 1990) also include the instationary effects and use different, temperature-dependent constitutive equations. However, as will be shown below, near the duct entrance the temperatures predicted by those models agree surprisingly well with the model used in our approach.

The moulding conditions as used by Van Wijngaarden et al.(1982), only differ from the situation in fig.3.2 by a higher injection speed of 3.6 m/s. An extended version of their model was used by Flaman (1990) to calculate the temperatures as indicated by the dashed line in fig.3.3. As can be seen from this figure, he predicts an about 8% higher maximum temperature, whereas near the wall his calculated temperatures lie beneath the solution given in this

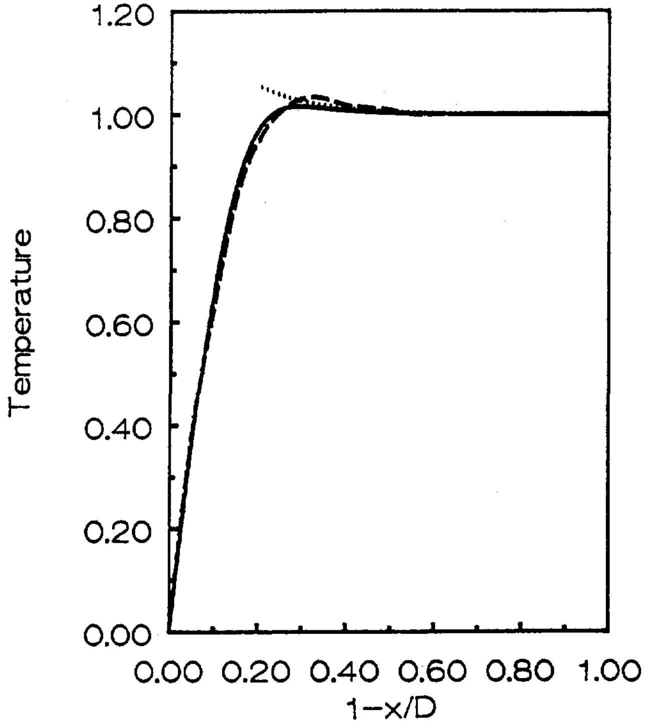

fig.3.4: Comparison of the dimensionless temperature profiles at the end of filling, predicted by the analytical approximation and the model used by Alles et a. (1986). The dimensionless quantities are: $\hat{z}$=1.93x10^{-3}, Br=30.8 and α=3.81. The solid, dotted and dashed lines represent the analytical, core flow and numerical predictions, respectively.

section. This is due to the presence of the solidified layer which shifts the area where most viscous dissipation occurs towards the core. Since the frozen-in layer also decreases the effective cross section, the velocity increases and more heat is dissipated. This will cause the viscosity to decrease, which, in its turn, decreases the dissipation. Thus the net effect will be a limited increase of the maximum temperature.

Alles et al. (1986) used experimentally determined viscosities in their numerical model to describe the filling process. In fig.3.4 we replotted the temperatures they calculated and added our predictions. Here a similar trend as in fig.3.3 is seen. However, since Br is much smaller now, less heat is generated resulting in a thicker solidified layer and a larger shift of the maximum towards the core.

3.1.4 Position of maximum temperature and solidified layer boundary

Position of the maximum temperature

An estimate of the position where the maximum temperature occurs, x_{max}, will now be made. We start with the leading term of T_A and the first three terms of T_B for large χ:

$$\tilde{T} \approx v_{A,0}(\hat{x}^3/\varepsilon^3) + \frac{\varepsilon^3 Br}{9}\left[\hat{x}^{-1} - \alpha + \frac{\alpha(\alpha-1)\hat{x}}{2}\right]$$

After differentiation with respect to $\hat{x}$ and equating the derivative to zero, we find as a first estimate of the position of the maximum:

$$\hat{x}_0 = \varepsilon.\sqrt{\ln(10/\varepsilon^4 Br)}$$

A more accurate estimate is obtained by substituting $\hat{x}_1=\hat{x}_0(1+\delta)$ and solving for δ. This results in a δ of about -0.1, while a direct comparison with numerical results leads to the same order of correction. Therefore the position where the maximum temperature occurs is given by:

$$\hat{x}_{max} \approx 0.9\varepsilon.\sqrt{\ln(10/\varepsilon^4 Br)} \tag{3.12}$$

The absolute error in eq.(3.12) is smaller than 0.01 for $\varepsilon^4 Br<0.03$.

A simple expression of $\hat{x}_{max}$ for larger values of $\hat{z}$ and Br, is not yet found.

Solidified layer thickness

For some purposes, e.g. for a determination of the position of the boundary of the solidified layer, we need an expression for the isotherms. Therefore we rewrite eq.(3.5) and (3.7) as a series of ascending powers of $\hat{x}$

with coefficients which depend on ε (or $\hat{z}$):

$$T(\hat{x},\hat{z}) = a_1(\hat{z}).\hat{x} + a_2(\hat{z}).\hat{x}^2 + a_3(\hat{z}).\hat{x}^3 + \dots \tag{3.13}$$

with

$$a_1(\hat{z}) = \frac{1}{\Gamma(4/3)\varepsilon} - \frac{\alpha-1}{10} + \frac{\mathrm{Br}\varepsilon}{2}\left[1 - \frac{\alpha\varepsilon}{3\Gamma(4/3)}\right],$$

$$a_2(\hat{z}) = \frac{\alpha-1}{10}.\frac{1}{\Gamma(4/3)\varepsilon} - \frac{\mathrm{Br}}{2},$$

$$a_3(\hat{z}) = \frac{\alpha\mathrm{Br}}{6}$$

For simplicity $\Gamma(5/3)/\Gamma(4/3)$ is taken to be unity, $k!a_k$ is the k^{th} derivative of the temperature profile at the wall.

This series is then inverted with the aid of the inversion equation listed by Abramowitz and Stegun (1972), to obtain:

$$\hat{x}(\varepsilon,\tilde{T}) = \frac{\tilde{T}}{a_1} - \frac{a_2}{a_1^3}.\tilde{T}^2 + \frac{2a_2^2 - a_1a_3}{a_1^5}.\tilde{T}^3 + O\left(\frac{\tilde{T}^4}{\varepsilon^4 a_1^5}\right) \tag{3.14}$$

The solidification isotherm determines the position of the frozen-in orientation peak (Wales 1972; Janeschitz-Kriegl 1979). Near the wall the temperature profile is almost linear and the first term of eq.(3.14) is sufficient to describe the solidified layer thickness, $\hat{D}_s$:

$$\hat{D}_s(\hat{z}) = \frac{\tilde{T}_s}{a_1} = \frac{\tilde{T}_s}{\left(\frac{1}{\Gamma(4/3)\varepsilon} - \frac{\alpha-1}{10}\right) + \frac{\mathrm{Br}\varepsilon}{2}\left(1 - \frac{\alpha\varepsilon}{3\Gamma(4/3)}\right)} \tag{3.15}$$

where $\tilde{T}_s$ denotes the dimensionless solidification temperature. Note that the denominator of eq.(3.15) consists of a separate convection-conduction term and a viscous dissipation term. If other heat generating contributions are present, they have to be added to the denominator in a similar manner. In figure 3.5 the solidified layer thickness is given for the injection moulding conditions of fig.3.3 with $\tilde{T}_s$=0.25 (solid line). The dashed line indicates the layer thickness without the dissipation contribution. It is clear that this contribution cannot be disregarded in this case. As a comparison also the predicted layer thickness of the penetration theory is shown (see Janeschitz-Kriegl 1979).

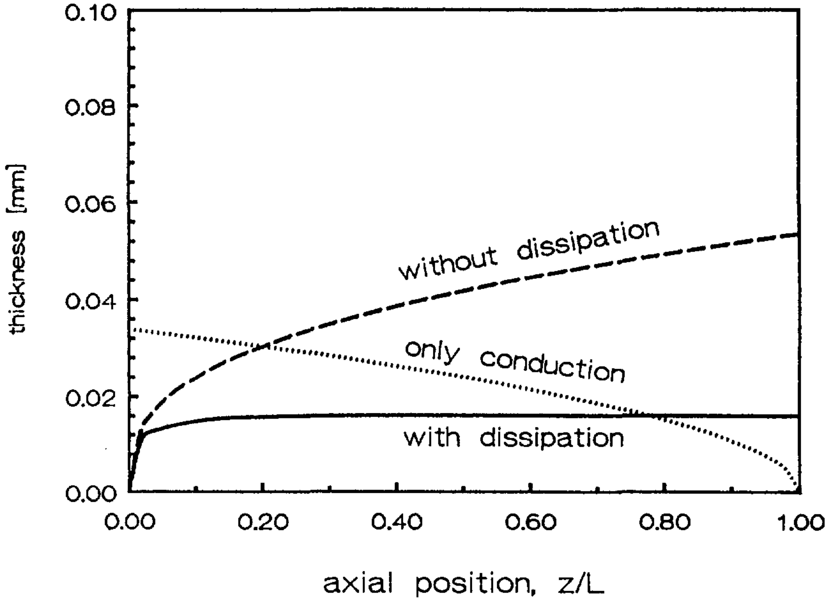

fig.3.5: Comparison of predicted solidified layer thicknesses at the end of filling. The solid and dashed lines correspond to the conditions as used in fig.3.3 with Br=144 and Br=0, respectively. The dotted line is the layer thickness as predicted by the penetration theory, i.e. with $Gz_m=0$ *and Br=0.*

3.1.5 Other heat sources (compression and chemical reaction)

In addition to viscous dissipation several other internal heat sources may affect the temperature distribution. Their contribution is easily calculated with the aid of appendix B.

Chemical reaction

In case of a zeroth order chemical reaction with heat production $P_{v,CR}$ [W/m^3], the source term becomes

$$Q_{CR} = \frac{P_{v,CR} D^2}{\lambda(T_i - T_w)}$$

and for the dimensionless temperature rise, $\tilde{T}_{CR}$, the exact solution is

$$\tilde{T}_{CR}(\hat{x},\hat{z}) = \frac{Q_{CR}}{2}\varepsilon^2 v_{B,00}(\chi) \qquad (3.16)$$

$$= 0.5Q_{CR}\left[\varepsilon\hat{x} - \hat{x}^2 + O(\hat{x}^4/\varepsilon)\right] \tag{3.16a}$$

Compression heating

In the steady state the dimensionless compression contribution is given by

$$Q_{compr}(\tilde{x}) = Q_c \cdot \phi_z(\tilde{x}), \quad Q_c = \frac{(\overline{\alpha_v T})D^2 v_{max}}{\lambda(T_l - T_w)}\left(\frac{\partial P}{\partial z}\right)$$

Here α_v denotes the volumetric thermal expansion coefficient in $[K^{-1}]$ and $(\overline{\alpha_v T})$ is assumed to be constant. $(\partial P/\partial z)$ denotes the pressure drop in the channel. Usual values of $(\overline{\alpha_v T})$ and Q_c are about 0.2 and $O(1)$ respectively.

This compression effect was treated by Laven (1985) for large values of $\hat{z}$. For small $\hat{z}$, as is common in injection moulding processing, the temperature rise due to compression is easily obtained using eq.(B12):

$$\tilde{T}_{compr}(\hat{x},\hat{z}) = 1.5\hat{z}Q_c\left[v_{B,10}(\chi) - \frac{\alpha-1}{3}\hat{x}\right] + O(Q_c\varepsilon^5) \tag{3.17}$$

$$= \frac{\alpha Q_c}{6}\left(\frac{\varepsilon^2\hat{x}}{\Gamma(4/3)} - \hat{x}^3 + O(\hat{x}^4/\varepsilon)\right) \tag{3.17a}$$

In order to calculate the effect of a zeroth order chemical reaction and compression heating on the stationary solidified layer thickness, the terms proportional to $\hat{x}$ have to be added to the denominator of eq.(3.15).

3.1.6 Other geometries (pipe flow and divergent flow)

Pipe flow solution

The method developed here for a rectangular mould can easily be extended to other geometries. As an example a solution will be given for a cylindrical pipe. Let r denote the radial coordinate and z the axial coordinate in a circular pipe of radius R and length L. In this case the dimensionless energy equation reads:

$$\left(1 - \tilde{r}^{\alpha}\right)\frac{\partial\tilde{T}}{\partial\hat{z}} = \frac{\partial^2\tilde{T}}{\partial\tilde{r}^2} + \frac{1}{\tilde{r}}\frac{\partial\tilde{T}}{\partial\tilde{r}} + Br.\tilde{r}^{\alpha} \tag{3.18}$$

Initial condition: $\tilde{T}=1$ for $\hat{z}=0$

Boundary condition $\tilde{T}=0$ at $\tilde{r}=1$

where $\tilde{r}=r/R$. The treatment is very similar to the case treated before (but now with $\tilde{r}$ instead of $\tilde{x}$). On closer inspection it turns out that the results of the channel flow solution, eqs.(3.5) and (3.7), can be used to obtain the solution for pipe flow[2]

$$\tilde{T}^{\text{pipe}} = \tilde{T}^{\text{channel}} - \frac{\hat{r}}{2}[1-v_{A,0}] - \frac{\hat{r}^2}{2}\left(\frac{\alpha-1}{10}+\frac{1}{2}\right)[1-v_{A,0}] - \varepsilon^2\frac{v_{A,2}.\Gamma(2/3)}{24\ \Gamma(4/3)} - \frac{\hat{r}^2\varepsilon e^{-\chi}}{\Gamma(4/3)}\left(\frac{\alpha-1}{5}-\frac{1}{12}\right) \tag{3.19}$$

Here $\hat{r}\equiv 1-\tilde{r}$. The effect of the geometry on the T_B part is confined to the $v_{B,ki}$ terms with $i\geq 1$, which in our approach are not taken into account. Note that the similarity variable χ in eq.(3.19) depends on $\hat{r}$ rather than on $\hat{x}$.

Diverging flow[3]

In many practical situations the width available for flow, 2W, changes along the flow direction ($W=W(r)$, see fig.3.6), while the volume flux, $\dot{V}$, remains constant. This introduces an additional position dependence of the average velocity, which shows up in the convection (and dissipation) terms in the energy equation. We will show below that, with a well suited transformation, it is still possible to solve the modified differential equation (3.1). Because of the general formulation this theory is also useful for geometries where the flow path consists of several sections with different angles of divergence. This is, of course, of practical interest since industrial products seldom consist of only one rectangular or diverging region.

We assume that the width is always much larger than the thickness ($W \gg D$). The average velocity at a certain axial position, r, then easily follows from the equation of continuity (if incompressibility is assumed):

$$\overline{v_r(r)} = \frac{\dot{V}}{4DW(r)}, \tag{3.20}$$

where the bar denotes averaging over the thickness, 2D. The essential change in the energy equation is that the convection term (first term in eq.(3.1)) now becomes dependent on the axial position. In dimensional form:

---

[2] Note that in the pipe flow solution as given by Richardson (1979) and Jansen and van Dam (1992) the homogeneous part of $v_{A,2}$ was erroneously omitted.

[3] KMB Jansen, submitted to Rheol Acta

$$\text{convection term} = v_r(x,r)\frac{\partial T}{\partial r} = \frac{\alpha+1}{\alpha}.\frac{\dot{V}}{4DW(r)}[1-|1-\hat{x}|^{\alpha}]\frac{\partial T}{\partial r}.$$

A new axial parameter, s, is now introduced such that

$$\text{convection term} = A_{\max}[1-|1-\hat{x}|^{\alpha}]\frac{\partial T}{\partial s},$$

where $A_{\max}$ is a constant. This implies that $\partial s = W(r)\partial r$ and $A_{\max}=\frac{\alpha+1}{\alpha}.\frac{\dot{V}}{4D}$. Thus, if the function W(r) is known, the convection term can be reduced to the form of eq.(3.1) by introducing

$$s(r) \equiv \int_0^r W(r)dr, \qquad A_{\max}=\frac{\alpha+1}{\alpha}.\frac{\dot{V}}{4D}, \qquad \hat{s} \equiv \frac{a.s}{A_{\max}D^2}. \tag{3.21}$$

s can be interpreted as the surface covered by the melt between the entrance and a certain axial position, r. With these substitutions, the dimensionless energy equation becomes

$$[1-|1-\hat{x}|^{\alpha}]\frac{\partial\tilde{T}}{\partial\hat{s}} = \frac{\partial^2\tilde{T}}{\partial\hat{x}^2} + \frac{Br^d|1-\hat{x}|^{\alpha}}{\tilde{W}(\hat{s})^{(1+\nu)}}, \qquad \tilde{T}(\hat{x}=0,\hat{s})=0; \quad \tilde{T}(\hat{x},\hat{s}=0)=1 \tag{3.22}$$

with

$$Br^d \equiv \frac{\mu_0 D^2}{\lambda(T_1-T_w)}\left[\frac{\alpha A_{\max}}{W_0 D}\right]^{1+\nu}, \qquad \tilde{W} \equiv \frac{W}{W_0},$$

and W_0 denotes a width which is used for scaling purposes (e.g. the width at r=0). In eq.(3.22) only the effect of the shear rate component $\partial s/\partial x$ on the viscous dissipation was taken into account. All other contributions are assumed to be negligible.

The solution of the dissipation independent part of eq.(3.22) is given by eq.(3.5) where $\hat{z}$ (as occurring in χ and ε) is exchanged by $\hat{s}$ as given in eq.(3.21). This was first recognized by Stevenson (1976) for the case of disk flow ($W(r)=\pi r$). The derivation followed here, however, is more general.

The solution of the differential equation corresponding to the viscous dissipation part, $\tilde{T}_B$, is now complicated by the presence of $\tilde{W}(\hat{s})^{1+\nu}$ in the denominator of the dissipation term (see eq.3.22).

After introducing

$$\tilde{T}_B(\hat{x},\hat{s}) = \frac{Br^d\varepsilon^2}{\tilde{W}(\hat{s})^{1+\nu}}\sum_{k=0}^{\infty}\varepsilon^k\vartheta_{B,k}(\chi) \tag{3.23}$$

we proceed analogously to paragraph 3.1.2 to obtain for each $\vartheta_{B,k}(\chi)$:

$$\chi\ddot{\vartheta}_{B,k} + \left(\frac{2}{3}+\chi\right)\dot{\vartheta}_{B,k} - \left(\frac{k+2}{3} - p\right)\vartheta_{B,k} = -\frac{(-\alpha)_k}{9k!}\chi^{\frac{k-1}{3}} + \dots \tag{3.24}$$

With as initial and boundary equations

$$\vartheta_{B,k}(0) = 0, \qquad \vartheta_{B,k}(\infty) \sim \chi^{\frac{k-1}{3}}.$$

The three dots on the right hand side stand for the contribution of previous terms ($v_{B,ki}$ with $i \geq 1$). This contribution is small and will not be considered here (see remark in paragraph 3.1.2). The only difference with the channel flow situation is the extra parameter p, which is given by

$$p \equiv (1+\nu)\frac{\partial W}{\partial s}.\frac{s}{W} \tag{3.25}$$

The solution of eq.(3.24) depends on whether p is a function of s or not. If, for example, this parameter is independent of s, eq.(3.23) becomes

$$\tilde{T}_B(\hat{x},\hat{s}) = \frac{Br^d\varepsilon^2}{\tilde{W}(\hat{s})^{1+\nu}}\sum_{k=0}^{\infty}\frac{(-\alpha)_k}{(k+2)!}\varepsilon^k v^d_{B,k}(\chi) \tag{3.26}$$

with

$$\begin{aligned} v^d_{B,k}(\chi) &= \frac{\Gamma\left(\frac{k+4}{3}\right)\Gamma\left(\frac{k+5}{3}\right)\Gamma\left(1-p\right)}{\Gamma\left(\frac{4}{3}\right)\Gamma\left(\frac{k+4}{3}-p\right)}\chi^{1/3}e^{-\chi}M\left(\frac{k+5}{3}-p,\frac{4}{3},\chi\right) - \chi^{\frac{k+2}{3}}\,{}_2F_2\left(1,p;\frac{k+4}{3},\frac{k+5}{3};-\chi\right) \\ &\sim \left(\frac{k+1}{3}\right)\left(\frac{k+2}{3}\right)\chi^{\frac{k-1}{3}}/(p-1), \qquad \text{for large } \chi; \quad p \neq 1 \end{aligned} \tag{3.27}$$

Special case: constant angle of divergence

We will now illustrate these results for two special cases in which the angle of divergence, ω, is constant. For small ω ($\omega<\pi/2$) we use the geometry as is shown in fig.3.6a because it assures that for vanishing ω the channel flow case is retained (constant width $2W_0$). Obviously this geometry is not very useful in the other limit, viz. that of $\omega \rightarrow \pi$ (disk flow). In that case, the geometry depicted in fig.3.6b is used. It is easy to show that for these cases the arc length of the width at a certain axial position is

$$W(r) = \begin{cases} W_0 + \omega r & \text{for } \omega<\pi/2 \quad \text{(near channel flow)} \\ \omega r & \text{for } \omega>\pi/2 \quad \text{(near disk flow)} \end{cases} \tag{3.28}$$

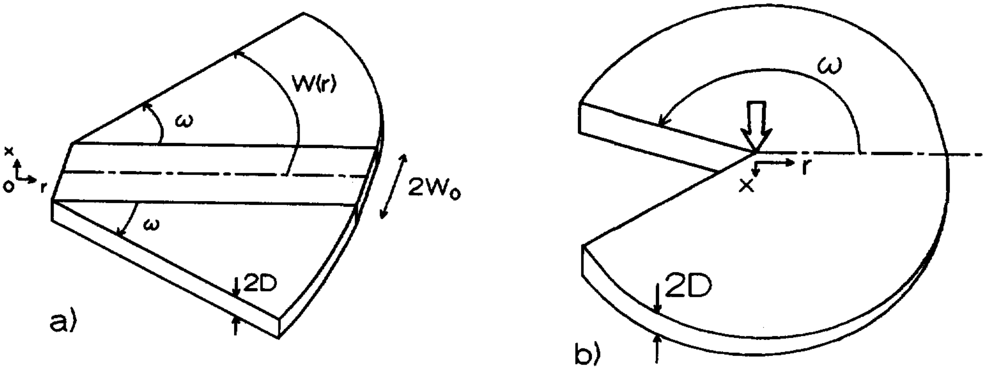

Fig.3.6: Geometry in two cases of diverging duct flow with constant angle of divergence, ω. a) small angle of divergence (near channel flow); b) nearly complete disk flow. The fat arrow indicated the fluid entrance and the dash-dotted line is the line of symmetry.

The transformation of the axial variable, eq.(3.21), then becomes

$$s(r) \equiv \int_0^r W(r)dr = \begin{cases} W_0 r + \frac{1}{2}\omega r^2 & \text{for } \omega<\pi/2 \quad \text{(near channel flow)} \\ \frac{1}{2}\omega r^2 & \text{for } \omega>\pi/2 \quad \text{(near disk flow)} \end{cases} \tag{3.29}$$

These expressions yield the dimensionless width $\tilde{W}$ as a function of $\hat{s}$:

$$\tilde{W}(\hat{s}) = \begin{cases} (1+\kappa\hat{s})^{1/2} & \text{for } \omega<\pi/2 \\ (\kappa\hat{s})^{1/2} & \text{for } \omega>\pi/2 \end{cases}, \qquad \kappa \equiv \frac{2A_m\omega D^2}{a.W_0{}^2}. \tag{3.30}$$

and thus with eq.(3.25):

$$p \begin{cases} \cong(1+\nu)\kappa\hat{s}/2 = O(\omega\varepsilon^3) & \text{for } \omega<\pi/2 \quad \text{(near channel flow)} \\ =(1+\nu)/2 & \text{for } \omega>\pi/2 \quad \text{(near disk flow)} \end{cases} \tag{3.31}$$

Eq.(3.31) shows that in the near channel flow case, p is proportional to ε^3. This means that the effect of p is delayed until the ϑ_3 term and does not contribute much to the temperature distribution. Therefore, in that case, the solution of the viscous dissipation part is given by eq.(3.26) with p=0 which is, of course, equal to eq.(3.7).

In the near disk flow case, however, p does not depend on $\hat{s}$ and ω, and varies between 1/2 (plug flow) and unity (Newtonian limit). The solution of $\tilde{T}_B$ is again given by eq.(3.26). Note that due to the asymptotic behaviour of $v^d_{B,k}(\chi)$ the Newtonian limit has to be excluded from our solution. The apparent discontinuity of p at $\omega=\pi/2$ is caused by the geometrical differences between the two cases (see fig.3.6a and fig.3.6b). It is clear that for $r \gg W_0$ the solutions of the two cases should approach each other.

To summarize: It was shown that the main effect of the geometry on the steady state heat transfer is accounted for by a simple transformation of the axial coordinate, according to eq.(3.21). This was worked out in more detail in case of constant angle of divergence. We then saw that only in the case of almost disk like flow there is an additional effect, which is confined to the dissipation dependent part of the temperature solution.

3.1.7 Conclusion

An analytical solution is presented for the calculation of the steady state temperature profiles occurring in common injection moulding circumstances. Situations with high injection speed, where the viscous heating is large, are also covered. A good agreement with the numerical solution for the region near the mould wall is found. Further, the solution is seen to converge to the asymptotic solution of the core flow.

Comparisons with some more extensive numerical models, as given in the literature (Flaman 1990; Alles et al. 1986), show differences of the relative temperatures of at most 8%. These differences are thought to be due to the assumptions which are made, such as temperature independent viscosity.

The solution can be used to calculate the position of the maximum temperature and the solidification isotherms. Also some approximate functions are derived to facilitate the calculation of the temperature field. Furthermore the effects of heating due to a chemical reaction or compression are given. Finally the solutions for the temperature profiles are generalized for the case that the width of the channel changes in the flow direction.

3.2 Instationary temperature during filling

The stationary analysis as performed in the previous section results in an accurate description of the temperature field in at least part of the product (i.e. in the entrance region) and gives useful expressions for the maximum temperatures and solidified layer thicknesses which can be expected at a certain axial position. Nevertheless, for some purposes, a complete solution of the energy equation is required. Therefore in this section an attempt is made to estimate the instationary effect in the temperature distribution during the filling stage.

The differential equation under consideration is

$$\frac{\partial \tilde{T}}{\partial \tilde{t}_c} - \frac{\partial^2 \tilde{T}}{\partial \tilde{x}^2} = -\phi_z(\tilde{x})\frac{\partial \tilde{T}}{\partial \hat{z}} + \mathrm{Br}\,|\tilde{x}|^{\alpha} \tag{3.32}$$

with

$\tilde{T}(\hat{z}=0) = 1$

$\tilde{T}(\tilde{x}=\pm 1) = 0$

$\tilde{T}(\tilde{t}_c=0) = 1.$

3.2.1 Classical instationary models

In the most simple instationary model the terms on the right hand side of eq.(3.32) equal zero. The solution is then obtained with elementary techniques, resulting in an error-function solution, which is well suited for for short cooling times, or an exponential solution for longer times (see section 2.1).

A way to include the convection term near the melt front region, was suggested by Richardson (1983). Since near the melt front the melt moves with a nearly uniform velocity, equal to the average velocity $\langle v_z \rangle$, the transformation $(z_f - z) = \langle v_z \rangle t_c$ may be used near the melt front. Here z_f denotes the axial position of the melt front. The first term of the solution is similar to the error-function solution mentioned above.

Further, an instationary model for the growth of the solidification isotherm is due to Janeschitz-Kriegl (1977,1979). His model, as will be shown in paragraph 3.2.3, may be derived from the following reasoning: 1 Assume that the convection and dissipation terms are constant in time, 2 Find an estimate (averaging by integration over the thickness) for each term in the energy balance and 3 Solve the resulting equation for the solidified layer thickness. Despite the semi-quantitative character of the model, the results are surprisingly accurate (e.g. van Wijngaarden et al. 1982).

3.2.2 Semi-instationary model

Some progress in solving the instationary energy equation can be made by realizing that the convection and dissipation contributions are almost stationary during filling (first assumption in the Janeschitz-Kriegl model). What then results is a non-homogeneous differential equation which is easily solved.

This assumption seems plausible, since during injection with constant flow rate, most of the changes in the convection and dissipation terms are caused by the effect of the channel narrowing on the local velocities. This velocity changes proportional to $1/(1-\hat{D}_s)$, where $\hat{D}_s$ is the solidified layer thickness, which increases from zero at $t_c=0$ to its stationary value, which is of $O(0.1)$[4]. Therefore only changes of about 10% in the convection contribution are to be expected during filling. Furthermore, since the flow rate remains constant, the total amount of energy convected by the fluid core does not change at all.

As for the dissipation part, two limiting cases can be distinguished. Firstly, if $\mathrm{Br} \lesssim 1$, the effect of viscous heating on the temperature profile is negligible and therefore the need of including an instationary contribution becomes irrelevant. Secondly, if $\mathrm{Br} \gg 1$, then the viscous dissipation largely suppresses the growth of the solidified layer (paragraph 2.3.3), resulting in only minor changes in the viscous dissipation term with time.

Solution for small $\tilde{t}_c$

With the convection and dissipation terms constant in time the differential equation may be written as

$$\frac{\partial \tilde{T}}{\partial \tilde{t}_c} - \frac{\partial^2 \tilde{T}}{\partial \tilde{x}^2} = -g(\tilde{x},\hat{z}). \qquad (3.32a)$$

Since the right hand side of eq.(3.32a) is independent of t_c, it follows that $g(\tilde{x},\hat{z})$ is in fact the second derivative of the stationary temperature profile, which was calculated in section 3.1. After developing $g(\tilde{x},\hat{z})$ in powers of $\hat{x}$ (use eq.3.13), the solution is obtained in the usual way (see appendix B with n=0):

---

[4] Note that in common injection moulding situations this solidified layer thickness is often much smaller than 10% (see paragraph 2.2.4).

$$\tilde{T}(\hat{x},\hat{z},\tilde{t}_c) = \mathrm{erf}(\sqrt{\chi_t}) - \sum_{k=0}^{\infty} a_{k+2}(\hat{z}).\varepsilon_t^{k+2} v_{B,k0}(\chi_t) \tag{3.33}$$

$$= \mathrm{erf}(\sqrt{\chi_t}) - a_2(\hat{z})\left[4\hat{x}\sqrt{\tilde{t}_c/\pi}.e^{-\chi_t}M(2,3/2,\chi_t) - \hat{x}^2\right] - a_3(\hat{z}).6\hat{x}\tilde{t}_c \,..$$

In this case $\chi_t \equiv \dfrac{\hat{x}^2}{4\tilde{t}_c}$ and $\varepsilon_t \equiv 2\sqrt{\tilde{t}_c}$. Note that for Br≫1, $a_2<0$, making the second term of eq.(3.33) positive.

This solution is only valid for small times. For larger t_c the method of separation of variables is more useful.

Solution for large $\tilde{t}_c$

In this case it is convenient to separate the transient contribution from the stationary solution. The equation for the transient temperature, $T^t(x,z,t)$ then becomes

$$\frac{\partial \tilde{T}^t}{\partial \tilde{t}_c} - \frac{\partial^2 \tilde{T}^t}{\partial \tilde{x}^2} = 0, \quad \tilde{T}^t(\tilde{t}_c=0)=1-\tilde{T}^{t\infty}(\tilde{x},\hat{z}), \qquad \tilde{T}^t(\tilde{x}=\pm 1)=0 \tag{3.32b}$$

If solutions of the form: $\tilde{T}^t=C_nX_n(\tilde{x})F_n(\tilde{t}_c)$ are tried, substitution readily shows that $X_n(\tilde{x})=\cos(\beta_n\tilde{x})$ and $F_n(\tilde{t}_c)=\exp(-\beta_n^2\tilde{t}_c)$. β_n is an eigenvalue which is determined by the boundary condition: $\beta_n=(n+0.5)\pi$. The normalization coefficients, C_n, follow from the initial condition. For simplicity the stationary temperature distribution, which appears in the initial condition, is approximated as unity in the core region and linearly decreasing near the mould walls:

$$\tilde{T}^{t\infty} \cong \begin{cases} 1 & \text{as } \tilde{x}\leq 1-1/a_1 \\ a_1\hat{x} & \text{as } \tilde{x}\geq 1-1/a_1 \end{cases}, \quad \text{with } a_1=a_1(\hat{z}) \text{ (see eq.3.13)} \tag{3.34}$$

With this approximation C_n becomes

$$C_n = \frac{2(-1)^n}{\beta_n}(1 - \sin\left(\frac{\beta_n}{a_1}\right)\frac{a_1}{\beta_n}) \tag{3.35}$$

$$\cong \frac{(-1)^n\beta_n}{3\alpha_1^{\,2}}\left\{1 - \frac{1}{20}(\beta_n/\alpha_1)^2 + ..\right\} \qquad (3.35a)$$

Note that in most cases $\alpha_1(\hat{z})\gtrsim 4$ and the first term in eq.(3.35a) is sufficiently accurate for n=0, 1. The instationary temperature distributions are now given by

$$\tilde{T}(\tilde{x},\hat{z},\tilde{t}_c) = \tilde{T}^{t\infty}(\tilde{x},\hat{z}) + \sum_{n=0}^{\infty} C_n\cos(\beta_n\tilde{x})e^{-\beta_n^{2}\tilde{t}_c} \qquad (3.36)$$

This expression is in fact valid for all values of t_c. Note that the procedure, followed in this paragraph, is mathematically identical with finding the solution of eq.(3.32a) with $g(x,z)=0$, $\tilde{T}(t_c=0)=1$ and $\tilde{T}(t_c\to\infty)=\tilde{T}^{t\infty}(x,z)$.

Eq.(3.36) allows us to estimate the boundary between stationary and instationary temperature distributions. If the temperature field is nearly stationary, the time dependence is almost completely confined to the term with n=0. If we demand the deviation from $\tilde{T}^{t\infty}$, to be less than 2%, the corresponding time, $\tilde{t}_{c,98}$, is given by

$$\tilde{t}_{c,98} \geq \frac{1}{\beta_0^2}.\ln[C_0/0.02] \cong 0.81.\ln[5.1/\alpha_1] \qquad (3.37)$$

Thus, if $\alpha_1=4$, the transient effects will vanish for $\tilde{t}_c\geq 0.2$.

3.2.3 Solidified layer thickness

Solution for small times

There are several ways to derive expressions for the solidification isotherms. For short times eq.(3.33) can be inverted to obtain

$$\hat{D}_s(\hat{z},\tilde{t}_c\ll 1) = \frac{\tilde{T}_s\sqrt{\pi\tilde{t}_c}}{1 - 0.4(\alpha-1)/\varepsilon\Gamma(4/3) + Br\tilde{t}_c(2-\sqrt{\pi\tilde{t}_c}} \qquad (3.38)$$

Note that this solution shows the same initial square-root-of-time behaviour as the solidified layer in case of negligible convection and dissipation.

Alternative derivation of Janeschitz-Kriegl's solution

For larger contact times eq.(3.36) can be used to derive the solidified layer thickness. However, as was pointed out above, there already exists a very useful expression which shows the right behaviour in both the small time limit and the larger time limit. We will now give an alternative derivation of this solution.

We start with substituting the approximation for the temperature profile, eq.(3.34), in eq.(3.32a). We then integrate each term over the thickness. For the instationary term this results in

$$< \frac{\partial \tilde{T}}{\partial \tilde{t}_c} > = \int_0^1 \left(\frac{\partial \tilde{T}}{\partial \tilde{t}_c}\right) d\hat{x} = \frac{\partial}{\partial \tilde{t}_c}\left(\frac{1}{2} a_1 \hat{x}^2 \Big|_0^{1/a_1} \right) = \frac{1}{2}\tilde{T}_s^{-1} . \frac{\partial \hat{D}_s}{\partial \tilde{t}_c}.$$

Repeating this for all term in eq.(3.32a) yields for the averaged energy equation

$$\frac{1}{2}\tilde{T}_s^{-1} . \frac{\partial \hat{D}_s}{\partial \tilde{t}_c} + \left(\text{<convection>} + \frac{Br}{\alpha+1} \right) = \frac{\tilde{T}_s}{\hat{D}_s} \tag{3.39}$$

Note that the front factor of the instationary term is $\frac{1}{2}\tilde{T}_s^{-1}$ instead of $\frac{1}{2}\tilde{T}_s$ (as was used by Janeschitz-Kriegl). Most probably, this is the reason of the overestimation of the layer growth in the earliest version of the Janeschitz-Kriegl model (see remark in JK 1979, p.695). As the reader may verify, eq.(3.39) shows the right behaviour in the limit of vanishing convection and dissipation contribution (yielding $\hat{D}_s = 2\tilde{T}_s\sqrt{\tilde{t}_c}$). In addition, the stationary limit (with $(\partial/\partial t_c) \gg 0$) becomes equal to $\tilde{T}_s$ divided by the average convection and dissipation terms. This stationary limit, denoted as $\hat{D}_s^{t\infty}$, can be used to scale $\hat{D}_s$ (e.g. by introducing $\psi \equiv \hat{D}_s/\hat{D}_s^{t\infty}$). The solution then becomes: $2\tilde{t}_c(\tilde{T}_s/\hat{D}_s^{t\infty})^2 = -\psi - \ln(1-\psi)$ and, using the approximate inversion as given by Janeschitz-Kriegl (1979):

$$\hat{D}_s(z,t_c) \cong \hat{D}_s^{t\infty}(z)\left(1 - \exp\left[-2a_1^{\,2} . \tilde{t}_c \right] \right)^p, \qquad p=0.417 \tag{3.40}$$

Here we used the linearity of the temperature distribution near the wall: $a_1 = \tilde{T}_s/\hat{D}_s^{t\infty}$. Note that for p=0.5 the solution eq.(3.39) yields for small contact times: $\tilde{T}_s\sqrt{(2\tilde{t}_c)}$, which is the kind of behaviour to be expected (see e.g. eq.3.38). Eq.(3.40) is supposed to become even more accurate if the stationary solution as given by eq.(3.15) is used for $\hat{D}_s^{t\infty}$.

In the derivation above, no expression for the average convection contribution was given yet. In fact, by the substitution of eq.(3.15) for $\hat{D}_s^{t\infty}$, such an expression becomes irrelevant. Janeschitz-Kriegl derived an estimation of this contribution by using a mean heat transfer coefficient, h, which is proportional to the heat flux through the solidified layer. The heat convected in the fluid core which leaks away through the solidified layer then becomes in dimensionless form:

$$\langle\text{convection}\rangle \cong \mathrm{Nu}(\ 1 - \tilde{T}_s\ ),$$

with $\mathrm{Nu}=hD/\lambda$ as the well known Nusselt number. Note that this Nusselt number is obtained by assuming that the mean convection equals the average conduction and is therefore equal to the temperature difference at the wall. Thus Nu may be expressed as $\alpha_1(z)\approx 1/\Gamma(4/3)\varepsilon$ (compare with eq.3.13). For Newtonian fluids ($\alpha=2$) this indeed corresponds to the Nusselt number used by Janeschitz-Kriegl (note the factor 2 difference in the definition of Nu).

An expression as eq.(3.40) is particularly useful since it shows us not only the behaviour at both large and small contact times, but also gives us a clear picture of how the thermal aspects (T_s, T_{in} and T_w) work out in this instationary isotherm. The argument of the exponential function is independent of any temperature, while the front factor is directly proportional to $\tilde{T}_s$. Therefore $\hat{D}_s(z,t_c)$ scales proportional to $\tilde{T}_s$. (The attentive reader could have known this from the start, since we *assumed* the temperature in the solidified layer to be linear).

3.2.4 Comparison with measurements

It is interesting to compare the predictions of the isotherms given by eq.(3.40) with measured values of the solidified layer thickness. For this purpose we will use the results of the orientation measurements (i.e. the position of the shear maximum) as discussed in chapter 5. However, eq.(3.40) cannot be used straightforward since 1) it assumes a rectangular cavity, which is not the case and 2) the exact value of the solidification temperature is not known.

Ad 1) The cavity consists of a 35 mm long entrance region with diverging flow ($\omega=20^\circ$ = 0.352 rad) and a rectangular region of 80 mm (fig.5.9). We therefore use the diverging flow theory from paragraph 3.1.6 and introduce as a new axial variable

$$\hat{s} = \begin{cases} (W_0 z+\omega z^2/2)\,.\,a/A_m D^2 & \text{for } z\le 35 \text{ mm} \\ (z-35)\,.\,a/v_m D^2 + \hat{s}_0 & \text{for } z>35 \text{ mm} \end{cases} \qquad (3.41)$$

with W_0=35 mm, D=1 mm, v_m=109 mm/s, A_m=4810 mm^2/s, a=0.124 mm^2/s and $\hat{s}_0 \equiv \hat{s}(z=35mm)=21.4x10^{-3}$. The contact time at the moment the cavity is filled completely, is now given by

$$\tilde{t}_{c,fill} = \tilde{t}_{fill} - \hat{s}. \tag{3.42}$$

Ad 2) The shear maximum at the end of the filling stage is located at the position of the no-flow isotherm (denoted as T_{nf}). Due to the relaxation process this shear maximum shifts to the mould wall until the temperature drops below the glass transition temperature (T_g). The velocity of this relaxation process is strongly dependent on the so-called relaxation time of the polymer (see section 4.2). It is rather complex to include the effect of the relaxation process in our calculations. The average solidification temperature, however, will be between T_{nf} and T_g. We will therefore make one

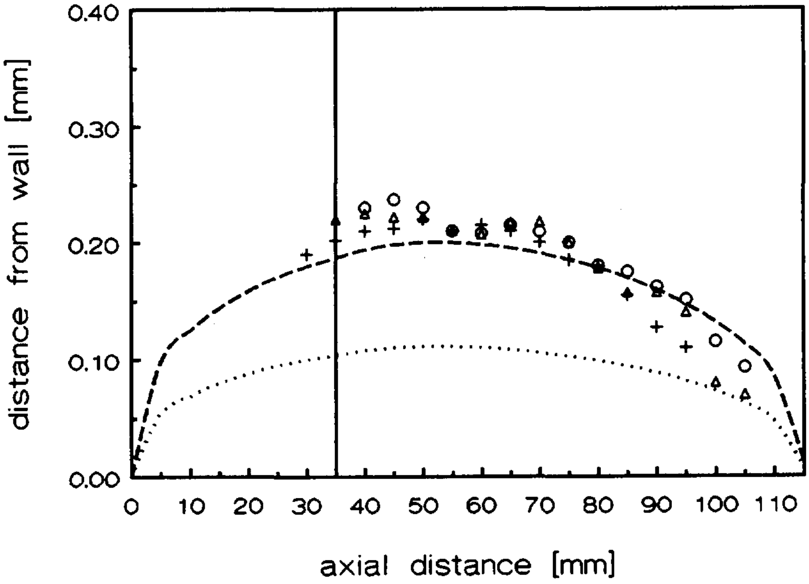

fig.3.8: Comparison of measured position of the shear maximum of the orientation distribution (symbols) and predictions of eqs.(3.39) together with (3.40) and (3.41) (lines). O: Experiment A185; Δ: A200 and +: A220 (see Chapter 5 for details). - - -: $T_s=T_{nf}=140°C$; .....: $T_s=T_g=100°C$.

prediction with T_{nf} as a solidification temperature and another with $T_s = T_g$ and compare these curves with the measured position of the shear maximum.

The results of the measurements are shown by the symbols in fig.3.8. As can be seen, there is not much difference between the experimental solidified layer thicknesses measured at different injection temperatures. We will therefore calculate the predicted curves for one T_{in} only ($T_{in} = 200^{o}C$). The lowest curve (dashed line) is the prediction for the limiting case that the relaxation is fast and T_g acts as a solidification temperature, whereas the dashed line corresponds to the opposite limit of slow relaxation. Considering the scatter of the measurements it can be concluded that eq.(3.40) predicts the *shape* of the solidification isotherm with reasonable accuracy. Moreover, since the measured values are all near the upper curve, it follows that in this case the relaxation process is slow compared to the cooling process.

3.3 Temperature after filling

3.3.1 Temperature profile and cooling time

As was stated in section 1.4, the convection contribution during the first part of the cooling stage is much smaller than in the injection stage. If this were not the case, a treatment similar to the one in the previous section would be more appropriate. However, in the following derivation the energy equation is assumed to be governed by the conduction and transient terms only.

Temperature profile

The energy equation with initial and boundary conditions become

$$\frac{\partial \tilde{T}}{\partial \tilde{t}_c} = \frac{\partial \tilde{T}}{\partial \tilde{x}^2}, \quad \tilde{T}(\tilde{t}'=0)=\tilde{T}^{tf}(\tilde{x},\hat{z},\tilde{t}_f) \quad \text{and} \quad T(\tilde{x}=\pm 1)=0 \tag{3.43}$$

Here t_f and $t' = t - t_f$ stand for the end of filling and the time starting from the moment the flow effectively stops. As a first approximation eq.(3.34) may be used as the "initial" temperature profile. Writing this in a Fourier series yields

$$\tilde{T}(\tilde{t}'=0) = \sum_{n=0}^{\infty} C_n' \cos(\beta_n \tilde{x}), \qquad \text{with } C_n' = \frac{2(-1)^n a_1}{\beta_n^{\,2}} \sin\left(\frac{\beta_n}{a_1}\right) \text{ and } \beta_n = (n+0.5)\pi \tag{3.44}$$

Following the analysis in the previous section, gives for the temperature profiles in the cooling stage

$$\tilde{T}(\tilde{x},\hat{z},\tilde{t}') = \sum_{n=0}^{\infty} C_n' \cos(\beta_n \tilde{x}) e^{-\beta_n^2 \tilde{t}'} \tag{3.45}$$

Cooling time

In this thesis we will define the cooling time as the moment the center temperature reaches T_s. Other definitions demand the *average* temperature to fall below a specified temperature. This, however, only alters the front factor of the expression for the cooling time with a factor $1/\beta_0$.

Since the desired (dimensionless) cooling time, $\tilde{t}_c$, is of $O(1)$, the first term of eq.(3.45) alone sufficiently describes the temperature profile and the expression is easily inverted to obtain

$$\tilde{t}_c' = \frac{1}{\beta_0^{\,2}}\ln(C_0'/\tilde{T}_s) \cong \frac{4}{\pi^2}\ln\left(\frac{4}{\pi}(1-\frac{\pi^2}{24a_1} + ..)/\tilde{T}_s\right) \tag{3.46}$$

In the second expression above C_0' is written as a series development in terms of β_0/a_1. Since a_1 is usually equal to, or larger than 4, the effect of the temperature after the filling stage is small ($O(0.4/a_1)$). Further note that, in order to obtain the total cooling time from the start of the injection stage, the filling time, $\tilde{t}_f$, has to be added to $\tilde{t}_c'$ as given by eq.(3.46).

3.3.2 Solidified layer thickness

In this case the first term of eq.(3.45) may still serve as a first approximation of the temperature profile to yield for the solidified layer thickness near the moment of complete solidification

$$\hat{D}_s(\tilde{t}') \cong \frac{2}{\pi}\arcsin(u), \qquad u \equiv (\tilde{T}_s/C_0')e^{\beta_0^2 \tilde{t}'} \tag{3.47}$$

For smaller times correction certainly become necessarily. Applying the same approximation as used in eq.(2.7), we obtain

$$\hat{D}_s(\tilde{t}') \cong \frac{2}{\pi}\arcsin(u) + [\hat{D}_s^{tf} - \frac{2}{\pi}\arcsin(u)]e^{-8\tilde{t}'} \tag{3.48}$$

With this equation and with the results of paragraph 3.2.3, the progression of the solidification isotherms is known during the whole moulding process. As will appear from chapter 4, these results are important for the calculation of the frozen-in stresses.

Appendix B: Perturbation solution of the diffusion equation

In this appendix a solution of the diffusion equation:

$$f(x)\frac{\partial T}{\partial z} = \frac{\partial^2 T}{\partial x^2} + g(x) \qquad \text{(B1)}$$

$$\text{Initial condition:} \qquad T=h(x) \text{ for } z=0 \qquad \text{(B2)}$$

$$\text{Boundary conditions:} \qquad T=0 \quad \text{at} \quad x=0$$

and

$$f(x)=f_0 x^n\left(1 + f_1 x + f_2 x^2 + \dots\right)$$

$$g(x)= g_0 + g_1 x + g_2 x^2 + \dots$$

$$h(x)= h_0 + h_1 x + h_2 x^2 + \dots$$

is sought for small x. For convenience, the g(x) part will be separated from the partial differential equation by introducing $T=T_A+T_B$, where T_A is the solution of the homogeneous equation. T_A satisfies the boundary and initial conditions (B2). T_B is the solution of (B1) with $T_B(x=0)=0$ and $T_B(z=0)=0$ as boundary and initial conditions respectively.

A similarity solution is tried by introducing the parameters ε and χ, so that T_A can be expanded in a series of powers of the small parameter ε:

$$\varepsilon \equiv \left(\frac{(n+2)^2 z}{f_0}\right)^{\frac{1}{n+2}}, \quad \chi \equiv \left(\frac{x}{\varepsilon}\right)^{n+2} = \frac{f_0 x^{n+2}}{(n+2)^2 z},$$

$$T_A = \sum_{k=0}^{\infty} \varepsilon^k . \vartheta_{A,k}(\chi) \qquad \text{(B3)}$$

After performing all substitutions and equating equal powers of ε, an inhomogeneous Kummer differential equation (Abramowitz and Stegun 1972) results for each $\vartheta_{A,k}$:

$$\chi\ddot{\vartheta}_{A,k} + \left(\frac{n+1}{n+2} + \chi\right)\dot{\vartheta}_{A,k} - \frac{k}{n+2}\vartheta_{A,k} = -\sum_{l=1}^{k} f_l \chi^{\frac{l}{n+2}}\left(\chi\dot{\vartheta}_{A,k-l} - \frac{k-l}{n+2}\vartheta_{A,k-l}\right) \qquad \text{(B4)}$$

with $\quad \vartheta_{A,k}(0)=0, \quad \vartheta_{A,k}(\chi\rightarrow\infty)=h_k\chi^{\frac{k}{n+2}}$

where $\dot{}$ stands for differentiation with respect to χ.

Note that the introduction of χ implies that the initial situation is not only reached for small values of z, but also for large x.

For k=0 the inhomogeneous part of eq.(B4) equals zero and the solution of $\vartheta_{A,0}(\chi)$ is easily obtained:

$$\vartheta_{A,0}(\chi) = h_0 \frac{\gamma(1/(n+2),\chi)}{\Gamma(1/(n+2))} \tag{B5}$$

where $\gamma(a,\chi)$ denotes the incomplete gamma function defined as

$$\gamma(a,\chi) = \int_0^{\chi} t^{a-1} e^{-t} dt$$

For k>0, the inhomogeneous part of eq.(B4) turns out to be of the form $K\chi^q e^{-\chi}$. Buchholz (1953) proves that the differential equation

$$\chi\ddot{\vartheta} + (b+\chi)\dot{\vartheta} - a\vartheta = K\chi^q\, e^{-\chi}$$

has a particular solution:

$$\begin{aligned}\vartheta_{\text{part}} &= \frac{K\,\chi^{q+1} e^{-\chi}}{(q+b)(q+1)} \cdot {}_2F_2\left(1, q+a+b+1; q+b+1, q+2; \chi\right) \\ &\sim K \frac{\Gamma(q+b)\Gamma(q+1)}{\Gamma(q+a+b+1)} \chi^{-a}\end{aligned} \tag{B6a}$$

where ${}_2F_2(1,a,;b,c;\chi)$ is a generalized hypergeometric function defined as

$${}_2F_2(1,a;b,c;\chi) = \sum_{k=0}^{\infty} \frac{(a)_k \chi^k}{(b)_k (c)_k},$$

and $(a)_k$ denotes Pochammer's symbol:

$$(a)_k = a(a+1)..(a+k-1).$$

For future use we remark that if the inhomogeneous part of the differential equation above equals $K\chi^q$, the particular solution becomes

$$\begin{aligned}\vartheta_{\text{part}} &= \frac{K\,\chi^{q+1}}{(q+b)(q+1)} \cdot {}_2F_2\left(1, q+1-a; q+b+1, q+2; -\chi\right) \\ &\sim K\left(\frac{\Gamma(q+b+1)\Gamma(q+2)\Gamma(a-q)}{\Gamma(b+a)\Gamma(1+a)} \chi^{-(q+1-a)} + \frac{(q+b)(q+1)}{(q-a)} \chi^{-1}\right)\end{aligned} \tag{B6b}$$

Using solution (B6a) together with the homogeneous solutions, we can calculate the next two terms of T_A:

$$\vartheta_{A,1}(\chi) = \frac{f_1 h_0}{n+4} v_{A,1}(\chi) + h_1 \chi^{\frac{1}{n+2}} \tag{B7}$$

$$\vartheta_{A,2}(\chi) = (h_2 - K_2) v_{A,21}(\chi) + K_2 v_{A,22}(\chi) - K_3 \chi^{\frac{n+5}{n+2}} e^{-\chi} \tag{B8}$$

where $$K_2 = \frac{3\Gamma\left(\frac{2}{n+2}\right)\Gamma\left(\frac{3}{n+2}\right)}{2(n+6)\Gamma\left(\frac{1}{n+2}\right)\Gamma\left(\frac{4}{n+2}\right)} h_o\left[\frac{(n+5)f_1^2}{2(n+4)} - f_2\right], \quad K_3 = \frac{h_o f_1^2}{2\left(\frac{n+4}{n+2}\right)^2\Gamma\left(\frac{1}{n+2}\right)},$$

$$v_{A,1}(\chi) = \chi^{\frac{1}{n+2}}\left[1 - \gamma\left(\frac{n+3}{n+2},\chi\right)/\left(\frac{n+3}{n+2}\right)\right]$$

$$v_{A,21}(\chi) = 2\frac{\Gamma(2/(n+2))}{\Gamma(1/(n+2))}\chi^{\frac{1}{n+2}}e^{-\chi}.M\left(\frac{n+4}{n+2},\frac{n+3}{n+2},\chi\right)$$

$$v_{A,22}(\chi) = \frac{\Gamma(4/(n+2)+2)}{\Gamma(3/(n+2)+2)\Gamma(2/(n+2)+2)}\chi_2F_2\left(1,\frac{4}{n+2}+2;\frac{3}{n+2}+2,\frac{2}{n+2}+2;\chi\right)$$

The contribution of T_B can be found in a manner similar to the calculation of T_A. The asymptotic solution for large values of x, $T_B^{x\infty}$ can be obtained by letting $\partial T_B/\partial x$ in eq.(B1) vanish:

$$T_B^{x\infty}(x \to \infty, z) = \frac{g(x).z}{f(x)} \tag{B9}$$

The introduction of χ according to eq.(B3) implies that this solution has also to apply for small values of z. In this case the right hand side of eq.(B9) vanishes which is consistent with the initial condition. Further a slightly different perturbation series is introduced:

$$T_B = \varepsilon^2\sum_{k=0}^{\infty}\varepsilon^k\vartheta_{B,k}(\chi).$$

This results in the following set of differential equations:

$$\chi\ddot{\vartheta}_{B,k} + \left(\frac{n+1}{n+2} + \chi\right)\dot{\vartheta}_{B,k} - \frac{k+2}{n+2}\vartheta_{B,k} = -\frac{g_k}{(n+2)^2}\chi^{\frac{k-n}{n+2}} - \sum_{i=1}^{k} f_i\chi^{\frac{i}{n+2}}\left(\chi\dot{\vartheta}_{B,k-i} - \frac{k-i+2}{n+2}\vartheta_{B,k-i}\right) \tag{B10}$$

with

$$\vartheta_{B,k}(\chi=0)=0, \quad \varepsilon^2\sum_{k=0}^{\infty}\varepsilon^k\vartheta_{B,k}(\chi \to \infty, \varepsilon=0) = T_B^{x\infty}(x,0)=0 \tag{B11}$$

In fact the initial condition turns out to be such that each $\vartheta_{A,k}$ vanishes for large χ. The homogeneous solutions are similar to those of $\vartheta_{A,k}$, whereas the particular solution can be considered to consist of two parts, one resulting from the first and the other from the last term on the right hand side of (B10). The first part can easily be found. As can be verified by substitution this reads:

$$\vartheta_{B,\mathrm{part1}}(\chi) = -\frac{g_k}{(k+1)(k+2)}\,\chi^{\frac{k+2}{n+2}}$$

Applying the initial and boundary condition now yields:

$$\vartheta_{B,k0}(\chi) = \frac{g_k}{(k+1)(k+2)}.v_{B,k0}(\chi) \qquad \text{(B12)}$$

where

$$v_{B,k0}(\chi) = \frac{(k+2)\Gamma\left(\frac{k+2}{n+2}\right)}{\Gamma(1/(n+2))}\,\chi^{\frac{1}{n+2}}e^{-\chi}.M\left(\frac{k+2}{n+2}+1,\frac{n+3}{n+2},\chi\right) - \chi^{\frac{k+2}{n+2}} \qquad \text{(B13)}$$

further

$$v_{B,k0}(\chi\to\infty) = \left(\frac{k+1}{n+2}\right)\left(\frac{k+2}{n+2}\right).\chi^{\frac{k-n}{n+2}} \qquad \text{(B14)}$$

The particular solution due to the last term of (B9) can be found by expanding the $\vartheta_{B,k-l}$ solutions in powers of χ, multiplied by $\exp(-\chi)$. Using (B6), this results in a particular solution consisting of a series of ${}_2F_2(1,a;b,c;\chi)$ functions, which will be denoted as $G_{kl}(\chi)$:

$$G_{kl}(\chi) \equiv \chi^{\frac{l+n+3}{n+2}}e^{-\chi}\sum_{r=0}^{\infty}\frac{\left(\frac{k-i+2}{n+2}\right)_r\chi^r\,{}_2F_2\left(1,\frac{k+l+2}{n+2}+r+2;\frac{1}{n+2}+r+2,\frac{l+1}{n+2}+r+2;\chi\right)}{r!\,\left(\frac{n+3}{n+2}\right)_r\left(\frac{i+n+2}{n+2}+r\right)\left(\frac{i+n+3}{n+2}+r\right)} \qquad \text{(B15)}$$

In order to apply the initial conditions we must know the asymptotic behaviour of G_{kl}. This turns out to be (e.g. Luke (1969)):

$$G_{kl}(\chi\to\infty) = S_{kl}.\chi^{\frac{k+2}{n+2}} \qquad \text{(B16)}$$

with

$$S_{ki}=\frac{\Gamma\left(\frac{i+n+2}{n+2}\right)\Gamma\left(\frac{i+n+3}{n+2}\right)}{\Gamma\left(\frac{k+i+2}{n+2}+2\right)}{}_3F_2\left(\frac{k-i+2}{n+2},\frac{i+n+2}{n+2},\frac{i+n+3}{n+2};\frac{n+3}{n+2},\frac{k+i+2}{n+2}+2;1\right) \tag{B17}$$

Thus the final expression for T_B becomes:

$$T_B = \sum_{k=0}^{\infty}\varepsilon^{k+2}\left\{\frac{g_k}{(k+1)(k+2)}v_{B,k0}(\chi)+\sum_{i=1}^{k}\vartheta_{B,ki}(\chi)\right\} \tag{B18}$$

where

$$\vartheta_{B,ki}(\chi) = C_{ki}S_{ki}v_{B,ki}(\chi), \qquad \text{for } i>0 \tag{B19}$$

$$v_{B,ki}(\chi)=-\left[\frac{\Gamma\left(\frac{n+3}{n+2}+2\right)}{\Gamma\left(\frac{n+3}{n+2}\right)}\chi^{\frac{1}{n+2}}e^{-\chi}.M\left(\frac{k+2}{n+2}+1,\frac{n+3}{n+2},\chi\right) - \frac{G_{ki}(\chi)}{S_{ki}}\right], \qquad i>0 \tag{B20}$$

and

$$C_{ki} = \frac{f_i g_{k-i}}{(n+2)^2}.\frac{\Gamma\left(\frac{k-i+2}{n+2}\right)}{\Gamma\left(\frac{n+3}{n+2}\right)}$$

Acknowledgement

The numerical calculations leading to fig.3.3 were performed by A.A.M. Flaman (Philips Research Laboratories, The Netherlands).

CHAPTER 4

EFFECT OF TEMPERATURE ON ORIENTATION AND FROZEN-IN STRESSES

4.1 Introduction

As was already mentioned in chapter 1, knowledge of the heat transfer is of prime importance for understanding even the simplest process-properties relationships in injection moulding. This was the motivation for the -rather extensive- calculations of the two previous chapters. However, this thesis would certainly be incomplete if the links between the calculated temperature histories and the final products properties were omitted. Therefore, in the present chapter some attention will be paid to these aspects.

4.1.1 A short note on orientation and stresses

In polymer literature there exists a widespread confusion about what is exactly understood by frozen-in orientation and residual stresses. We prefer to adopt the definition for orientation as given by Struik (1990, part IV, Ch.8) and call a polymer specimen "*oriented*" when the spatial distribution of its chain segments shows directions of preference.

Stresses which persist in the finished product after removal of their original driving force (such as temperature-, pressure- or flow field) will be called "*residual stresses*". These stresses are to be added to the external loads exerted on the specimen during its product life and are therefore an important item for the product quality.

The stresses which are exerted on the polymer molecules during flow (normal and shear stresses) are referred to as "*flow-induced stresses*". They may give rise to relatively large molecular orientations which are (partly) frozen-in upon solidification. The frozen-in orientation on its part causes a small entropic stress in the solidified product which will be called "*residual flow-induced stress*".

In addition to these flow-induced stresses, several other kinds of stresses may develop upon solidification. In amorphous polymers the most important ones are the thermal stresses and pressure-induced stresses. "*Thermal stresses*" (or "*cooling stresses*") are caused by (differences in) thermal contraction during solidification, resulting in a stress distribution in the finished product. Residual thermal stresses are typically compressive at the surface and tensile in the interior (see section 4.3). Such stresses are often thought to be a major stress component in injection moulded products. However, as will be shown below, this in reality is not the case. The stress distribution in injection moulded products is found to be almost entirely determined by the melt pressure history in combination with the solidified layer growth (section 4.4). In contrast to the thermal stresses, these residual "*pressure-induced stresses*" usually cause the surface layer to be under tensional strain, which is a rather undesired property since it enhances environmental stress cracking.

Before discussing the different kinds of stresses, we shall first address to the effect of a heating element on the orientation relaxation process.

4.2 Effect of heater on orientation relaxation[1]

4.2.1 Relaxation model

In order to understand the influences of surface heating on the final level of orientation an attempt is made to construct a simple qualitative model which still comprises all relevant parameters (i.e. initial temperature, heating time, heating power delay time, etc). We want to stress that it is certainly not our aim to develop an exact, quantitative model, but merely to predict several trends in the relaxation process.

Janeschitz-Kriegl (1977) and others (Dietz et al. 1978, White 1979) derived a simple expression which relates the injection rate, product thickness and solidified layer thickness to the flow-induced (shear)stress distribution at the end of filling, $\sigma_{tf}(x)$. Since this shear stress is assumed to be proportional to the Hermans orientation factor, relations between the processing parameters and the (frozen-in) orientation could be derived. The shear stress distribution is given by

$$\sigma_{tf}(x) = \mu_{00}(P,T)\left[\frac{\alpha v_{max}/D}{\tilde{D}_s^{\,2}}\right]^{\nu} . \frac{\tilde{x}}{\tilde{D}_s} \qquad (4.1)$$

All symbols are consistent with the ones used in the previous chapters. Note, however, that in this model the power-law viscosity μ_{00} (or better: the consistency index) depends on the pressure and the temperature. The basic idea behind the model is that as the solid layer grows, the effective channel thickness decreases, which on its turn increases the shear stress just before solidification. After the flow stops, the stresses in the hot core partially relax. In order to account for this relaxation, the authors used a Maxwell model eq.(4.2) with temperature dependent relaxation time,eq.(4.3). These equations were solved together with the energy equation eq.(2.2).

---

[1] reprinted from KMB Jansen and AAM Flaman, Nat.Lab Technical note 175/92

$$\sigma_{xz}(x,t) = \sigma_{tf}(x).\exp\left[-\frac{t_r(T,t)}{\tau_{R0}}\right] \tag{4.2}$$

with

$$t_r = \int_0^t \frac{dt}{a_T(T[x,t])} \tag{4.3}$$

here τ_{R0} and a_T denote the relaxation time constant at the initial melt temperature (T_{in}) and the temperature shift factor, respectively. t_r stands for the relaxation time *variable* (also known as the reduced time), evaluated at T_{in}. This t_r is a direct measure of the amount of relaxation. If $t_r=0$, no relaxation has occurred yet, whereas with increasing t_r the relaxation increases monotonically. Once evaluated numerically, this model adequately predicts the frozen-in orientation distributions normally found in injection moulded products (Dietz et al. 1978).

However, since our goal is not only to find an analytical estimate of the amount of relaxation, but also include the effects of the heating elements, some further simplification is inevitable. We will therefore assume μ_{00} to be constant and approximate the shift factor a_T by

$$a_T \cong e^{-\beta(T-T_{in})}, \tag{4.4}$$

$$\beta = -2.3 \left.\frac{d\log a_T}{dT}\right|_{T_{in}}$$

Clearly, a simple exponential relation such as eq.(4.4) will underestimate the shift factor at lower temperatures. However, since most relaxation occurs at the highest temperature, also near T_{in}, a β determined at T_{in} should give a reasonable approximation.

Next, the cooling history will be approximated by:

$$T_{cool} \cong T_{in} - qt \tag{4.5}$$

where the cooling rate, q, follows from the differentiation of eq.(2.19) with respect to time:

$$q \cong B(\ T_{1L}(t) - T_w\ ) \approx B(T_{in}-T_w), \qquad (4.6)$$

with $B = \frac{\pi^2}{4}\left(\frac{Bi}{Bi+1}\right)^2 \frac{a_1}{D_1^2}$

Note that since eq.(4.5) is not valid for very small times, q will be underestimated at first. On the other hand, for larger times T_{1L} will deviate from T_{in} and q is overpredicted. This effect may be compensated by the overestimation of the relaxation time at lower temperatures.

Expressions for the relaxation time, t_r and the final stress distribution, $\sigma^{t\infty}(x)$, are obtained by integrating eq.(4.3) and substituting this in (4.2):

$$t_r = \frac{1}{\beta q}\left[\ 1 - e^{-\beta q t}\ \right] \qquad (4.7)$$

and

$$\sigma^{t\infty}(x) = \sigma_{tf}(x).e^{\frac{-1}{\beta q \tau_{R0}}} \qquad (4.8)$$

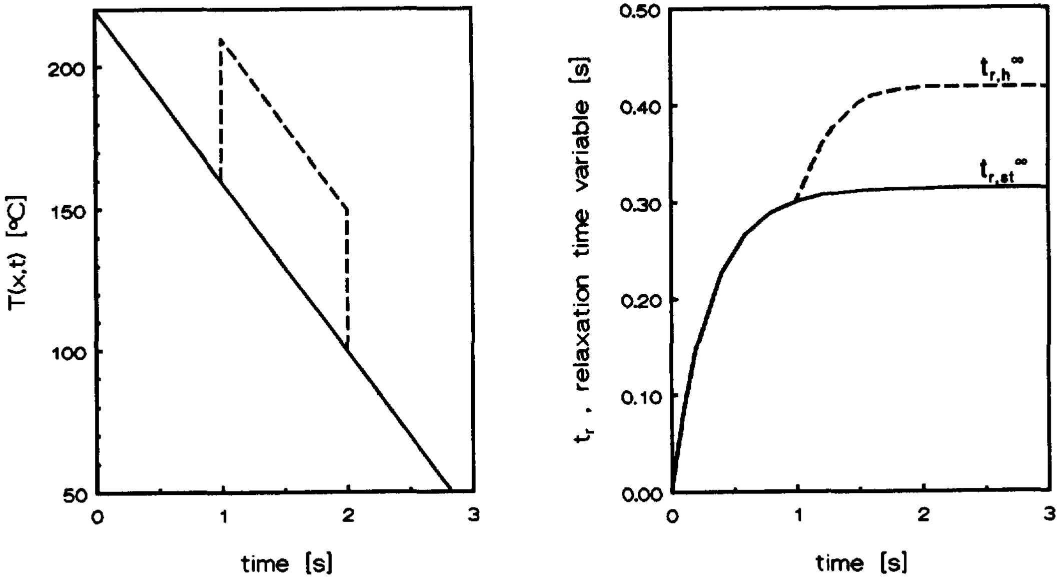

fig.4.1: Temperature curve (left) with and without heating pulse (dashed respectively full lines) and the effect on t_r (right).

An example of the influence of the temperature curve on the relaxation time variable is shown in fig.4.1 (full line). It is clear that as time proceeds and the temperature decreases, the relaxation process, characterized by t_r, slows down and effectively stops after a few seconds. The asymptotic value of the relaxation time is called t_r^{∞}. According to eq.(4.7) this t_r^{∞} is strongly dependent on the cooling history. High cooling rates and short relaxation times decrease the amount of orientation which is able to relax (see eq.4.8).

Eq.(4.8) is the (approximate) frozen-in flow-induced stress distribution. It is convenient to use this frozen-in stress distribution as a reference state and only consider the extra effects of a heating pulse.

Let, after a certain time interval t_d, the delay time, the heater be switched on for t_h seconds. Then at the polymer-mould interface an almost instantaneous temperature rise is encountered, followed by a much slower square-root-of-time increase (see also fig.5.2 and eq.2.25a). Although it is possible to perform the calculations with the complete eq.(2.25a), a simple "square" temperature pulse is thought to be sufficiently accurate for our purposes:

$$T_{heat} \cong \begin{cases} \Delta T_h & \text{for } t_d \le t \le t_h \\ 0 & \text{otherwise} \end{cases} \tag{4.9}$$

with

$$\Delta T_h = \frac{P_A}{1+\sigma_{14}} \frac{D_3}{\lambda_3} (1-x/D^*)$$

$$D^* = \frac{D_3/\lambda_3}{\sigma_{14}/\lambda_1}$$

Here D^* can be interpreted as a typical heater penetration depth which is about 0.7 mm in our case. If a pulse according to eq.(4.9) is applied, the integration of eq.(4.3) must be performed for each interval separately. The final relaxation time, t_{rh}^{∞}, is most conveniently written as:

$$t_{rh}^{\infty} = \frac{1}{\beta q} \left[1 + (1-f_{td}) f_{th} f_{\Delta Th} \right] \tag{4.10}$$

with

$$f_{td} = 1 - e^{-\beta q t_d}$$

$$f_{th} = 1 - e^{-\beta q t_h}$$

$$f_{\Delta Th} = e^{\beta \Delta Th} - 1$$

Here, the factors f_x are defined such that they are proportional to the arguments of the exponential functions, once these are small. We now arrive at our final expression for the influence of the heater parameters relative to the standard situation:

$$\sigma_h^{t\infty}(x) = \sigma^{t\infty}(x).\exp\left[\frac{-(1-f_{td})f_{th}f_{\Delta Th}}{\beta q \tau_{R0}}\right] \tag{4.11}$$

Eq.(4.11) clearly shows that if the delay time becomes too long ($t_d \gg 1/\beta q$), heating will hardly influence the orientation distribution. Further, if t_h becomes greater than $1/\beta q$, the effect of the heating time on the relaxation will decrease. On the other hand more heating power and a smaller delay time will result in an enhanced orientation relaxation.

4.2.2 Predictions and discussion

In this paragraph we will apply our relaxation model and compare the predictions of eq.(4.11) with measured orientation values. The moulding experiments and orientation measurements are described in detail in the next chapter. Here our interest is to study the effect of some processing and heater parameters on the final state of frozen-in orientation, illustrated for the point of maximum shear.

First we will look at the influence of the injection temperature, T_{in}. In the standard situation we have T_{in}=220 ^oC, which corresponds to a slope in the shift factor curve (fig.5.7) of β=0.053 [$^oC^{-1}$] and a relaxation time constant of about 0.6 s. The cooling rate was taken as 60 ^oC/s. Further, since the orientation relaxation will be evaluated at the position of the shear maximum, $x_1 \approx 0.2$ mm. Lowering the melt temperature will only slightly influence the cooling rate. Yet, the increase in relaxation time, evaluated at the new T_{in}, will be large (Eq.4.4 can be used to calculate this increase). As can be seen from fig.4.2, decreasing the melt temperature with 20 ^oC will result in an increase of the orientation level of about a factor 1.37 and a decrease of 35 ^oC gives a factor of 1.52. This is in moderate agreement with the experimentally observed factors 1.45 and 1.75. Note that the data point at 220 ^oC is in fact a reference point since this orientation level was used to scale both the model predictions and the experimental results.

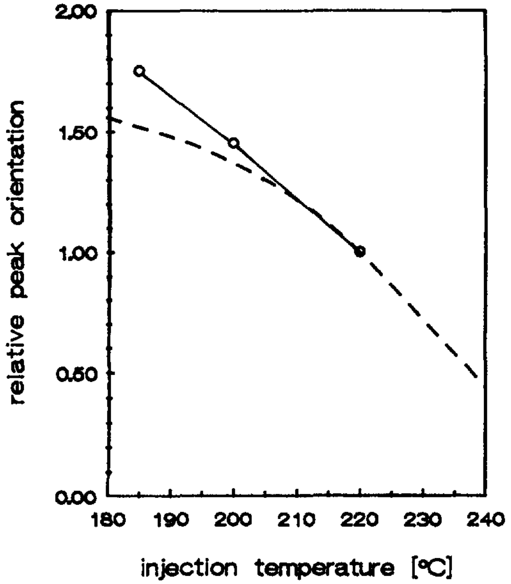

fig.4.2: Predicted effect of T_{in} on orientation relaxation. Symbols are measured values.

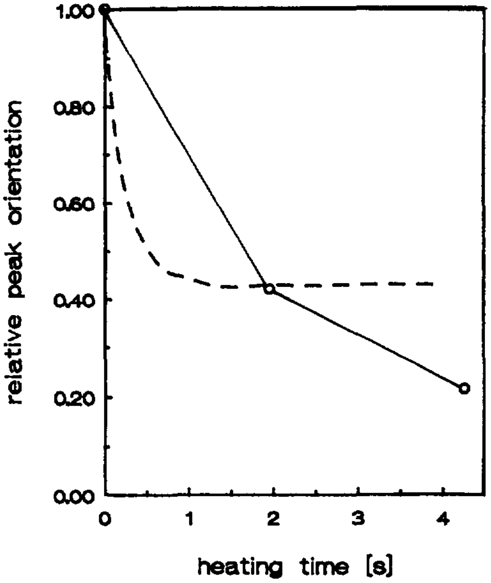

fig.4.3: Predicted effect of t_h on orientation relaxation . Symbols are measured values.

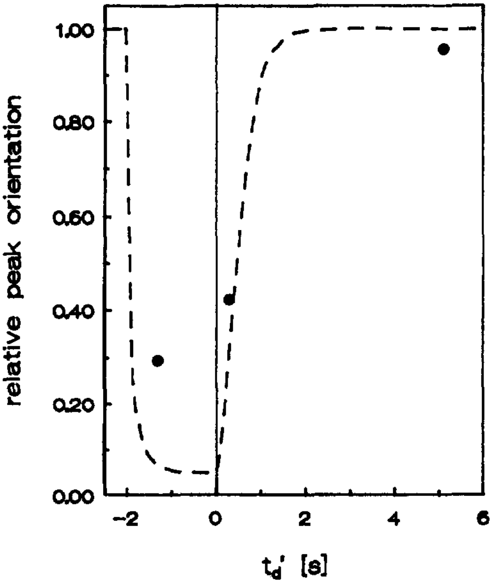

fig.4.4: Predicted effect of t_d' on orientation relaxation. Symbols are measured values. (No reference point included).

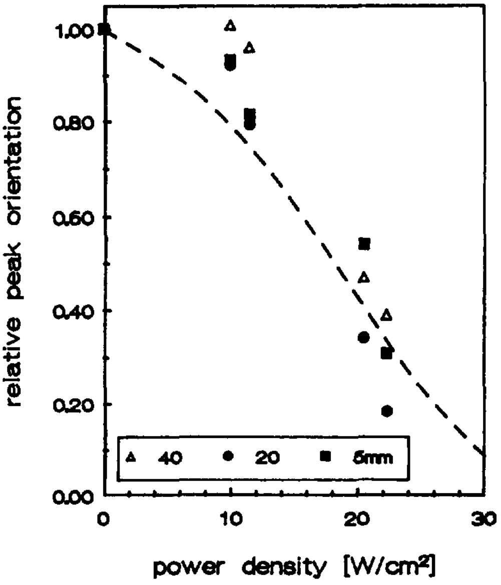

fig.4.5: Predicted effect of power on orientation relaxation. Symbols are measured values at different positions in the rectangular section (in mm).

Two remarks have to be made concerning t_d and t_h in eq.(4.10). Firstly, since the cooling process depends on the distance from the gate, we have to use the local delay time t_d':

$$t_d' = t_d + \frac{(L-z)}{\langle v_z \rangle} \tag{4.12}$$

Secondly, if the heating pulse starts before the melt is present, the effective heating time will be shorter. This effective heating time is defined by

$$t_h' = \begin{cases} t_h - |t_d'| & \text{if } t_d'<0 \\ t_h & \text{if } t_d' \geq 0 \end{cases} \tag{4.13}$$

An insulation layer thickness of 0.1 mm and a typical power density of 20 W/cm^2 result in a heating pulse at x_1=0.2 mm of ΔT_h = 36 ^{O}C. Most of the birefringence distributions are determined halfway the rectangular section, yielding a t_d' of: $t_d' = t_d + 0.4$.

Fig.4.3 shows that most of the orientation relaxation occurs during the first second of the heating pulse. This can be understood by considering the temperature history at the point of interest, x_1=0.2 mm. Initially this temperature is about 200 ^{O}C, which is still far above the solidification temperature, thus enabling rapid relaxation. After two seconds of cooling ($q \approx 60$ C^O/s) the temperature drops to about 80 ^{O}C, being well below the solidification temperature (100 ^{O}C). The additional temperature increase of the heater ($\Delta T_h \approx 36$ ^{O}C) is then hardly enough to enable orientation relaxation.

The predictions of such a fast initial relaxation (dashed line in fig.4.3), in fact overestimate the real relaxation process since the square-root-of-time increase of the heater temperature was disregarded in our model. This seems to be confirmed by the measurements (symbols in fig.4.3).

However, one has to be careful with the interpretation of the measured values as plotted in fig.4.3, since these were not performed at exactly the same delay time (see table 5.4). And, according to fig.4.4, small deviations near t_d'=0.4 will result in large deviations in orientation relaxation.

The delay time curve of fig.4.4 (dashed line) consists of two main parts, related to a negative and positive t_d' (eq.4.12). If the entire heating pulse is applied before the melt enters the cavity, the effect on the orientation relaxation is negligible (see eq.4.13). As soon as there is an overlap between the heating pulse and the presence of the melt in the cavity (i.e. $t_h' > 0$), the relaxation due to an increase in delay time parallels the relaxation due to an increase in heating time (fig.4.3). In the second part ($t_d' > 0$) the heating pulse is completely effective ($t_h' = t_h$). It then turns out that the later in the cooling process the heater is switched on, the less orientation relaxes.

If we now consider the complete predicted relaxation curve (dashed line in fig.4.4), we observe a strong minimum in the residual orientation near delay times corresponding to $t_d' = -1$ s. I.e., *the most effective heating pulse is that which includes the filling stage completely.* This is an important practical conclusion. Such a typical dependence of the relaxation on the delay time is not due to the approximating assumptions in our model, but seems to be a realistic prediction. Evaluation of the orientation relaxation with more accurate descriptions of the temperature shift factor, the heater temperature and cooling process will only alter the slopes near $t_d' = 0$ and $t_d' = -2$ s. to some extent. The minimum, however, remains.

The few measured values (symbols in fig.4.4) seem to confirm the predicted dependence of the relaxation on the delay time. Note that in this case none of the points is a reference point.

In fig.4.5 the effect of the power density is shown. As can be seen a gradual decrease of the orientation with increasing heating power is predicted (dashed line). Experimental results obtained along the flow path show a marked scatter which is probably due to differences in local heating power (compare with photos 5.1 and 5.2). The predicted curve, however, agrees reasonably well with the measurements.

4.3 Thermal stresses (constant pressure)

4.3.1 Stress calculation

Residual thermal stresses arise when a piece of material is cooled inhomogeneously and when the cooling moreover causes it to stiffen. The inhomogeneity of the cooling process is responsible for the thermal (expansion) stresses; the change of the elastic properties during solidification causes the stresses to persist after the cooling has been completed (Struik (1990)). This is best illustrated by considering the surface layers and the core region of the specimen separately. When the surface cools and contracts, the centre is still hot (i.e. behaves as a liquid) and the stresses produced there relax. Thus at that stage the surface layers are (almost) stress free because they were allowed to contract, whereas the core is free of stresses due to its viscous nature. In a subsequent cooling stage the centre solidifies and contracts, which causes the surface layers to get under compression.

Stress model

Many authors have tried to translate this physical picture in a mathematical model. A review of some of the theories used for predicting residual stresses in quenched inorganic glass is given by Isayev (1987). In addition, an excellent treatment on cooling stresses is given in Struik's recent book (Struik 1990, part III). Here we will only mention the result of Struik's most simple cooling stress model which assumes that the modulus of elasticity, E, is constant below the solidification temperature (T_s) and zero above that temperature (*elastic solid model*). This model still comprises the physically relevant issues and is simple enough to allow for analytical solutions. Let α_v, ν_p, D_s, t_{sx} and t_{s1} denote the volumetric thermal expansion coefficient, Poisson constant, solidified layer thickness, the time the solidification front reaches position x and the moment of complete solidification, respectively. Then the residual thermal stress distribution for a flat plate is given by

$$\sigma_T(x) = \frac{\alpha_v E}{1-\nu_p}\left[\int_{t_{sx}}^{t_{s1}} \frac{1}{\hat{D}_s} \int_0^{\hat{D}_s} \frac{\partial T}{\partial t'}\, d\hat{x}'dt' - (T(x,t_{s1})-T_s) \right]$$
$$+ \frac{\alpha_v E}{1-\nu_p}\left[T(x,t_{s1}) - \overline{T(t_{s1})} \right] \qquad (4.14)$$

The bar denotes averaging over the thickness. From eq.(4.14) it thus follows that $\sigma_T(x)$ may be considered as consisting of two separate parts. The first part, further referred to as $\sigma_{T1}(x)$, comprises the stresses developed during the initial cooling stage, and the second part, $\sigma_{T2}(x)$, the stresses formed from the moment of complete solidification onwards.

With eq.(2.3a) as a solution for the temperature distribution during the first cooling stage, σ_{T1} is easily calculated (Goslinga 1980). This solution, however, is not valid near the product surface and is usually much smaller than the σ_{T2} part. Therefore, as a first approximation, only the second part will be considered from now on. Using eq.(2.4a) we then arrive at

$$\sigma_T(x) \cong \frac{\alpha_v E}{1-\nu_p}(T_{in}-T_s)\left[\ \cos(\tfrac{\pi}{2}\tilde{x}) - \frac{2}{\pi}\ \right]. \tag{4.15}$$

Thus the residual quenching stresses are roughly proportional to the difference between the solidification temperature and the wall temperature. Furthermore, the stress profile is parabolic like $(\cos(\frac{\pi}{2}\tilde{x})\cong 1-1.23\tilde{x}^2\ )$ and the stresses are tensile in the centre of the slab and compressive at the surfaces. Such stress distributions have been reported by many experimentalists (see e.g. Isayev (1987) and Struik (1990)).

4.3.2 Warpage due to asymmetrical cooling

It is not uncommon in polymer processing that there exist small non-uniformities during the cooling process. This will lead to an unbalanced residual stress distribution and, if the part is not restricted in its movements, warpage of the part. In order to calculate the radius of curvature, R, due to quenching of a hot material between two walls with different temperature, we first need to know the effect of this temperature difference, ΔT_w, on the temperature distribution. Using standard techniques (e.g. Carslaw and Jaeger 1988, Kreyszig 1988) this turns out to be

$$\tilde{T}(\tilde{x},\tilde{t}) = \tilde{x}.\frac{1}{2}\Delta\tilde{T}_w + \frac{4}{\pi}\cos(\tfrac{\pi}{2}\tilde{x}).e^{-\pi^2\tilde{t}/4} - \frac{\Delta\tilde{T}_w}{\pi}\sin(\pi\tilde{x}).e^{-\pi^2\tilde{t}} + \ldots \tag{4.16}$$

with

$$\Delta\tilde{T}_w \equiv \frac{T_{wr}-T_{w\ell}}{T_{in}-T_{w0}}, \quad T_{w0}\equiv(T_{wr}+T_{w\ell})/2, \quad \tilde{T}\equiv\frac{T-T_{w0}}{T_{in}-T_{w0}}$$

Here T_{wr} and $T_{w\ell}$ refer to the right and the left wall temperature respectively (see also fig.4.6a). The moment, *M*, exerted by the unbalanced stress distribution is calculated as

$$M_{\sigma_{T2}} = 2W\int_{-1}^{1}\tilde{x}.\sigma_{T2}d\tilde{x} = 2W\frac{\alpha_v E}{1-\nu_p}\Delta T_w\left[\ \frac{1}{3} - \frac{\pi^2}{128}\tilde{T}_s^4\ \right], \tag{4.17}$$

and is balanced by the bending moment (e.g. Landau and Lifshitz 1986, Ch.2)

$$M_{\sigma_{bend}} = 2W\cdot\frac{2}{3}\ \frac{D.E_\infty}{(1-\nu_p)R} \tag{4.18}$$

thus for the curvature $\kappa_{warp}\equiv 1/R$ we obtain the rather simple expression

$$\kappa_{warp} \cong \Delta T_w\frac{\alpha_v E}{2D.E_\infty} \tag{4.19}$$

This is an important result, since it means that the curvature due to warpage scales linearly with the wall temperature difference and the thermal

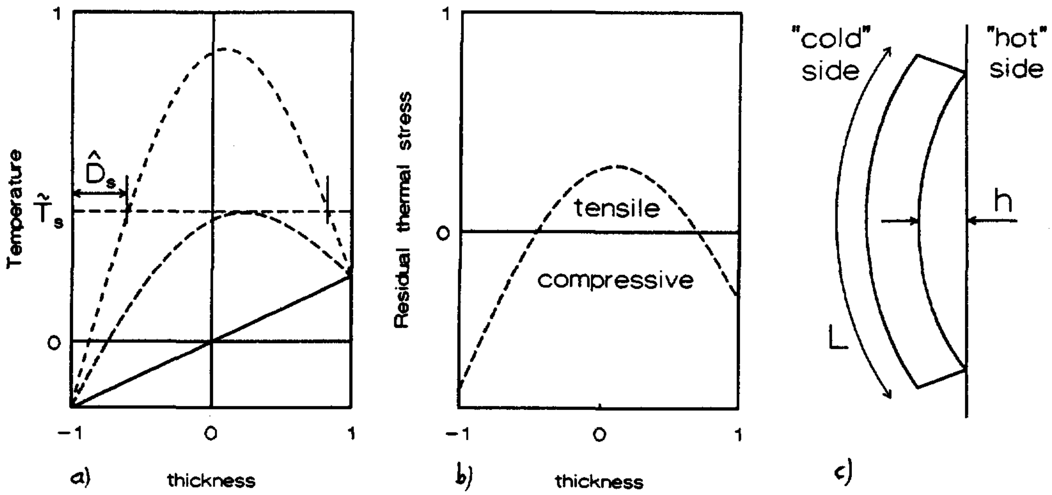

fig.4.6: Warpage by unbalanced cooling. a) Temperature distribution; b) Final stress distribution; c) Warpage towards the hottest side.

expansion coefficient and is inversely proportional to the sample thickness.

Note that the bending occurs at a different temperature than the stress formation, which might require a different modulus of elasticity (here referred to as E_∞). We further remark that eq.(4.19) is not only valid for flat plates, but also holds for thin rods or strips, since in that case the correction factor $(1+\nu_p)^{-1}$ appears in both eqs.(4.17) and (4.18).

In practice, sometimes the height of deflection, h (see fig.4.6.c), rather than the curvature is used. If the curvature is assumed to be perfectly circular, the deflection follows from geometrical considerations:

$$h = R(\ 1 - \cos[L/2R]\ ) \cong L^2/8R = \tfrac{1}{8}L^2\kappa_{warp}, \qquad (4.20)$$

where L is the length of the product (see fig.4.6c).

Example

Let us now illustrate the calculations above by considering the quenching of a 30 cm long polystyrene ruler, in perfect contact with two walls which differ 10 K in temperature. The half-thickness, D, is 1 mm. Assuming that $E=E_\infty$ and that $\alpha_v=2.10^{-4}$ K^{-1} (Oberbach 1980), gives for the curvature (eq.4.19) $\kappa_{warp} \cong 1\ m^{-1}$ and the deflection: $h \cong 1.1$ cm. It should be noted that the product is curved towards the side which was hottest during the stress formation (compare with fig.4.6c).

4.4 Pressure-induced stresses in injection moulded products

4.4.1 Stress calculation

In injection moulded products not only thermal stresses build up during solidification but also the varying melt pressure and the viscous flow cause additional stress contributions. For simplicity we will (again) assume linear elastic behaviour in the solidified part and purely viscous behaviour in the melt. This enables us to treat the different stress contributions separately. Of course, in practical situations, viscoelastic effects such as plastic deformation and stress relaxation are likely to occur, but the simple elastic approach is thought to still comprise the most relevant issues. We further neglect the residual flow-induced stresses which are about a factor 10^2 smaller than (the sum of) the other contributions (Baaijens (1991)). The residual stresses in injection moulded products are then given by the sum of the residual constrained quenching stresses (with zero pressure) and the stresses due to a varying melt pressure. These two contributions are discussed below.

Residual stresses in the constrained quenching case

The residual thermal stresses due to free quenching exist by virtue of the shrinkage (contraction) of the outer layers during the first part of the cooling process. Due to this contraction (most of) the stresses in the solidified outer layers could relax, which caused a nett residual stress after the subsequent contraction of the core. If the shrinkage of the outer layers is prevented, however, these layers become under tensional stress after the first cooling stage. In the second cooling stage the core cools from the same initial temperature to the same final temperature as the outer layers did during the first stage. Therefore, the thermal contractions are identical and the final stress distribution is uniform. After removal of the constraints at the outer surfaces (ejection from the mould in case of injection moulding) the product shrinks and the stresses vanish.

This simplified two-layer model can easily be generalized to a slab consisting of an arbitrary amount of thin layers (but still assuming the elastic-solid material behaviour). The essential point is that the stress build-up starts as soon as the temperature falls below T_g (which is the same for every layer) and that the temperature distribution after the cooling process is (usually) uniform. Furthermore, since in the solid phase time effects are neglected, the cooling rate (which differs for every layer) has no influence on the stress formation. Thus, if the final temperature is uniform, the stress distribution will be too and will vanish after removal of the constraints. This holds irrespective of a possible temperature dependency of E, ν_p and α_V.

If we would further generalize towards real visco-elastic material behaviour time effects would become more important, resulting in a non-zero residual stress distribution. As was shown experimentally by Wimberger-Friedl (1991, p.133), these residual stresses are not too large (about 2 MPa compression near the walls and almost no stress in the centre). Note that even in case of visco-elastic modeling the constrained quenching case is much simpler than the free quenching case because for thin constrained specimen the strains perpendicular to the thickness direction can be neglected everywhere.

During the solidification of an injection moulded product, shrinkage of the solidified layer is prevented by two mechanisms. Firstly, adhesion to the mould walls refrain (at least the outer skin of) the solid layers from moving, and secondly, the newly formed solid surface will be kept fixed by the stretching force of the melt pressure (see Fig.5 and Titomanlio (1987)). Therefore, although thermal stresses develop during the moulding process, no *residual* thermal (quenching) stresses will be present in the as-moulded part (at least for the elastic-solid material behaviour assumed here).

Doubts about the importance of the thermal stress contribution to the residual stresses in injection moulded products were already reported by Douven ((1991) p.107) and Wimberger-Friedl ((1991) p.129-136).

Pressure-induced stress model

Titomanlio et al. (1987) were the first who recognized the importance of the melt pressure on the residual stresses in injection moulded products. They used the same elastic-solid model and thermal model as we do and solved the equations numerically, probably because at that time it was not yet realized that the constrained quenching stresses vanish for elastic-solid models. Here we will give a simplified derivation of their model.

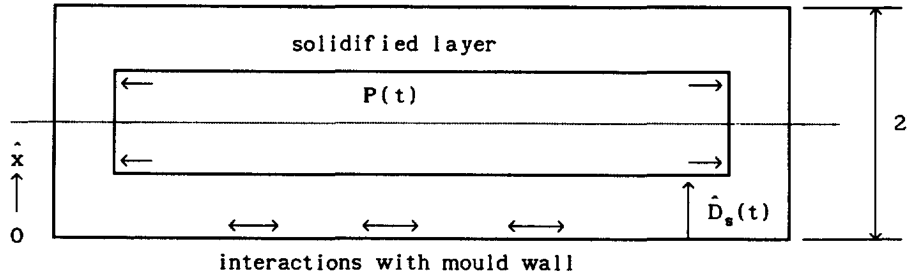

fig.4.7: Schematic view of a constrained solidifying slab.

We start with the solidifying rectangular slab as is depicted in Fig.5. At the solid-melt interface each volume element is under hydrostatic pressure. As the solidification front proceeds and this layer becomes solid the mutually perpendicular frozen-in strains at that surface (denoted by ε_{xx}, ε_{yy} and ε_{zz}) become in general (e.g. Landau and Lifshitz (1986))

$$\begin{aligned} \varepsilon_{xx} &= \frac{1}{E} [\ \sigma_{xx} - \nu_p(\sigma_{yy}+\sigma_{zz})\ ] \\ \varepsilon_{yy} &= \frac{1}{E} [\ \sigma_{yy} - \nu_p(\sigma_{xx}+\sigma_{zz})\ ] \\ \varepsilon_{zz} &= \frac{1}{E} [\ \sigma_{zz} - \nu_p(\sigma_{xx}+\sigma_{yy})\ ] \end{aligned} \tag{4.21}$$

Here E, ν_p and σ_{ii} represent the modulus of elasticity, the Poisson constant and the elongation stress in direction i. These elongation stresses all equal minus the melt pressure: $\sigma_{xx}=\sigma_{yy}=\sigma_{zz}=-P(t)$. Here we neglect normal flow induced stresses. Eq.(4.21) then simplifies to

$$\varepsilon_{xx} = \varepsilon_{yy} = \varepsilon_{zz} = -\ \frac{1-2\nu_p}{E} P(t), \qquad \text{at the solid-melt interface} \tag{4.22}$$

The pressure at the solid-melt interface is sometimes called the formation pressure, P_f, which in general differs for each subsequent layer x. Therefore the frozen-in strains depend on x, rather then on the time. The frozen-in strains, ε_{ii}, are then given by

$$\varepsilon_{ii}(x) = -\ \frac{1-2\nu_p}{E} P_f(x). \tag{4.22a}$$

At the moment of ejection the product is free to expand (or shrink) in all directions until stress equilibrium is reached. This expansion is proportional to the average value of eq.(4.22a). Furthermore, because the thickness is much smaller than the other two dimensions, the stress in thickness direction can be neglected and we have a typical plane stress situation after ejection (σ_{yy}=σ_{zz} and σ_{xx}=0). The residual pressure-induced stress contribution then becomes

$$\sigma_{yy}(x) = \sigma_{zz}(x) = -(1-2\nu_p)[\ P_f(x) - \overline{P_f(x)}\ ] \qquad (4.23)$$

The bar above the last term means averaging over the thickness. Note that this expression is independent of the modulus of elasticity, E. It should be remarked that whether the final situation is purely plane stress or not only affects the front factor in eq.(4.23).

Effect of the pressure history

There are three ways of dealing with the pressure history. The first, and most accurate one, is to use a recorded pressure curve of an injection moulding experiment. This, of course, is only possible if this experimental data is available and cannot be used to predict stress distributions from scratch. Secondly, a pressure curve predicted by numerical simulations can be used. And, thirdly, the pressure curve can be approximated by dividing it into three separate periods corresponding to the filling, holding and cooling stage of the injection moulding process (see also Greener (1986) and Titomanlio (1987)):

$$P(t) = \begin{cases} P_0 . t/t_0 & \text{I : } (0 \le t < t_0, \text{ filling}) \\ P_m & \text{II : } (t_0 \le t \le t_1, \text{ holding}) \\ P_\infty + (P_m - P_\infty) e^{-\beta_0^2(\tilde{t}-\tilde{t}_1)} & \text{III: } (t \ge t_1, \text{ cooling}) \end{cases} \qquad (4.24)$$

In order to show the effect of these different approaches on the predicted stress distributions we consider injection moulding experiment A_{200} (details in next chapter). During this experiment the pressure was measured at 74 mm from the end of the flow path (full line in fig.4.8). This pressure curve is approached according to eq.(4.24) with P_0=10 MPa, P_m=42 MPa, P_∞=0, t_0=0.7 s and t_1=2.7 s (dashed line).

Such a simplified pressure history still bears some physical relevance, since for rectangular cavities the pressure during filling in practice indeed increases almost linearly with time. Further, also the sharp change in pressure which marks the boundary between the filling stage and the holding stage is quite realistic. The change from stage II to III, however, is in practice more gradual (see fig.4.8). t_0 and t_1 correspond to the (local) filling time and the "gate freeze-off time" respectively. In this case the flow front velocity (v_z) was about 109 mm/s, suggesting a $t_0=\Delta z/v_z \cong 0.7$ s.

Further, P_0, P_m and P_∞ denote the pressure just before filling is completed, the (maximum) melt pressure in the holding stage and the pressure as $t \to \infty$. The exponential decay in period III and the value of P_∞ follow from the assumption that at t_1 the gate suddenly freezes-off and no extra material could enter the cavity. In that case the pressure decreases proportional to the average temperature (as calculated from e.g. eq.(2.4a) or 2.19). What is essential is that the value of β_0 used in eq.(2.24) is identical to the β_0 appearing in the solution of the temperature field and therefore cancel in the calculation of the formation pressure. Only in case of mould elasticity the pressure decreases much slower than the average temperature (Baaijens (1991)).

The formation pressure $P_f(x)$ is obtained by plotting the pressure (as obtained in one of the three ways mentioned above) against the solidified layer thickness. A second possibility is to substitute the time before solidification, denoted by t_{sx}, in the pressure curve, P(t). Both the solidified layer thickness, $\hat{D}_s(t)$ and the time before solidification are obtained by inverting the expression $T(x,t)=T_s$ (Chapters 2 and 3).

As an example the pressure history given by eq.(4.24) will now be used to calculate the formation pressures and the stress distribution. The time before solidification is calculated from the "erf"-solution (eq.2.3a) for period I and from eqs.(2.19) or (2.4a) for period II and III. This yields for the formation pressures

$$\text{I} \;:\; P_f(\hat{x}) = P_0\left(\frac{\hat{x}}{\hat{D}_{s0}}\right)^2$$

$$\text{II} \;:\; P_f(\hat{x}) = P_m$$

$$\text{III} \;:\; P_f(\hat{x}) = P_\infty + (P_m - P_\infty)\left[\frac{\sin(\frac{\pi}{2}\hat{D}_{s1})}{\sin(\frac{\pi}{2}\hat{x})}\right], \tag{4.25}$$

where

$$\hat{D}_{s0} \equiv \hat{D}_s(\tilde{t}_0) \cong \tilde{T}_s\sqrt{\pi\tilde{t}_0},$$

$$\hat{D}_{s1} \equiv \hat{D}_s(\tilde{t}_1) \cong \frac{2}{\pi}\arcsin(\frac{\pi}{4}\tilde{T}_s . e^{\beta_0^{2}\tilde{t}_1}).$$

Note that we used $\beta_0=\pi/2$ and $\cos(\beta_0\tilde{x})=\sin(\beta_0\hat{x})$ for simplicity. If β_0 is somewhat smaller than $\pi/2$ (corresponding to $Bi<\infty$, see appendix A) a few additional terms become necessary. The residual pressure-induced stress distribution is obtained by substituting eq.4.25 into eq.4.23. The average formation pressure is given by

$$\overline{P_f(x)} = \frac{1}{3}P_0\hat{D}_{s0} + P_m(\hat{D}_{s1}-\hat{D}_{s0}) + P_\infty(1-\hat{D}_{s1}) - \frac{2}{\pi}(P_m-P_\infty)\sin(\frac{\pi}{2}\hat{D}_{s1})\ln[\tan\frac{\pi}{4}\hat{D}_{s1}] \tag{4.26}$$

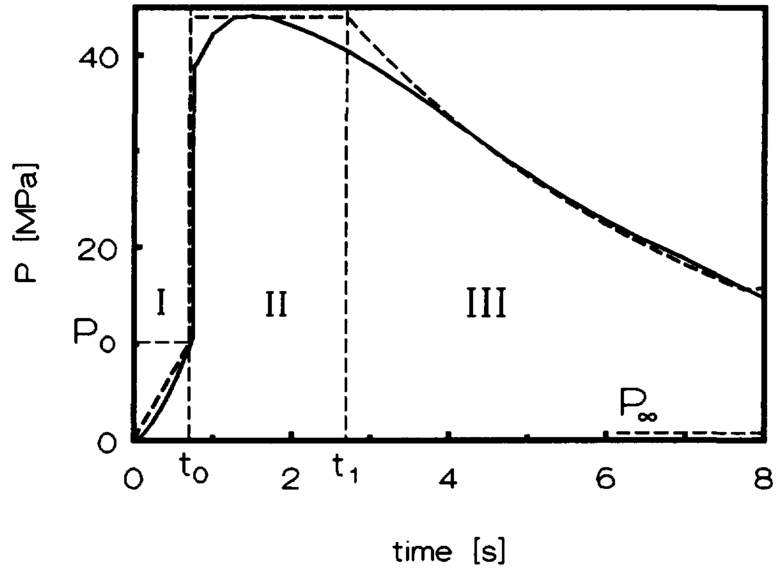

fig.4.8: Comparison between measured and approximated pressure curve. Full line: pressure curve P_3 measured during injection moulding experiment A200 (see Ch.5); Dashed line: approximation according to eq.(4.24) with t_0=0.7 s., t_1=2.7 s., P_0=10 MPa, P_m=42 MPa, P_∞=0 and a=8.3x10^{-8} m^2/s.

Measured versus predicted stress distributions

In fig.4.9 two residual stress distributions, predicted by eq.(4.23) are shown. The simplified curve obtained with the formation pressure as given by eq.(4.25) (dashed line) compares extremely well with the more accurate prediction (full line: measured pressure curve and numerically calculated solidified layer growth, including convection and dissipation effects). In fig.4.9 also the different zones (I, II and III) are indicated, which facilitates a study of the relative importance of the different injection moulding stages. Although the local filling time can be small (especially near the end of the flow path), the initial layer growth is fast (see fig.2.1), resulting in a considerable contribution in the stress distribution. It is therefore wrong to neglect zone I in eq.(4.24). According to eq.(4.25) the surface stresses vary quadratically with $\hat{x}$. Due to a fast layer growth during the filling and the (end of the) cooling stage, the

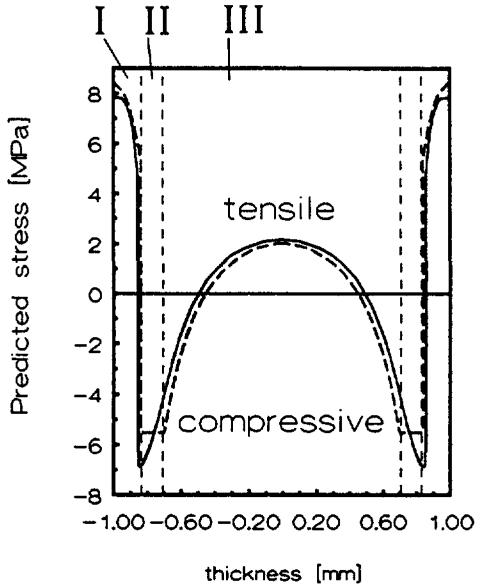

fig.4.9: Predicted stress distributions according to eq.(4.23) with the pressure curves as depicted in fig.4.8. Full line: formation pressure from measured pressure curve and numerically predicted solidified layer thickness; Dashed line: approximate formation pressure according to eq.(4.25). The numbers I, II and III correspond to the injection, holding and cooling stage.

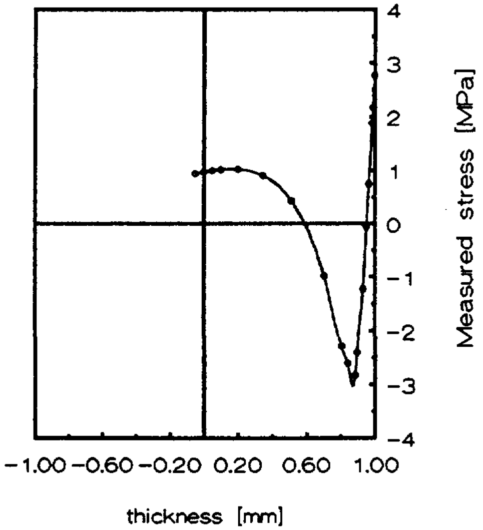

fig.4.10: Measured stress distribution (Layer Removal Method) of an injection moulded polystyrene strip (A200, see Ch.5). E=3400 MPa and ν=0.33.

contribution of the holding stage (zone II) turns out to be relatively small. Further, the stresses in the centre vary proportional to $1/\cos(\frac{\pi}{2}\tilde{x})\cong 1+1.23\tilde{x}^2$ which explains the parabolic like behaviour. Clearly this parabolic profile has very little to do with the parabolic quenching stress distribution according to eq.(4.15).

The shape of the thus predicted stress distributions compares well with the measured stress distribution as is shown in fig.4.10 (details about the Layer Removal measurements refer to section 5.5). The predictions, however, overestimate the measurements with about a factor of 2. The same amount of overestimation was reported by Douven (1991, §6.4) who compared numerical viscoelastic stress calculations with measured stress distribution in injection moulded products. The overestimation is most probably not due to approximations in the pressure curve or the solidified layer growth, but can be caused by stress relaxation or a wrong value for the modulus of elasticity, E. Note that the predicted stress curves do not depend on this modulus, whereas the measured stress curve is proportional to it.

Technological implications

Although free quenching stresses and injection mouding stresses are of the same order of magnitude (about -10 to 10 MPa) and both cases show a parabolic like profile near the centre of the product, the surface stresses are completely different. In case of extruded (or free quenched) products these surface stresses are compressive, whereas injection moulded products show a surface layer which is of tensional nature. This implies that injection moulded products are much more sensitive to environmental stress cracking than extruded products.

Furthermore, both theory and measurements indicate that the residual stress distribution in injection moulded products rapidly changes over the thickness. The rather sharp boundary between the first tensional zone and the subsequent compressive layer (zones I and II in fig.4.9) is -if we disregard stress relaxation for a moment- in practice quite realistic, since it is directly related to the fast pressure change at the end of filling. The technological implications of such sharp boundaries can be quite severe. *The injection moulded product in fact behaves as composite material*, consisting of 3 or more layers which will respond differently to an imposed force field. This effect is further enhanced by the presence of a large uniaxial orientation in layer I. The laminar-like behaviour will show up most clearly in extreme cases as crazing and stress cracking.

We want to conclude this paragraph with two more remarks. Evidently, the rather "edged" stress curve of fig.4.9 will smooth out somehow in practical situations. And, secondly, the solidification temperature (or the "no-relaxation temperature") for stresses is not necessarily the same as the glass transition temperature or the temperature below which orientation relaxation is effectively inhibited. Therefore the solidified layer thicknesses used in this paragraph may differ from the ones related to orientation.

4.4.2 Warpage due to asymmetrical cooling

In view of the complex shapes of injection moulded articles it is not always possible to insert cooling channels at the most optimal locations. Therefore (small) differences in the mould wall temperature are easily encountered. Such temperature differences usually lead to additional residual stresses or unwanted deformations. The calculation of the warpage of an injection moulded plate with eq.(4.24) as a pressure curve, proceeds similar to the calculation in paragraph 4.3.2. In this analysis we use the following relations:

$$\int(x/\sin x)dx \cong x-x^3/18 -\ldots, \qquad \ln[\tan(\tfrac{1}{2}(x+\varepsilon))] = \ln[\tan(\tfrac{1}{2}x)] + \varepsilon/\sin(x) -\ldots$$

and the fact that "even" terms do not contribute to the warpage. Neglecting the higher order terms of $\Delta\tilde{T}_w$, the result finally becomes

$$\kappa_{warp} \cong \frac{-3(1-\nu_p)}{E_\infty D}(1-2\nu_p)\left\{\hat{D}_{s0}\delta_0\left[(P_m-\tfrac{1}{3}P_0)(1-\hat{D}_{s0}) + \tfrac{1}{6}P_0\hat{D}_{s0}\right] + \right.$$
$$\left. + \delta_1(P_m-P_\infty)\cos(\tfrac{\pi}{2}\hat{D}_{s1})\left[\ln\tan\tfrac{\pi}{4}\hat{D}_{s1} + 1-\hat{D}_{s1} - \tfrac{\pi^2}{72}(1-\hat{D}_{s1}^3)\right]\right\} \qquad (4.27)$$

with

$$\delta_0 \cong \tfrac{1}{2}\Delta\tilde{T}_w(\tilde{T}_s^{-1}-1),$$

$$\delta_1 = \frac{\Delta\tilde{T}_w}{\pi\tilde{T}_s}.\frac{u}{\sqrt{1-u^2}}.(1-\hat{D}_{s1}), \qquad u\equiv(\tilde{T}_s/C_0)e^{\beta_0{}^2\tilde{t}_1} = (\tfrac{\pi}{4}\tilde{T}_s)e^{(\pi^2/4)\tilde{t}_1}\ .$$

From eq.(4.27) it follows that again warpage is proportional to $\Delta\tilde{T}_w/E_\infty$. The effect of the pressure dependence, however, is not straightforward and the full equation (4.27) should be used to evaluate κ_{warp}. Note that for the warpage of strips instead of planes an extra factor $(1+\nu_p)$ has to be added.

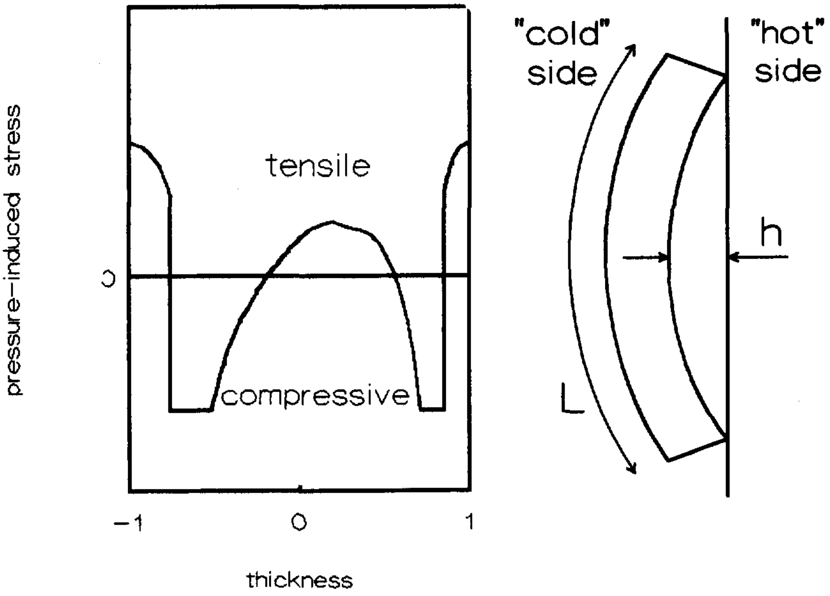

***fig.4.11**: Warpage due to asymmetrical cooling in injection moulding.*

(Left) residual pressure-induced stress distribution due to asymmetrical cooling; (Right) warpage towards the hottest side.

Example

As an illustration we will calculate the warpage of the ruler of the previous example, but now in case of it being injection moulded. Let T_{in}=200°C, T_w=50°C, T_s=100°C, P_m=60 MPa, $P_0=P_\infty$=10 MPa, t_0=1 s., t_1=4 s., E_∞=3400 MPa, ν_p=0.33, and ΔT_w=10°C. Then, with a=0.083 mm^2/s, $\hat{D}_{s0}$, $\hat{D}_{s1}$ and κ_{warp} respectively become 0.14, 0.30 and 0.083 m^{-1}, whereas the height of deflection, h, is about 1 mm. Comparing these results with the quenching case shows that the injection moulded ruler warps about a factor 12 less than the quenched ruler. The ruler again warps towards the hottest side (see fig.4.11).

Acknowledgements

The author is grateful to ir. P. Schoone of Philips CFT for his numerical (Inject 2) calculations leading to the more realistic prediction of the solidified layer thickness as used in fig.4.9.

CHAPTER 5

REDUCTION OF FROZEN-IN ORIENTATION AND RESIDUAL STRESS

5.1 Heater design[1]

In this section first several global requirements for heating elements which can be used for reduction of frozen-in orientation in injection moulding will be discussed. After that a more detailed analysis of the various design parameters is given.

The most important requirements are related to the desired temperature rise and pulse duration, which determine the amount of orientation (and stress-) relaxation. In general, the melt temperature must be well above the glass transition during an interval comparable to the relaxation time at that temperature. As relaxation times usually are not commonly available and strongly depend on the polymer at use, a more practical condition is that the mould temperature should be kept above the glass transition during the filling stage. In this way the growth of the highly oriented layer is prevented, which clearly results in low oriented products. After the filling stage (which is about one second) the product should cool as fast as possible in order stay economically relevant. This requires fast surface temperature changes, indicating that the heater should be situated directly below, or at the mould surface.

Next, to achieve a uniform orientation relaxation, the heat production should be homogeneously distributed over the heater surface. A heating element consisting of several parallel heating wires therefore does not seem to be suitable for this specific purpose. Application in injection moulding machines further requires some additional features. The conditions which should be fulfilled under common injection moulding circumstances are summarized below.

1 a surface temperature which is about 50 to 100 °C above its initial value during one or two seconds;

2 a limited increase in cycle time after heating of, say, 20%;

3 a homogeneous plane heating source;

4 proof against large shearing forces and pressures up to 1000 bar;

---

[1] KMB Jansen and AAM Flaman, submitted to Polym. Eng. Sci.

5 a smooth, wear resistant, upper surface which shows little interaction with the injected polymer.

A heating element satisfying all the requirements consists of a steel mould wall, an insulation layer, a heat producing layer and a protective coating. The insulation layer provides both electrical and thermal insulation. The thickness of this layer is a major design parameter as will be pointed out later on. The heat production is realized by resistance heating, requiring an electrically conducting layer.

Polyimide foils were used as insulation layers, mainly because of their excellent thermal stability. A sputtered metal layer was found to be too vulnerable as a heat producing layer and a carbon filled resin was used instead. The top layer consists of a thin (10 μm) polyimide film.

In order to determine the required layer thicknesses, we use the expression for the contact temperature rise at the polymer-heater interface as given in section 2.3

$$\Delta T_1(0,t) = \frac{P_A}{1+b_1/b_4}\left(\frac{2\sqrt{t}}{b_4\sqrt{\pi}} + \frac{D_3}{\lambda_3}\right) \qquad t>0.3 \text{ seconds} \qquad (5.1)$$

Here P_A, b, D and λ denote the power density, heat penetration coefficient ($\equiv\sqrt{\lambda\rho c_p}$), layer thickness and thermal conductivity respectively. The subscripts 1, 3 and 4 refer to the polymer, insulation and mould layer, respectively. The first term shows a square root of time dependent temperature rise and is mainly affected by the thermal properties of the mould ($b_1 \ll b_4$). In literature, typical power densities of about 20 W/cm^2 are reported (see also table 1.1), while the heat penetration coefficient of the steel mould is about 7700 Ws$^{1/2}$/m^{2}K (Oberbach 1980). After 1 second of heating, the first term thus becomes about 30 ^{o}C. The magnitude of the second term directly depends on the conductivity and thickness of the insulation material. For simplicity we have omitted the contribution of the electrically conducting layer to this term. If the thermal resistance (D/λ) of this layer is large, it should be added to the second term. In order to realize an extra 60 ^{o}C temperature rise, the thermal resistance of the insulation layer has to be about 3.10^{-4} m^{2}K/W. Since polyimide with λ=0.37 W/mK is used as an insulation material, its thickness has to be 0.1 mm at least.

An upper bound for the layer thickness is provided by the maximum cycle time increase. For short heating pulses, the cooling time relative to the situation without heater, is mainly determined by the delaying effect of the insulation layer, which can be approximated by (see eq.2.21)

$$\frac{t_{c,L}}{t_{c,0}} \cong \left(1 + \frac{1}{\mathrm{Bi}}\right)^2, \qquad \mathrm{Bi} \cong \frac{D_1/\lambda_1}{D_3/\lambda_3} \qquad (5.2)$$

Here Bi denotes the ratio of the thermal resistance inside the polymer melt to the thermal resistance outside. If we want the cooling time not to increase with more than, say, 20%, Bi has to be larger than 10. Further, since D_1 and λ_1 are 1 mm and 0.2 W/mK typically, the insulation layer thickness should not exceed the 0.2 mm. Note that if the heat production were taken into account, a smaller maximum thickness would be predicted. We therefore choose the layer thickness to be near the lower limit of 0.1 mm. This kind of argumentation of course does not result in the most optimal design. It merely provides some insight in which are the most important properties and which not.

The thickness of the heat producing layer (a carbon filled resin "LR-6007" from AKZO/Lion) depends on the desired resistance, which is most conveniently chosen to be near 15Ω (both voltage and amperage should not be too large). The specific resistance of the conducting material was measured to be 190 μΩm and the heater surface is 76x31 mm^2, thus suggesting a layer thickness of about 30 μm.

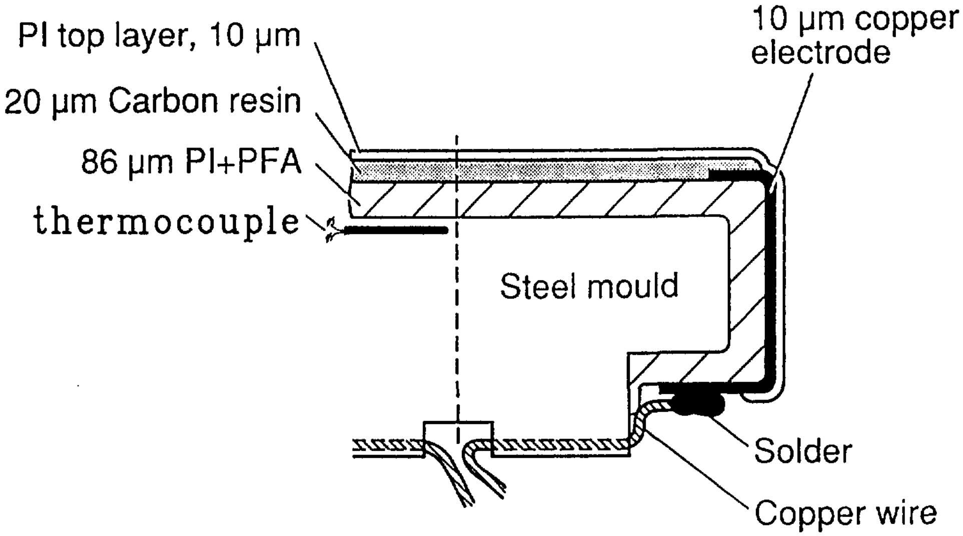

fig.5.1: Schematic view of fast-response heating element. The junction of the chromel-alumel thermocouple is situated 0.13 mm beneath the steel surface.

Following these guidelines several heater cells, according to the principle depicted in fig.5.1, were constructed. First, polyimide foils were attached to the steel mould with PFA glue (a fluoridated polymer). Then thin copper electrode foils were glued to the side surfaces and the conducting resin was painted on top of the polyimide layer. After drying and curing the resin was polished to the desired thickness. The thin polyimide top layer (Pyre ML resin) covers both the upper and the side surfaces in order to ensure electrical insulation. Thermal properties of the different layers are summarized in table 5.1.

5.2 Verification of heating curves (comparison with predictions)

In this section temperature measurements during and after certain, well defined, heating pulses will be shown. The experiments are simple. A heating element as in fig.5.1 is heated with constant power density, during a fixed

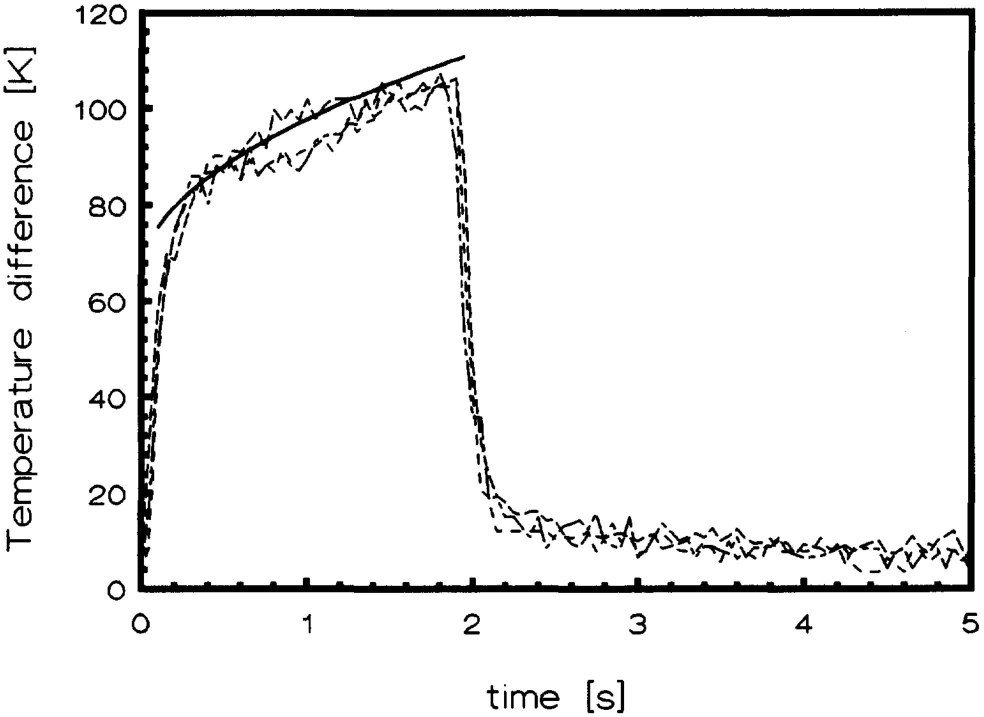

fig.5.2: Surface temperature rise as measured with IR pyrometer (ε=0.83). Dashed lines represent three experiments with a power density of 22.4 W/cm^2 during 1.9 s. Solid line represents the surface temperature according to eq.(5.1) with b_1=0 and λ_3=0.30. All other parameters are listed in table 5.1.

period of time. The temperatures at the upper surface and in the steel mould were recorded during and after this heating pulse.

Material	λ W/mK	ρ kg/m^3	c_p J/kgK	thickness mm	remarks
steel (X6CrNi 18-10)	15	7900	500	36.0	suppliers data
polyimide	0.37	1410	1340	0.087	Vespel®, own data
PI/PFA (4:3)	0.30	-	-	0.087	averaged
conducting layer	1.41	1520	1510	0.025	own measurements

table 5.1: Thermal properties and sizes of layers used in heater cells

Fig.5.2 shows the surface temperature rise due to a heating pulse of 22.4 W/cm^2 during 1.9 seconds. The experiment was repeated three times. The temperatures were measured with an IR pyrometer (Heimann, type KT4). Most of the temperature change occurs during the first few instants: about 70 ^oC temperature rise in 0.2 seconds. A similar behaviour is observed at the end of the heating pulse. Half a second after the end of heating, the surface temperature is back to only 12 ^oC above its initial value. These fast temperature changes are mainly due to the low heat capacity of the insulation layer and the heat producing layer, whereas the ratio D_3/λ_3 is responsible for the magnitude of the initial temperature jump (compare with eq.5.1). Comparison with earlier reported work clearly shows that our heating elements exhibit a 5 to 10 times faster temperature response for both heating (table 1.1) and cooling. This is of practical importance since now, for the first time, it becomes possible to realize a temperature jump of about 100 ^oC during the injection stage without any significant increase in cycle time.

Due to local thickness fluctuations, there is a variation of about 30% in the local power density, P_A. Pictures supplied by an IR thermovision system (photo 5.1) show that there are several hot spots present. These spots are about 30 to 50 ^oC warmer than their immediate surroundings. A better polishing procedure should settle this. The maximum possible power density, of course, is very much dependent on the presence of hot spots at the heater surface. In our laboratory a power density of 30 W/cm^2 was realized during several seconds.

In practical situations, surface temperature measurement is often not possible and measurement of the mould temperature seems to be the only

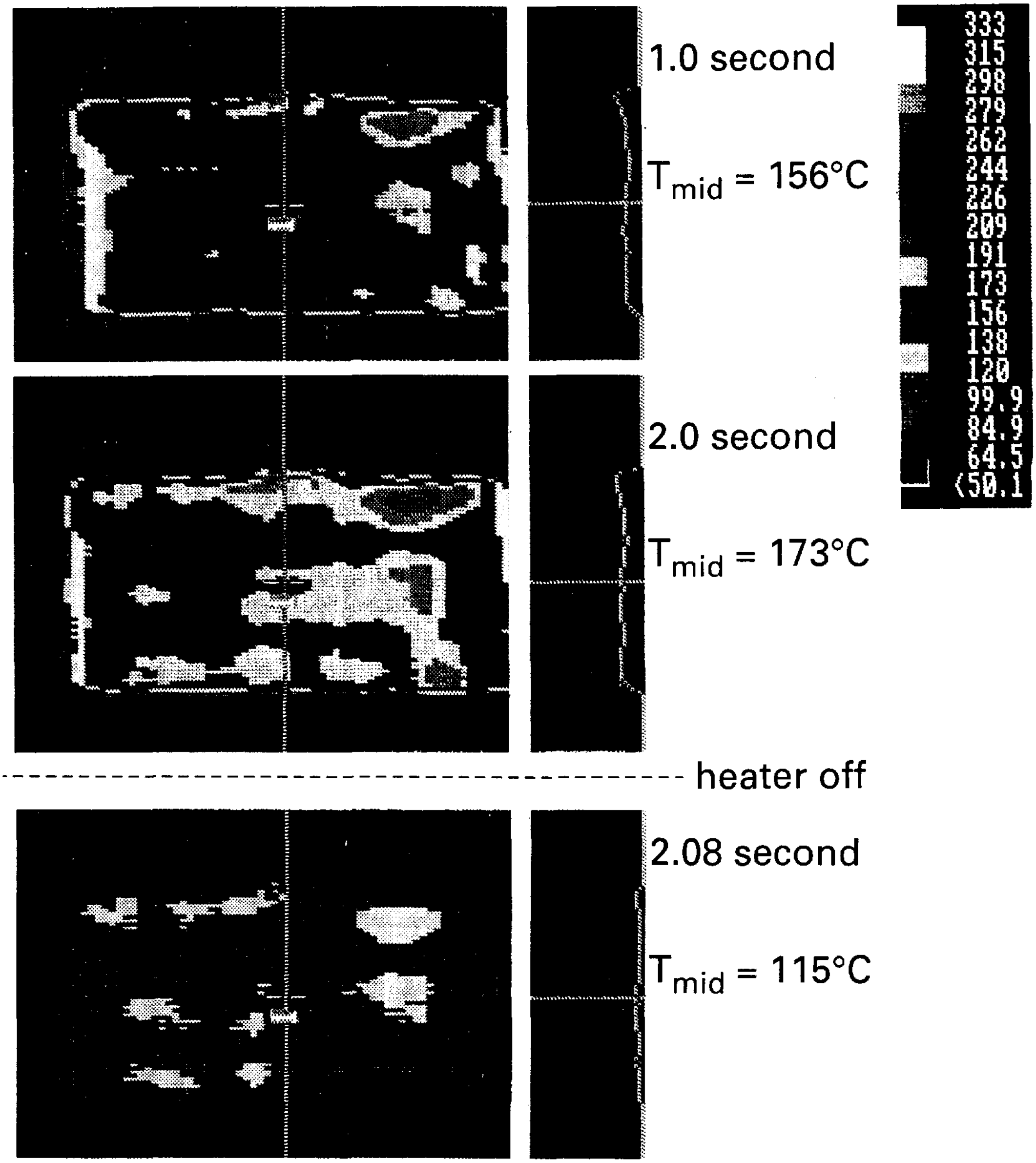
1.0 second
T_{mid} = 156°C
2.0 second
T_{mid} = 173°C
heater off
2.08 second
T_{mid} = 115°C
333
315
298
279
262
244
226
209
191
173
156
138
120
99.9
84.9
64.5
(50.1

photo 5.1: Example of the surface temperature of a heating element after 1.0 and 2.0 seconds of heating with 22 W/cm^2. The picture below was taken 0.08 seconds after the heater was switched off.

alternative. We therefore inserted a thin, 0.25 mm diameter thermocouple in the mould wall, parallel to the steel surface (see fig.5.1). The junction of the thermocouple was 0.13 mm below the surface, resulting in errors of 1 to 2°C typically.

The relation between the surface temperature and the temperature at the mould-insulation layer interface can be deduced from eqs.(2.25a) and (2.28a)

$$T_1(0,t) \cong T_4(0,t) + P_A \frac{D_3}{\lambda_3} \tag{5.3}$$

Measurements of the mould temperature during and after heating pulses of 2.0 seconds are shown in fig.5.3. The temperature rise is much lower than that at the heater surface (compare with fig.5.2), which is due to the thermal resistance of the insulation layer in between. The different curves correspond to three different power densities used and all fall onto one single curve if normalized to the same power density. It further shows a delay of about 0.3 seconds between the end of the heating pulse and the start of the cooling stage. The surface temperature as predicted from the mould

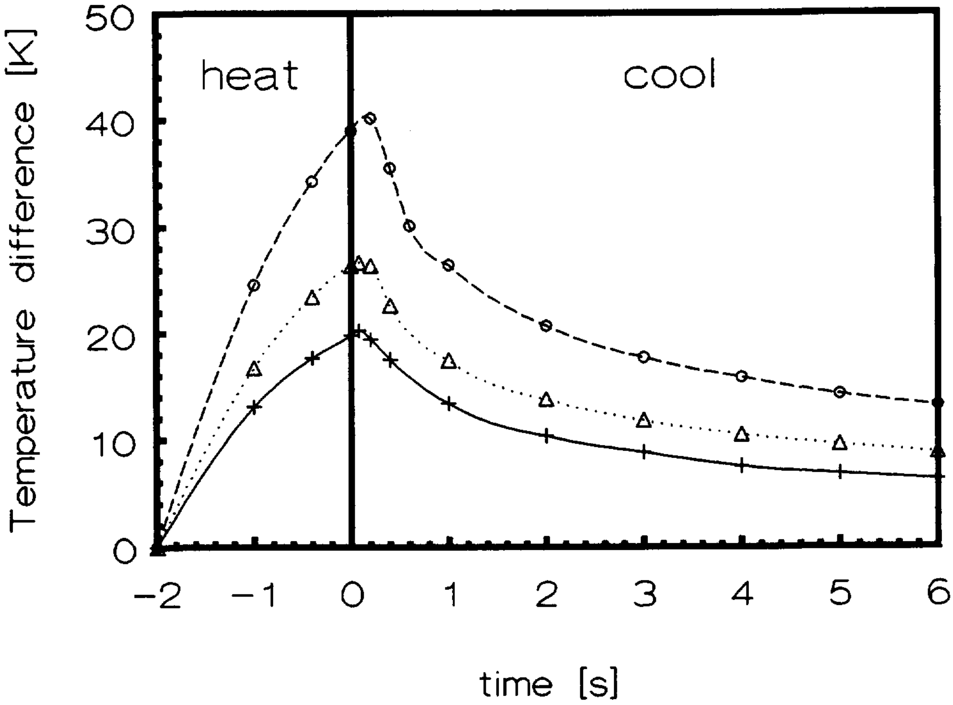

fig.5.3: Mould temperature during and after a heating periods Of 2.0 seconds for various heating strengths. -+-: 300 Watt, -Δ-: 400 Watt, -o-: 600 Watt. The surface area was 25.5 cm².

temperature and eq.(5.3), corresponds well with the measured surface temperature as indicated in fig.5.2.

5.3 Injection moulding experiments[2]

5.3.1 Material data and characterization

The injection moulding experiments were carried out with two types of polystyrene supplied by the Dow Chemical company, being respectively PS 638 and PS 678E. As can be seen from fig.5.4 and table 5.2, PS 638 exhibits a lower molecular weight while in both cases the ratio $\bar{M}_w/\bar{M}_n$ was 3.0.

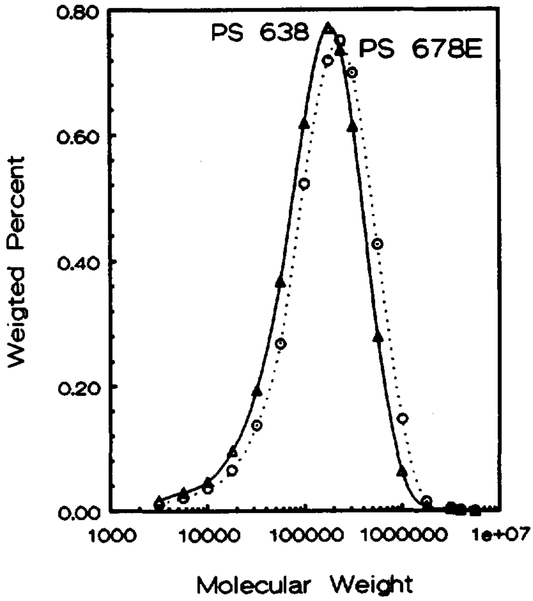

fig.5.4: Molecular weight distribution of PS 638 and PS 678E

Material	$\bar{M}_n$	$\bar{M}_w$	$\bar{M}_z$	Literature
PS 638	72	220	54	
PS 678E	87 ± 4	250 ± 20	49 ± 6	
PS 678E	90	240	53	Wales
PS 678E	85 ± 2	255 ± 2		Flaman

table 5.2: Molecular weights of PS 638 and PS 678E (in 1000)

---

[2] reprinted from KMB Jansen and AAM Flaman, Nat.Lab Technical note 175/92

The molecular weight distributions were determined with a linear μ-Styragel HT column at 35 ^{o}C and THF as a solvent. After the injection moulding experiments the $\overline{M}_n$ was found to decrease about 6% while $\overline{M}_w$ and $\overline{M}_z$ virtually remained unchanged.

The viscosity of PS 638 at lower shear rates was determined from oscillatory measurements with a Rheometrics cone-and-plate rheometer. For higher shear rates a Rosand capillary viscometer was used. Bagley and Rabinowitz corrections were applied to obtain true shear rate and viscosity values. As is shown in fig.5.5, there exists a good overlap of the cone and plate measurements at low frequencies and the capillary measurements at higher frequencies.

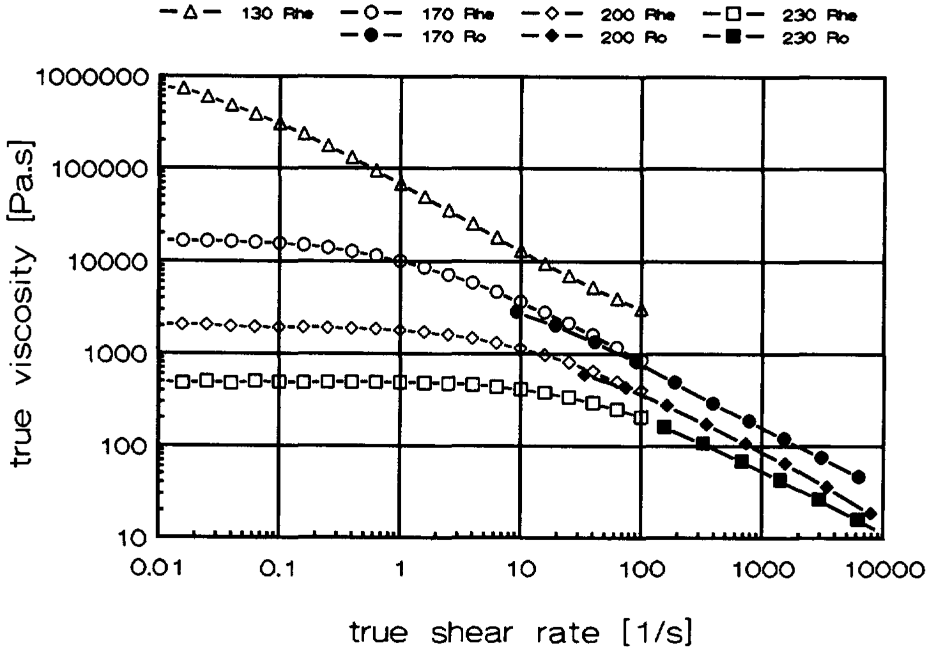

fig.5.5: viscosity curves of PS 638 as determined with cone and plate rheometer (open symbols) and capillary rheometer (filled symbols)

In fig.5.6 and 5.7 we plotted the master curves of μ^*, G' and G", obtained from oscillatory measurements at different temperatures. Here μ^*, G' and G" denote the complex viscosity, shear modulus and loss modulus, respectively (e.g. Bird et al. 1987). In the high shear rate region which is typical for the injection moulding process ($10^2<\dot{\gamma}<10^4$ s^{-1}), the master curves at 220 ^{o}C are conveniently approximated with the power-law model:

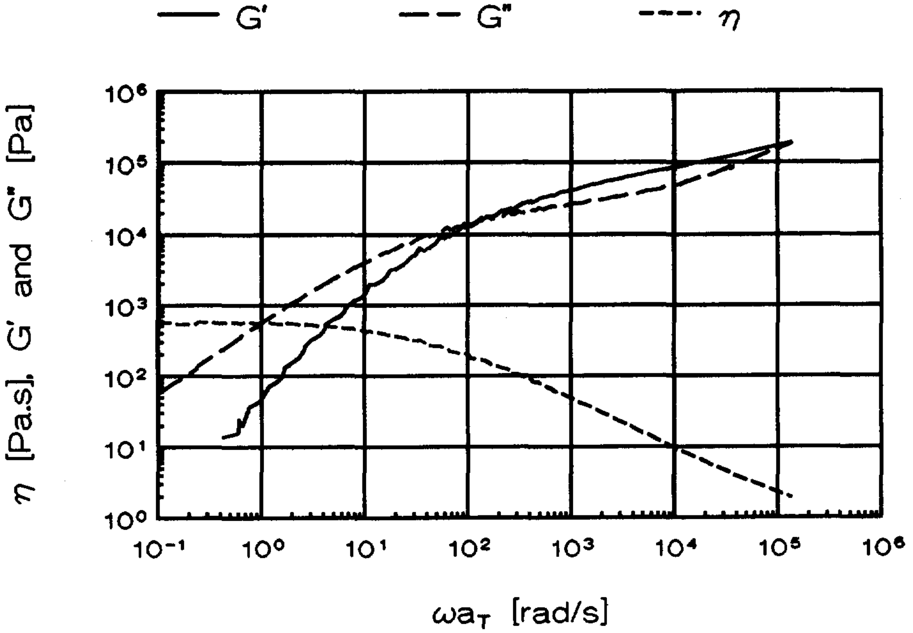

fig.5.6: Storage modulus, G', loss modulus, G", and viscosity, μ , versus ωa_T at 220°C for PS 638

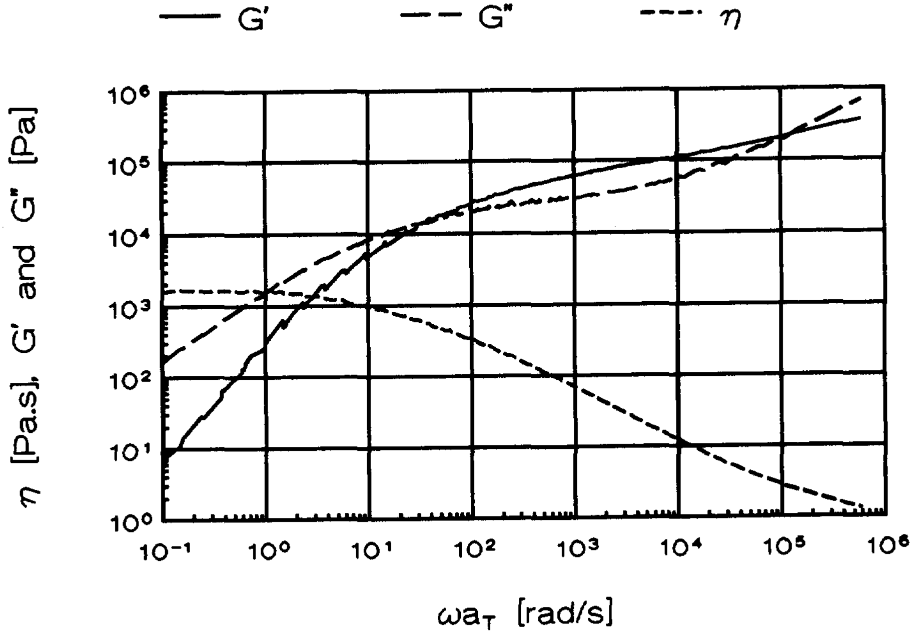

fig.5.7: As fig.5.6, but for PS 678E

$$\mu(\dot{\gamma},220^{o}C) = \mu_0 \cdot \dot{\gamma}^{\nu-1}, \qquad \dot{\gamma} = \frac{\partial v_z}{\partial x} \tag{5.4}$$

For PS 638 and PS 678E the parameters μ_0 and ν are, respectively, 4860 [Pa.s$^\nu$], 0.333 and 7970 [Pa.s$^\nu$], 0.31.

At low frequencies log G' and log G" approach a slope of 1 resp. 2. The frequency at which first deviation from these slopes occurs, is connected to the largest relaxation time, τ_o (Meistner 1989). At 220 °C the characteristic relaxation time is about 0.3±0.1 s. for PS 638 and 0.6±0.1 s. for PS 678E. Such relaxation times were used for the semi-quantitative calculations in section 4.2.

The temperature dependency of the viscosity (and other rheological properties) can be described with the temperature shift factor, a_T. Although the differences in molecular weight result in different rheological behaviour (figs.5.6 and 5.7), the difference in the shift factor is remarkably small (fig.5.8).

The thermal properties of polystyrene are λ=0.17 W/mK, ρ=1050 [kg/m^3] and

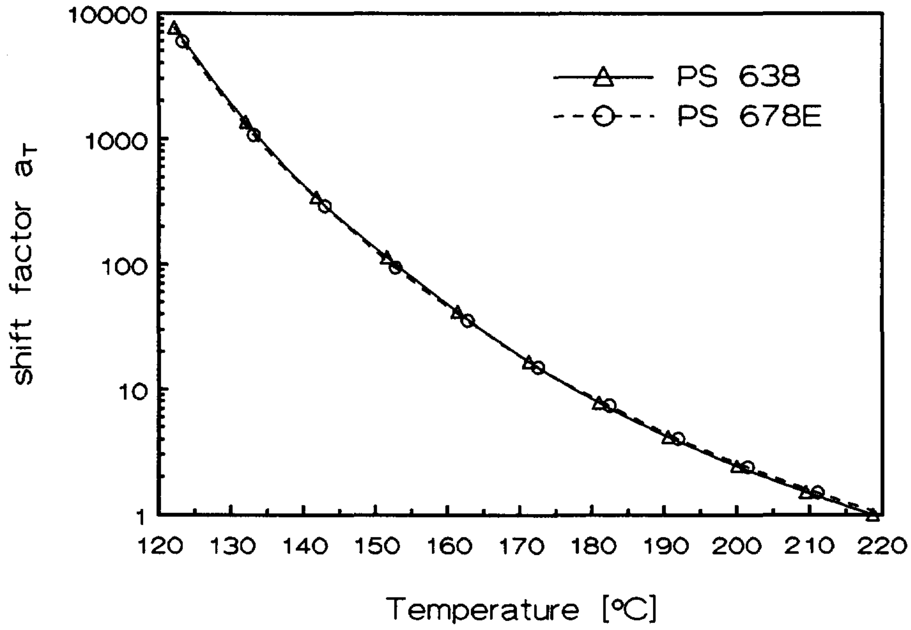

fig.5.8: Temperature dependence of the shift factor a_T with reference temperature of 220°C. (C_1 and C_2 are 3.22 resp. 179.11 for PS 678)

c_p=1300 [J/kgK] (see e.g. table 2.1, Oberbach 1980 and VDMA 1986). These properties are all taken at room temperature. No differences between the two grades are to be expected and the effect of the temperature is considered as secondary.

5.3.2 Injection moulding machine and mould geometry

The experiments were performed on a 35-ton Arburg machine with a PMC 1000 control system. The mould basically comprises a rectangular cavity of 80x35x2 mm^3 and a triangular entrance region as is indicated in fig.5.9. Four Kistler pressure transducers, located at different positions (indicated by P_1, P_2, P_3 and P_4 in fig.5.9), registered the cavity pressures during the moulding experiments without heating elements. During the other experiments only the pressures at P_1 and P_2 could be measured. The pressure in front of the screw tip, indicated by P_p, is calculated from the hydraulic pressure. The screw displacement is registered and converted afterwards to the screw velocity. The transition from injection to holding stage was always initiated by the signal from pressure transducer P_2.

During the passive layer experiments mould blocks were used which were equipped with a 0.25 mm diameter chromel-alumel thermocouple, located directly under the surface (see fig.5.1). The tip of the thermocouple is situated 20 mm from the entrance region and about 0.13 mm under the surface (fig.5.10).

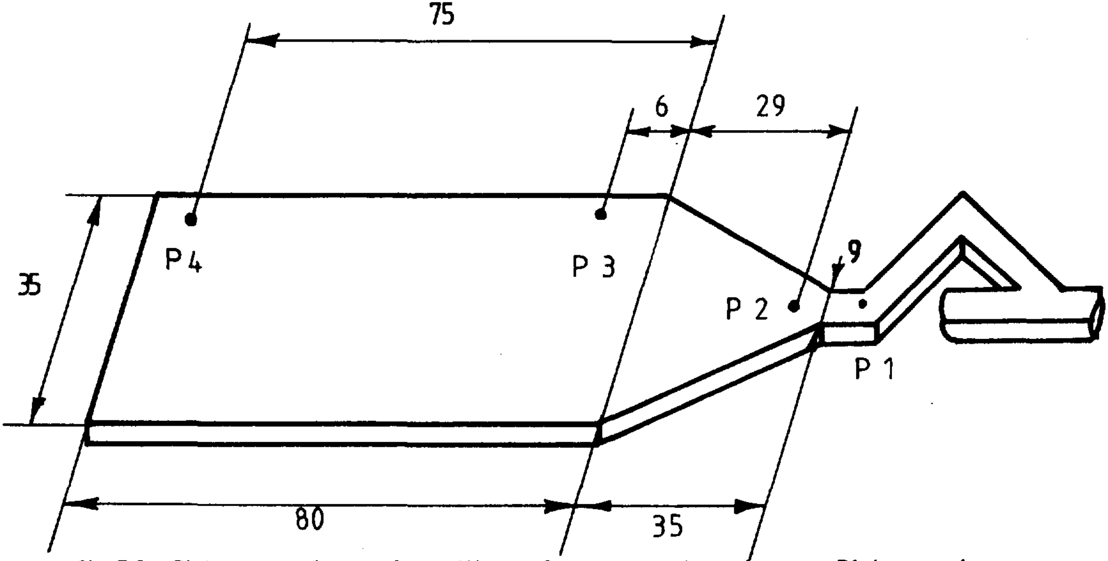

fig.5.9: Strip geometry and position of pressure transducers. Distances in mm. Thickness is 2 mm.

A 150 V, 7.5 A DC power supply was connected to each of the heating elements. A pulse generator which was triggered by the hydraulic pressure signal and a BBC Petersem (type B25-40-00) power relay were used to create a well defined electrical pulse.

The voltage and current of both heaters as well as the pressures, screw position and wall temperatures were recorded by a data acquisition system.

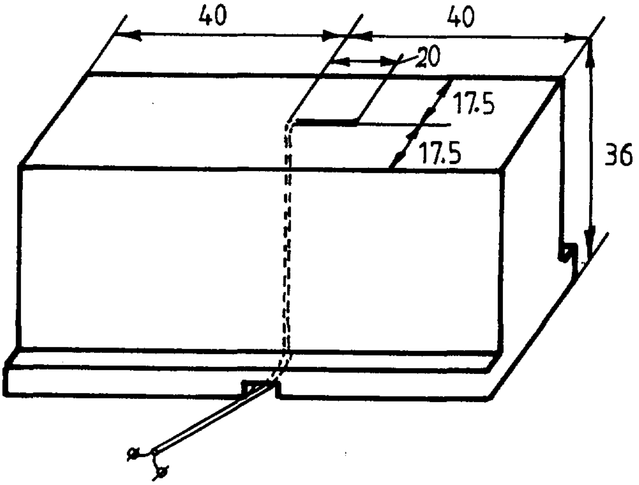

fig.5.10: Steel insert block with thermocouple

5.3.3 Processing conditions

By means of the injection moulding machine and the moulds described in the previous section several types of experiments were performed to investigate the influence of the injection moulding and heater conditions on the product properties. These experiments can be grouped in three categories:

1 Standard experiments where the influence of the temperatures and molecular weight was investigated;

2 Experiments involving passive insulation layers at the mould surface and

3 Experiments with an active heating element.

We chose the moulding conditions as used by Flaman (1990, Chapter 5.2) as a standard set of conditions (see also table 5.3).

T_{in}	injection temperature	220	^{o}C
T_w	mould temperature	50	^{o}C
$\dot{V}$	injection flow rate	7.62	cm^3/s
P_p	melt packing pressure	700	bar
t_{hold}	holding time	15	s
t_c	cooling time	30	s

table 5.3: processing conditions of standard experiment (A220)

Wall temperature, flow rate. packing pressure, holding and cooling time are kept constant in all experiments. The passive layer experiments (heater present but not used) are identified with code B whereas the standard experiments are coded as experiments A. In experiments C through G the heating conditions are varied systematically (see table 5.4).

experiment	**bare mould** (standard)	**cold heater** (passive)	**heater on**				
			lower power	standard heating	longer time	during filling	during holding
code	A	B	C	D	E	F	G
t_h [s]	-	-	1.95	1.95	4.25	1.85	2.15
t_d [s]	-	-	-0.05	-0.10	-0.05	-1.70	4.70
P_A (fixed mould)	-	-	11.5	22.2	22.3	22.3	21.6
P_A (moving mould)			10.0	20.5	20.9	20.9	17.1

table 5.4: schematic representation of the injection moulding experiments

The delay time is defined as the time interval from the moment the cavity is completely filled onwards. This moment is easily recognized in the pressure diagrams since at this point a sharp increase in all pressures is encountered. An example of a pressure diagram with heating pulse is given in fig.5.11.

All experiments are performed with an injection temperature of 220, 200 and 185 ^{o}C, except experiment C which was only performed with T_{in}=220 ^{o}C. In this section, however, we will mainly confine ourselves to the experiments at 220 ^{o}C. If necessarily, the temperature is added to the code in order to distinguish between the different experiments (experiment A185 thus indicates the experiment with conditions as given by table 5.3 but with a mass temperature of 185 ^{o}C). The results of all experiments can be found in

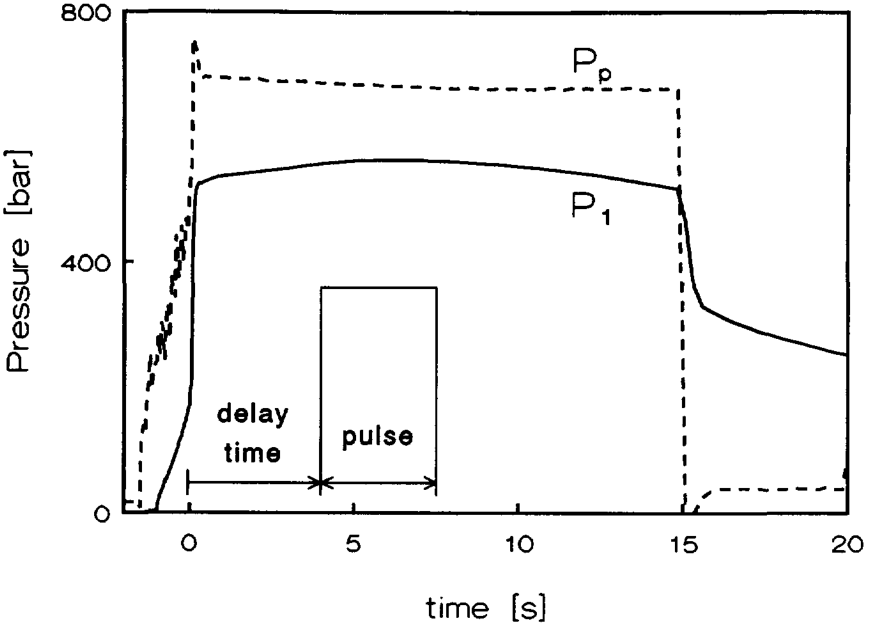

fig.5.11: Example of recorded pressure curves and heating pulse. P_p is the pressure in front of the screw tip, calculated from the hydraulic pressure.

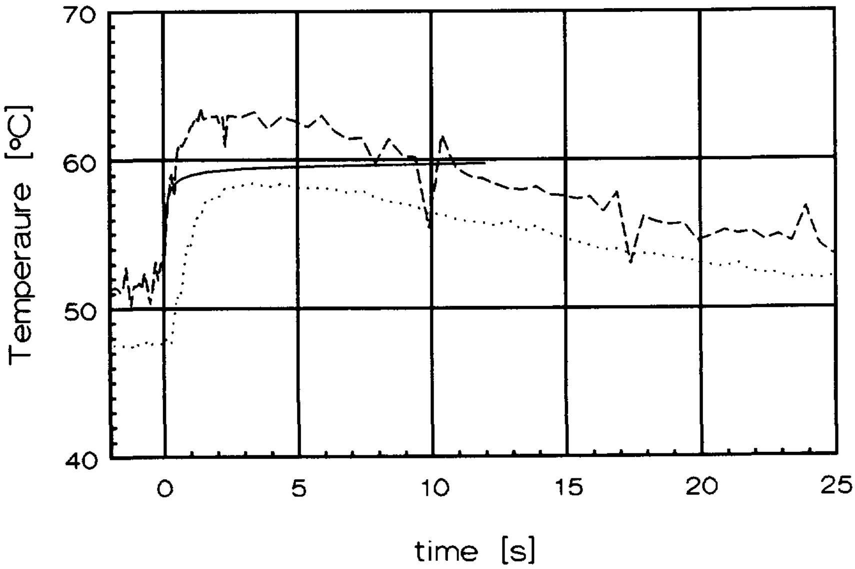

fig.5.12: Measured temperatures at mould-insulation layer interface of experiment B220. The dashed and dotted lines represent the two different thermocouple signals.

Jansen and Flaman (1992b). PS 638 is only used in experiments A and B and is coded with a double letter (e.g. BB200).

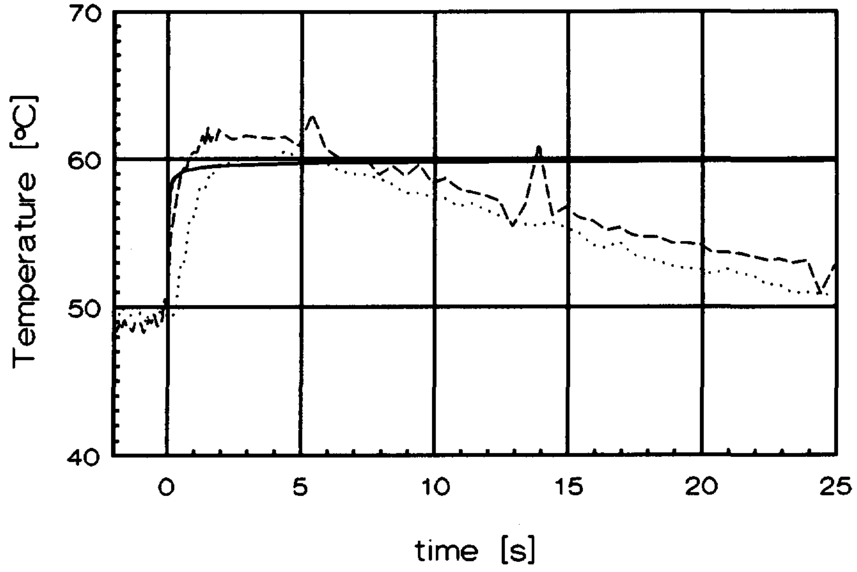

fig.5.13: As fig.5.12, but for experiment BB220 (with PS 638). The full line represents the calculated contact temperature 0.13 mm below the mould surface ("erf"-solution eq.(2.14)).

5.3.4 Moulding experiments with heater

The injection moulding experiments resulted in about 240 strips of series A and B and 80 specimens of the heater series (C through H). Several strips of each series were stored in a freezer at -18 °C to prevent stress and density relaxation. All other products were stored at room temperature. The products of the heater experiments all showed a typical and reproducible color pattern when examined between crossed polarizers (photo 5.2). This is due to the surface temperature variations (compare with photo 5.1). Note that looking through the product between crossed polarizers in fact shows the orientation *averaged* across the thickness, which is different from the much more detailed measurements described in the next section. The colors are a measure for the average orientation. It is important to note that the less pronounced the colors are, the more orientation is frozen-in. Thus in the specimen without a heating pulse, B220, the orientation steadily decreases from the gate area towards the end of the flow path. About 4 different orders of blue (4 wavelengths path difference) are observed in sample B220, whereas

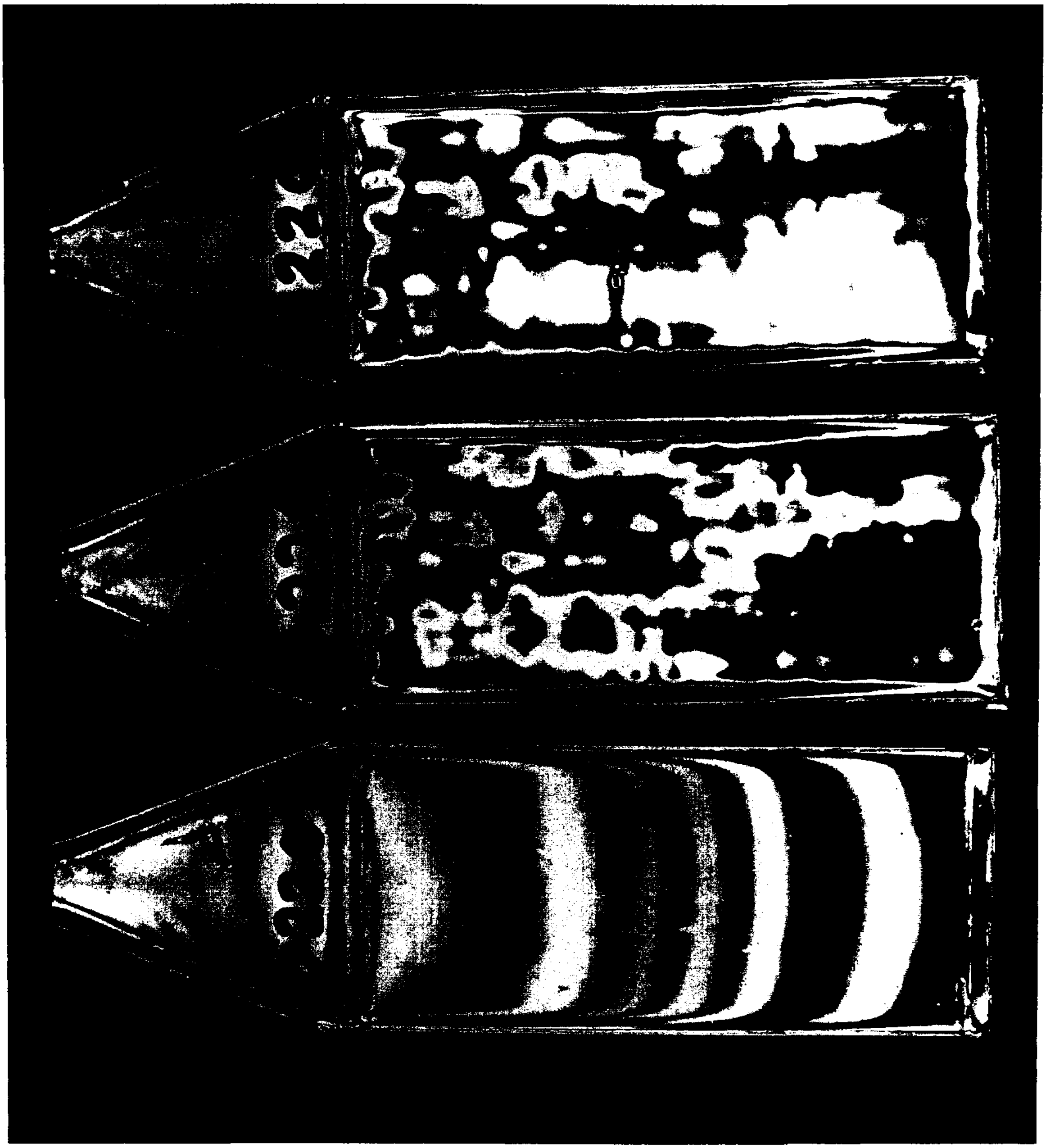

photo 5.2: specimen of series B220, D220 and E220 with heating times of 0, 2 and 4 seconds (20 W/cm^2), viewed between crossed polarizers.

sample D220 (2 seconds heating) shows only one or two different orders. This means that also the large amount of orientation near the gate seems to be sufficiently suppressed. In specimen E220 this effect is even stronger.

Pressure measurements

A typical cavity pressure profile was already given in fig.5.11. The initial pressure rise, during the filling process, shows an almost linear increase. Directly after the mould is filled completely, the pressure increases instantaneously. The maximum pressure in the holding stage can be maintained for some time, depending on the distance from the gate. Far from the gate (P_3 and P_4) the temperature is lowest, causing a high viscosity which restricts the additional melt flow in this region. Therefore, at P_3 and P_4 shrinkage prevails and the pressure rapidly decays. The pressure measured at P_1 (in the 5 mm thick gate) can be kept high during the holding stage because of the relatively large thickness. This pressure only drops if the holding pressure (or P_p) is removed. Note that the pressures at P_3 and P_4 are the most interesting ones since they are measured in the rectangular area of the cavity. All pressure curves depicted in this paragraph follow the same

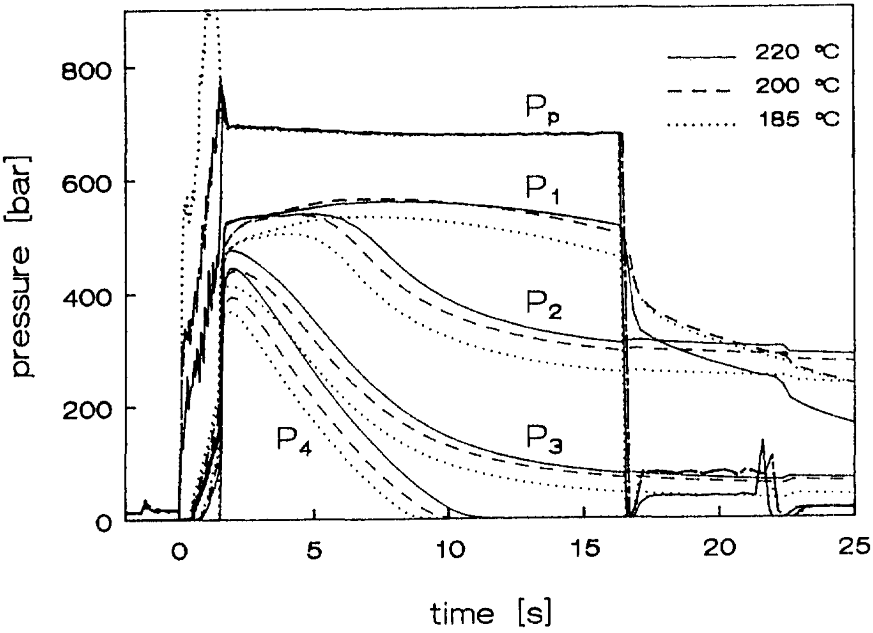

fig.5.14: Effect of melt temperature on pressure profiles at 220 °C. (series A220 and A200 and A185).

qualitative behaviour. In the following we will therefore discuss the *differences* between the pressure curves of different experiments, rather than the pressure histories themselves.

Fig.5.14 shows the dependence of the pressure profiles on the melt temperature. At all locations the lowest pressure corresponds to the lowest temperature. Further, the material with the highest viscosity (PS 678E), is less capable of maintaining a high pressure level at the end of the flow path as follows from fig.5.15.

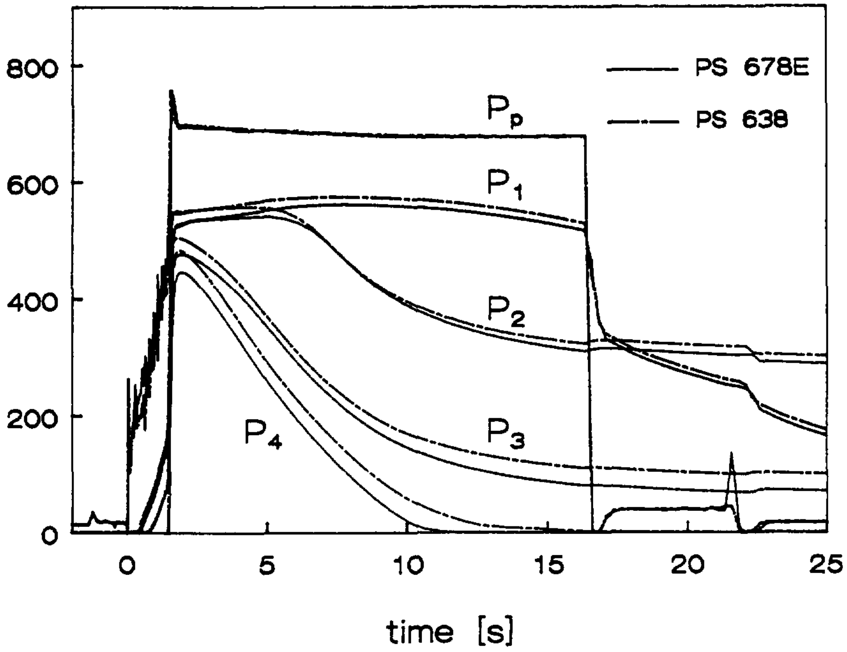

fig.5.15: Effect of molecular weight on pressure profiles at 220 °C. (series A220 and AA220).

The effect of a passive layer at the cavity surface is limited as can be seen in fig.5.16. The hydraulic pressure (here indicated by the pressure in front of the screw tip, P_p) is hardly lower and the effect on the pressure before and in the entrance region seems to depend on the melt temperature. The pressure of P_1 and P_2 in the first few seconds of the holding stage of experiment B220 is above that of the standard experiment without passive layer. However, at 200 and 185 °C (not shown here) the pressures of the experiments B are below those of the respective standard experiments.

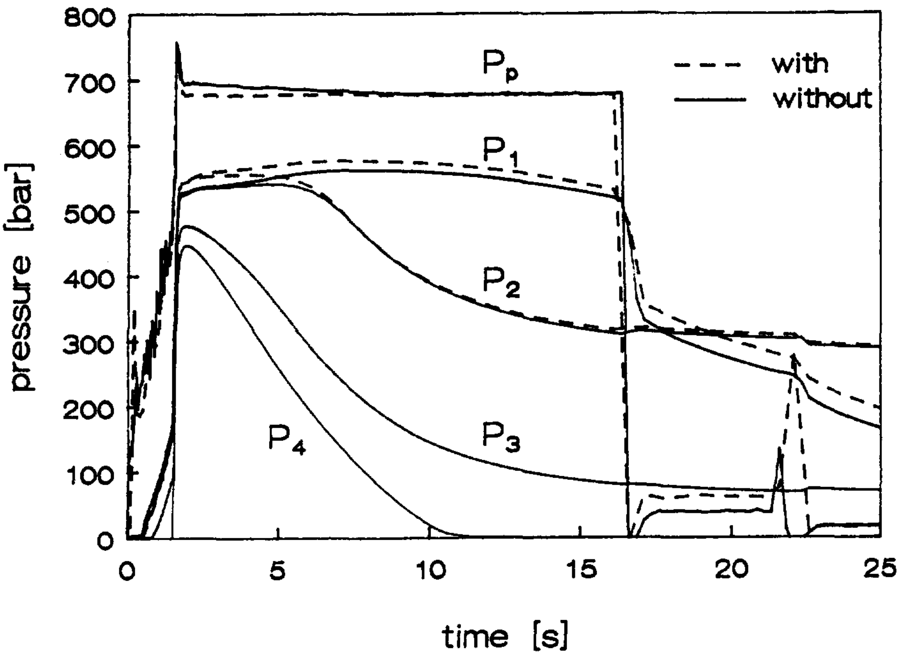

fig.5.16: Effect of a passive layer on pressure profiles at 220 °C. (series A220 and B220).

In the pressure curves of the heating experiments (fig.5.17, 5.18 and 5.19) also the power pulses are shown (in Watt/23 cm^2). For these pulses the same scale is used. Thus pulse E is about 500 Watt/23 cm^2 (= 22 W/cm^2). Differences in heating power of about 10% between the two cavity sides were observed. The interpretation of the cavity heating on the pressure curves is rather difficult since the cavity pressures could not be measured themselves (due to the presence of the heaters at the mould surface). Furthermore, during the heater experiments the pause time between two shots was increased to allow for visual inspection, resulting in lower mould and runner temperatures and a subsequent (small) increase of the pressure drop. This effect probably counteracts the effect of the heating elements some seconds after the end of the pulse. Further, if the heating pulse is applied before the gate freezes off, more material may enter the cavity causing a higher cavity pressure. It would have been interesting to check this hypothesis by comparing the different product weights. However, such a verification is complicated by the fact that the gap width of experiments B (without heating) differs slightly from that of the other experiments, which will affect the

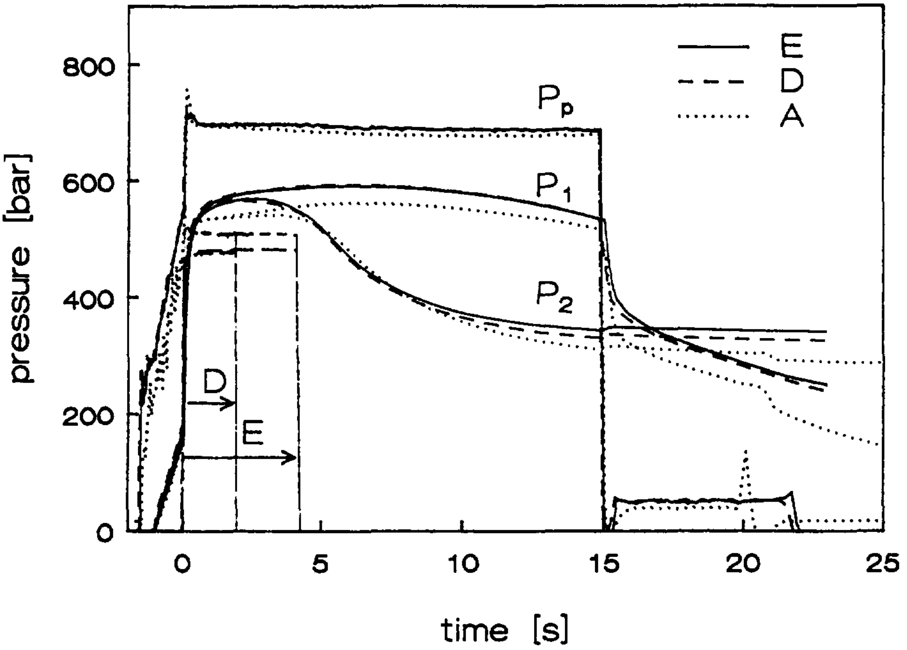

fig.5.17: Effect of heating time on pressure profiles at 220 °C. (series A, D and E). The square pulses denoted with D and E indicate the heating power in W.

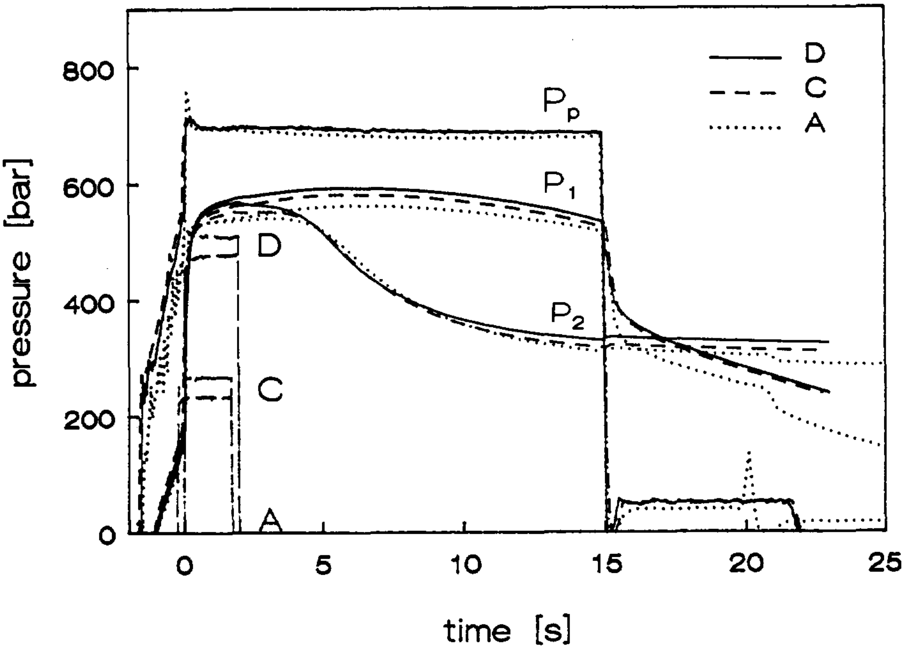

fig.5.18: Effect of heating power on pressure profiles at 220 °C. (series A, C and D).

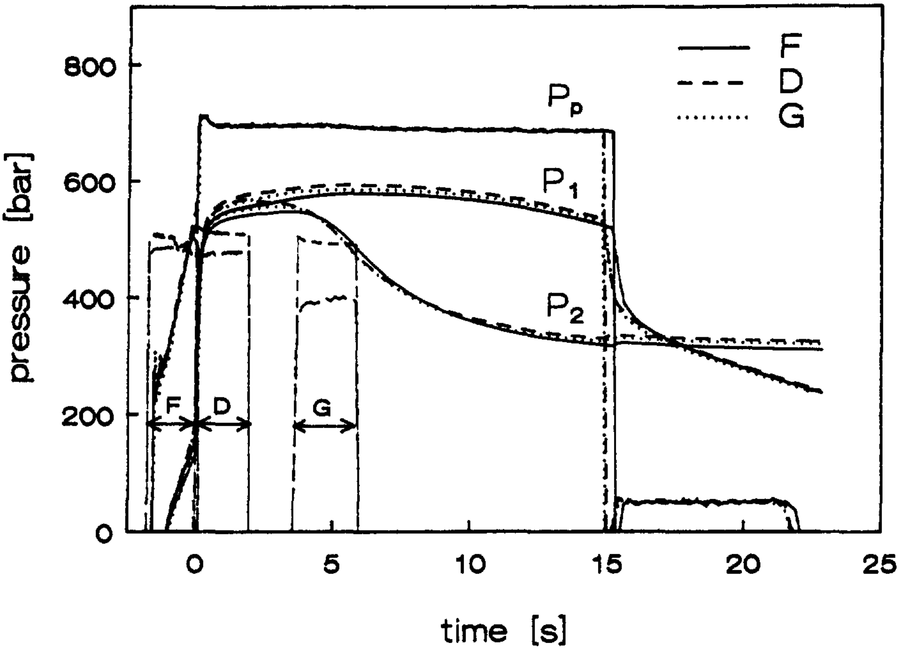

fig.5.19: Effect of delay time on pressure profiles at 220 °C. (series G, D and F).

product weight. The reason for the small differences in gap width is that after experiments B the mould inserts were removed and inspected.

The most important conclusion concerning the effect of the heating elements on the pressure history, is that the heaters have only a small effect on the filling pressures.

5.4 Orientation measurements

In this section we will discuss the measurements of the orientation distribution by means of the birefringence technique. First it is briefly explained what is understood by birefringence and under what circumstances it can be used for orientation measurements. In a second paragraph we will discuss the importance of the different (tensorial) birefringence components. Next, the measurement method itself will be elucidated, whereas in the last paragraphs the results of the measurements will be discussed.

5.4.1 Birefringence contributions

Birefringence is an optical effect, caused by the small difference in electrical polarizability of the material between the direction of the chain axis and a direction perpendicular to that axis (see e.g. Feynman (1989) vol.I §33.3, Struik (1990) p.297). In polymer materials, both orientation and (frozen-in) stresses contribute to the birefringence. Therefore, the total birefringence, Δn_{tot}, is given by

$$\Delta n_{tot} = \Delta n_{or} + \Delta n_{stress} \tag{5.5}$$

Here Δn_{or} and Δn_{stress} denote the orientation dependent part and the stress dependent part of the total birefringence, respectively. Each of these parts is proportional to the principal stress difference which caused that specific part of the birefringence (Wimberger-Friedl (1991) p.197):

$$\Delta n_{or} = C_m \Delta\sigma_{flow} \qquad (= \Delta n_{\infty}.f_H) \tag{5.6}$$
$$\Delta n_{stress} = C_g \Delta\sigma_{residual} \tag{5.7}$$

where C_m, C_g and $\Delta\sigma_{fl}$, $\Delta\sigma_{residual}$ represent the proportionality constants (stress optical constants) in melt and glassy state and the flow induced and residual stress components, respectively. Further, the Hermans orientation factor, f_H, expresses the amount of average chain orientation and Δn_{∞} denotes the birefringence at complete uniaxial orientation (f_H=1).

Which of the two parts dominates the total birefringence is fully material dependent. In PMMA, for example, the residual stress contribution is relatively high, which makes PMMA a suitable material for optical stress measurements. On the other hand, if the orientation contribution predominates, birefringence measurements can be used to measure the (frozen-in) orientation. For polystyrene (PS) the optical constants are (Wimberger-Friedl (1991) and Struik (1990)): C_m=-4800.10^{-12}[Pa^{-1}], C_g=10.10^{-12}[Pa^{-1}] and Δn_{∞}=-0.12. Thus, a typical residual stress of about 2 MPa will cause a $\Delta n_{stress} \cong 2.10^{-5}$, which is low compared to the total amount of birefringence in PS, $O(10^{-3})$. This, in fact, motivated us to perform our experiments with PS as a moulding material.

As was said before, the birefringence and stress contributions are tensorial quantities. The relative importance of these components will be discussed below.

5.4.2 The different components of the birefringence tensor

In the paragraph above we showed that for polystyrene the birefringence tensor is almost completely proportional to the frozen-in orientation. Here we will elucidate the relation between the complete state of orientation and the measurable (birefingence) quantities. This subject was treated in more detail in the recent paper of Wu and White (1991). The refractive index tensor possesses 9 non-zero components in an arbitrary coordinate system. This tensor can expressed in diagonal form with only three non-zero components by a suitable rotation of the coordinate axes. These new axes are referred to as the principal directions (I, II and III) and are connected to the old coordinate system by three rotation angles. The birefringence differences are defined as the difference in principal axis values:

$$\Delta n_{I,II}= n_I-n_{II}, \quad \Delta n_{II,III}= n_{II}-n_{III}, \quad \Delta n_{I,III}=\Delta n_{I,II}+\Delta n_{II,III} \tag{5.8}$$

Note that there are only two independent birefringence differences. The birefringence tensor (and the orientation tensor) is thus completely characterized by these two values and their rotation angles ($\mathcal{X}$). In our coordinate system we use the designation z, x and y for the flow direction, thickness direction and width direction, respectively. For a sample cut along the centre of the specimen as is indicated in *fig.5.20*, the *y* direction coincides with one of the principal axis, say the III-axis, because of symmetry. As a consequence, the other principal axes must lie in the xz-plane of the specimen. This can be verified independently by measurements in the xy-plane, which should yield $\mathcal{X}_{y,III}=0$ at y=0. As will be shown below (fig.5.22, 5.23), the birefringence difference in the xy-plane is much lower than that in the xz-plane.

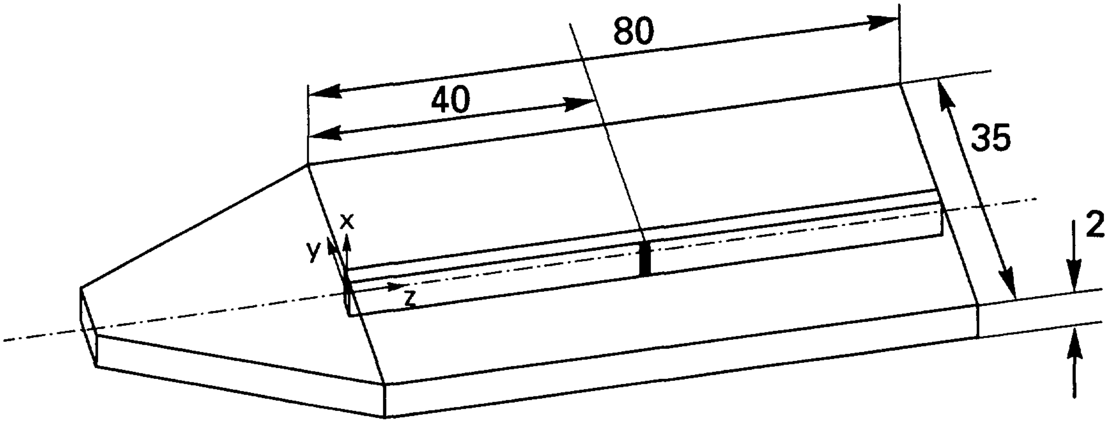

fig.5.20: Schematic illustration of slice removed from moulded part used for measurements of Δn in xz-plane (light beam in y direction). Distances in mm.

The birefringence in e.g. the xz-plane can be represented in vector form. As is shown in fig.5.21 such a representation is quite illustrative since it gives us a physical picture of how the molecules are oriented in an injection moulding sample. The molecules which are frozen-in at the product surface experienced a strong elongational force just before solidifying (fountain effect at flow front) and are oriented in the flow direction. The orientation direction of the molecules nearer to the core are all directed more or less towards the centre, which is typical for the shear flow of a (viscoelastic) fluid. In fact, the rotation angle is a measure of the melt elasticity (Wimberger-Friedl (1991)):

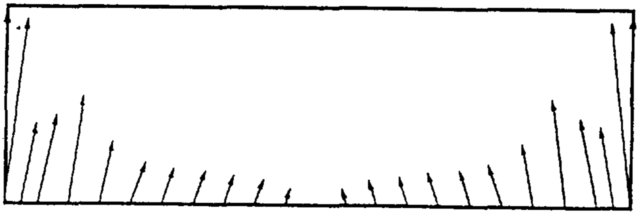

fig.5.21: Vector representation of birefringence in xz-plane (plane of shear)

$$\cot|2\chi_{z,I}| = \frac{\sigma_{xx}-\sigma_{zz}}{\sigma_{xz}} = \frac{N_1}{\sigma_{xz}} \tag{5.9}$$

Here N_1 denotes the first normal stress difference which is zero for Newtonian fluids. From eq.(5.9) it thus can be seen that this angle may vary between 45° for Newtonian (or purely viscous) fluids and somewhere near zero for very elastic fluids (large normal stresses with respect to shear stress).

Remark 1: since the rotation angle $\chi_{z,I}$ is defined as the angle between the flow direction and one specific principal direction, its sign reverses, going from left to right in fig.5.21. This is consistent with our experimental observations. The reader should note that the difference with the classical "extinction angle" is only a matter of definition. The extinction angle is the *smallest, positive* angle between the flow direction and one of the principal axes. It changes from principal axis instead of changing sign.

Remark 2: For practical reasons we chose to present all measured birefringence vectors as two separate plots, one for the magnitude and the other for the rotation angle.

The plot of the orientation magnitude in the plane of shear (e.g.

fig.5.22) is typical for injection moulded products. As was already explained in the introduction, the small surface maximum is ascribed to the well known fountain flow effect. Further down the surface it is followed by a broader maximum due to the shearing stress during flow. The position of this maximum is connected with the solidified layer thickness at the end of the filling stage.

5.4.3 Sample preparation and measurement technique

Slices of about 0.3 mm thickness were removed by a milling machine with a diamond cutter rotating at a speed of 3400 rpm at 80 mm from the centre. In this way an optically smooth surface was obtained without introducing extra orientation or causing stress relaxation.

The measurements were performed at room temperature on a Jenapol polarizing microscope with linearly polarized light. The light beam was in the y direction (see fig.5.20) and the sample was scanned in the x direction (thickness). Each measurement starts with finding the rotation angle. This was done by rotating the sample in the xz-plane, relative to the flow direction (edge of sample), until complete extinction is accomplished. This rotation angle is called $\mathcal{X}$. The direction of polarization is then parallel to the direction of the molecular orientation. Next, the sample was rotated 45° to the position of maximum transmission. The birefringence can then be measured by subtracting an equal amount of birefringence by means of an Ehringhaus E6 tilting compensator. The relation between the tilting angle ϕ of the compensator plate and the birefringence is given by (Ehringhaus 1938)

$$\Delta n = \frac{d_c}{d_s}\left(\sqrt{n_e^2-\sin^2\phi} - \frac{n_e}{n_o}\sqrt{n_o^2-\sin^2\phi}\right) \tag{5.10}$$

where n_e and n_o denote the extraordinary and ordinary refractive indices of the compensator plate at wavelength λ, d_c(=1mm) the compensator thickness and d_s the sample thickness. For the (quartz) compensator plate at hand n_e=1.555339 and n_o=1.546168 (at λ=546 nm).

The birefringence and rotation angle are measured with a typical error of $\pm 0.04\times10^{-3}$ and ±1°, respectively, while the error in the location of the measuring spot is estimated to be about 0.01 mm. The reproducibility was investigated by analyzing the birefringence distribution in the xz plane for two specimens produced several weeks apart, but under the same experimental conditions (series A220). As can be seen from fig.5.22, both location and magnitude of the measured birefringence and rotation angle show an excellent agreement.

5.4.4 Orientation perpendicular to flow direction

The orientation distribution in the xy plane (perpendicular to the flow direction) was measured at different axial and transverse positions. The birefringence distribution at z=40 mm and y=0, i.e. at the midpoint of the

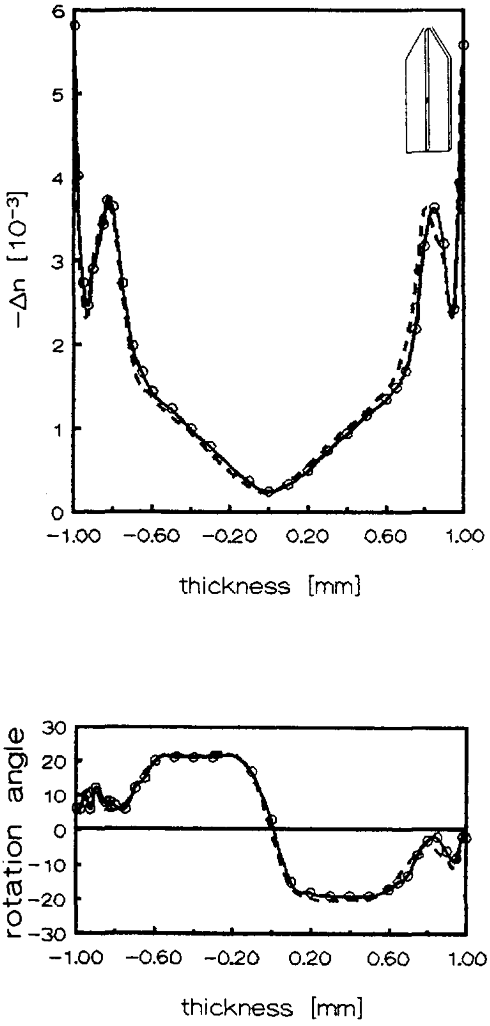

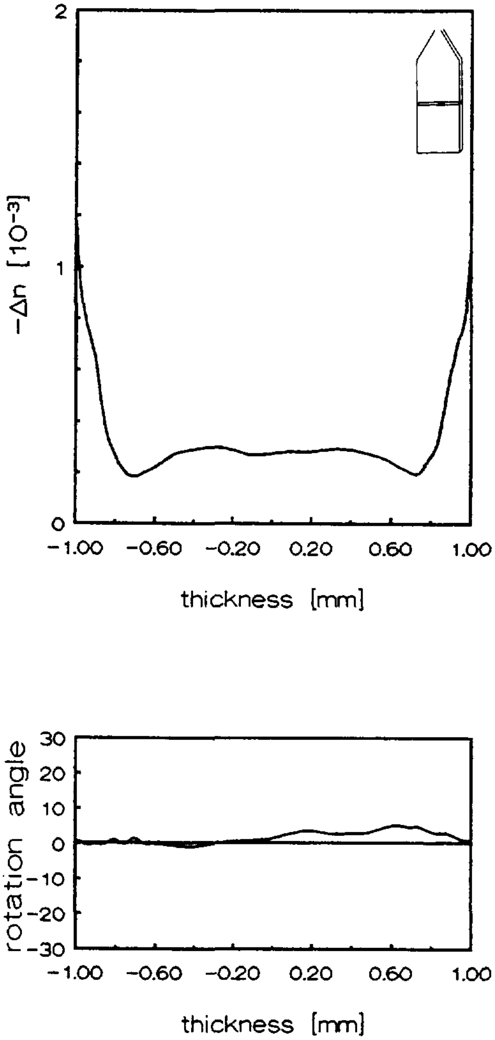

fig.5.22: Birefringence (above) and rotation angle (below) in xz-plane for two samples of A220 (y=0,z=40 mm) Dashed line is duplicate measurement.

fig.5.23: As fig.5.22, but now in xy-plane (y=0, z=40 mm)

rectangular section, is shown in fig.5.23. A comparison with fig.5.22 shows the surface maximum to be about 5 times lower in transverse direction, whereas the orientation level in the central part is equal in both cases. The orientation angle of the transverse component is almost zero, which was expected because of symmetry reasons.

The transverse birefringence distributions at z=40, y=12.5 mm (5mm from

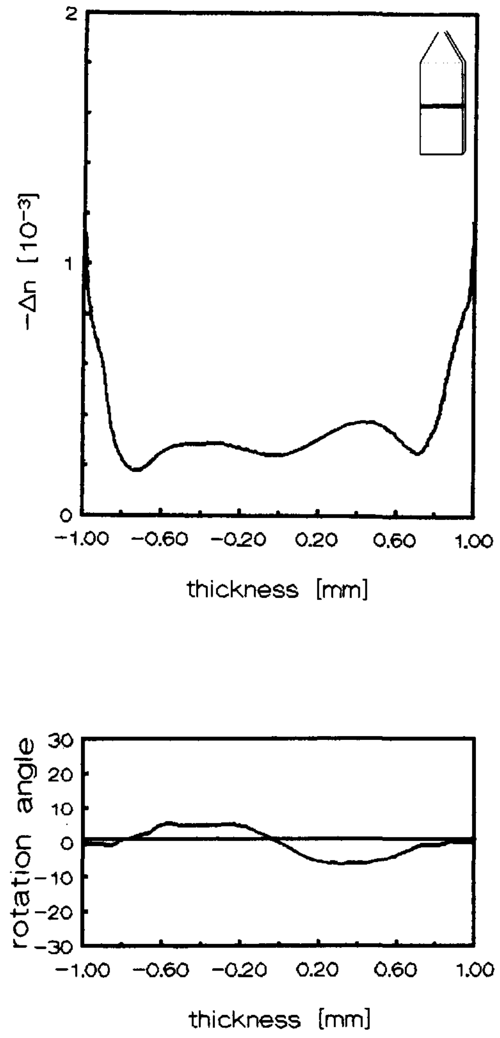

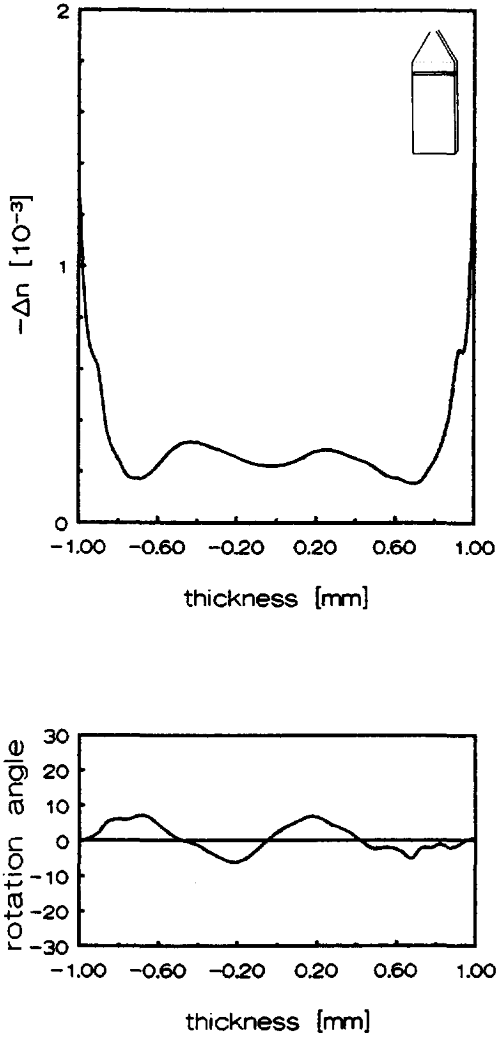

fig.5.24: As fig.5.23 but at z=40 mm and y=5 mm from the edge

fig.5.25: As fig.5.23 but at z=10 mm and y=2 mm from the edge the edge) and the distribution at z=10, y=15.5 mm (2 mm from edge, see fig.5.24 and 5.25) hardly deviate from the distribution as given in fig.5.23. This birefringence is associated with the residual stress component and thus corresponds well with the idea of an equibiaxial stress distribution as discussed in sections 4.4 and 5.5. This idea is further supported by the fact that the level of birefringence at x=0 in the xz-plane and the xy plane are identical (compare figs.5.22, 5.23 and 5.27). Note that at x=0 no shear

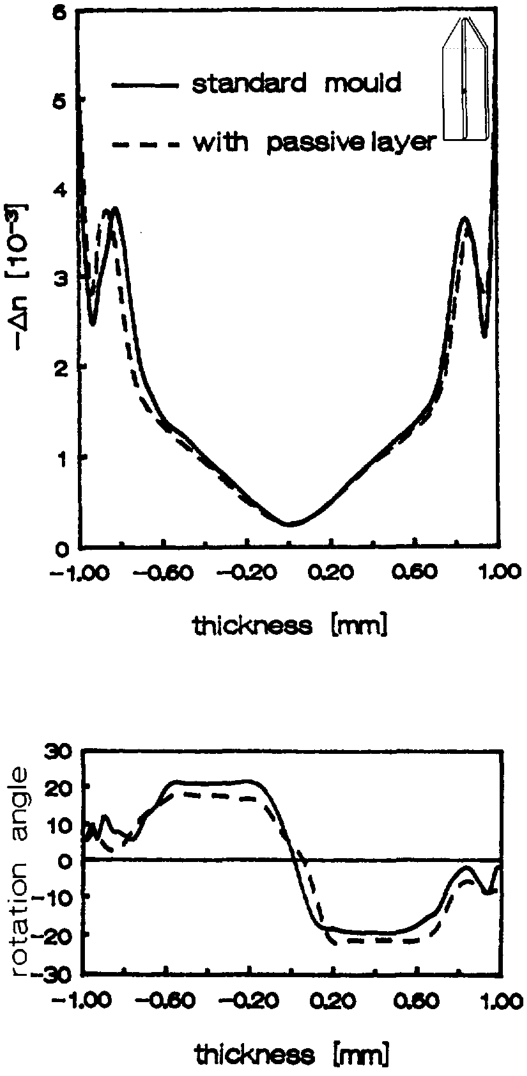

fig.5.26: Effect of passive layer on birefringence distribution at 220 °C. (series A220 and B220). The rotation angle is shown below.

forces could be present and thus no orientation contribution is to be expected. The deviations from zero of the rotation angles in figs.5.24 and 5.25, however, were not expected and are probably a combined effect of a small transverse flow during packing and an asymmetric cooling behaviour present near the edges of the strip.

The effect of the *orientation* on the birefringence in the xy-plane is thus small and the birefringence distribution in the xz-plane will be taken as being representative for the overall orientation level.

5.4.5 Orientation distribution with passive layer

The presence of a thermal insulating layer at the mould surface raises the contact temperature between polymer and cavity and thus allows for faster orientation relaxation. This process is largely dependent on the polymer used. Wimberger-Friedl (1991) reported an experiment with a low molecular weight polycarbonate (having short relaxation times). The orientation peak at the product surface disappeared completely after the mould surface was covered with a 0.2 mm thick teflon sheet. In contrast, our experiments B with polystyrene PS 678E (longest relaxation time at 220 °C about 0.6 s.) show hardly any effect of the insulation layer (0.1 mm PI) on the birefringence distribution. Only a small shift towards the product surface (due to a somewhat slower cooling process) can be observed (fig.5.26). Likewise, the rotation angle was not much affected by the insulation layer.

5.4.6 Orientation distribution with active heater[3]

In contrast with the experiments reported above, a short period of mould heating turned out to be an effective means of reducing the orientation level in injection moulded polystyrene products. The effect is most clearly illustrated by comparing the standard situation (A_{220}) with a heating experiment (D_{220}), at different positions along the flow length (fig.5.27 and 5.28). As appears from these figures, the surface orientation remains more or less unchanged by the heating pulse, while the shear orientation decreases with a factor 2 or 3. After the heating pulse, the orientation relaxation is not symmetrical anymore, nor does the orientation decrease monotonically along the flow path. This is probably caused by the (small) non-uniformities in heating power (see table 5.4).Surprisingly enough also the orientation near the core region is strongly reduced. An almost constant and very low birefringence level in the region from -0.6 to 0.6 mm was observed.

---

[3] KMB Jansen, AAM Flaman, accepted for publication in Polym. Eng. Sci.

The effects of the heating pulse on the orientation angle is shown at the lower part of fig.5.28. As can be seen, the angle first increases, reaches a maximum near z=20 mm and then quickly decreases to turn negative from about 50 mm onwards. This behaviour is quite strange, especially if compared with

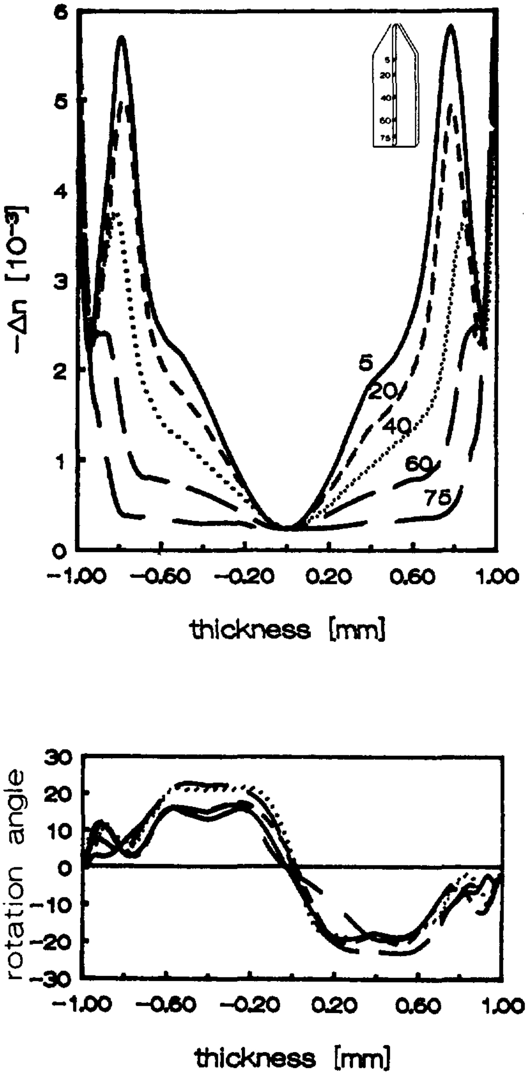

fig.5.27: Effect of flow path on orientation distribution of A220. The numbers represent the distance from the start of the rectangular section.

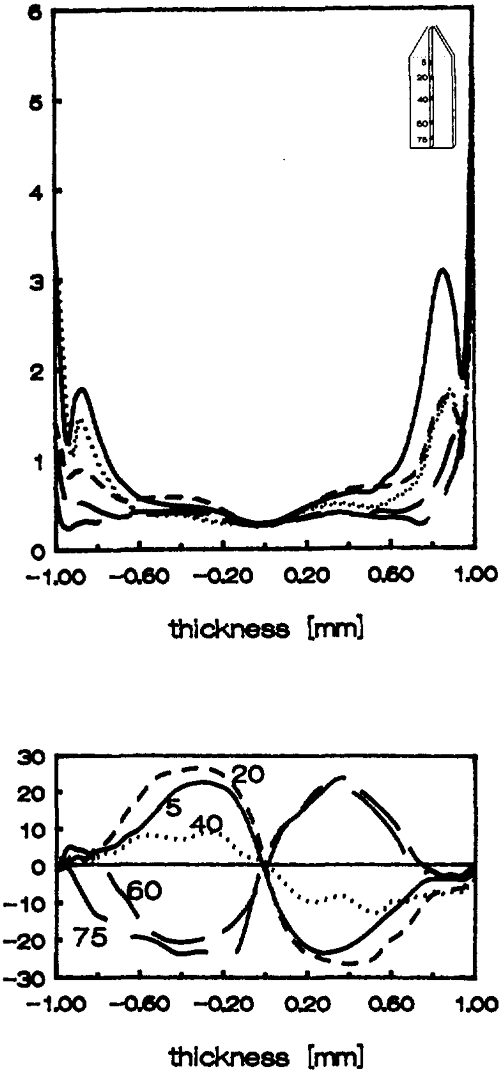

fig.5.28: As fig.5.27 but now for series D220.

the more or less constant angle distributions of the standard experiment (fig.5.27). No explanation is available yet.

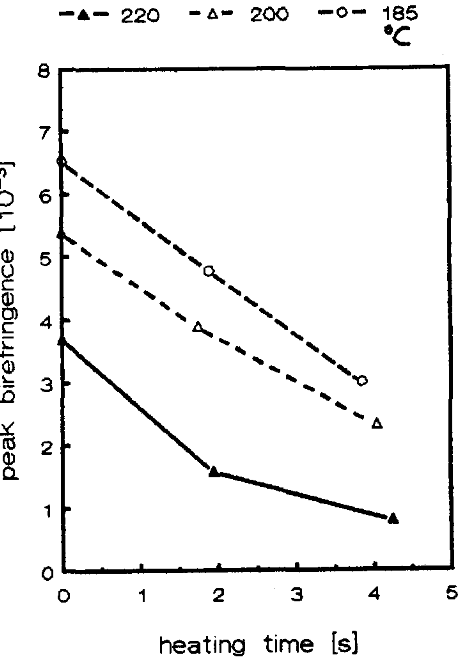

fig.5.30: Effect of heating time on peak birefringence at several temperatures.

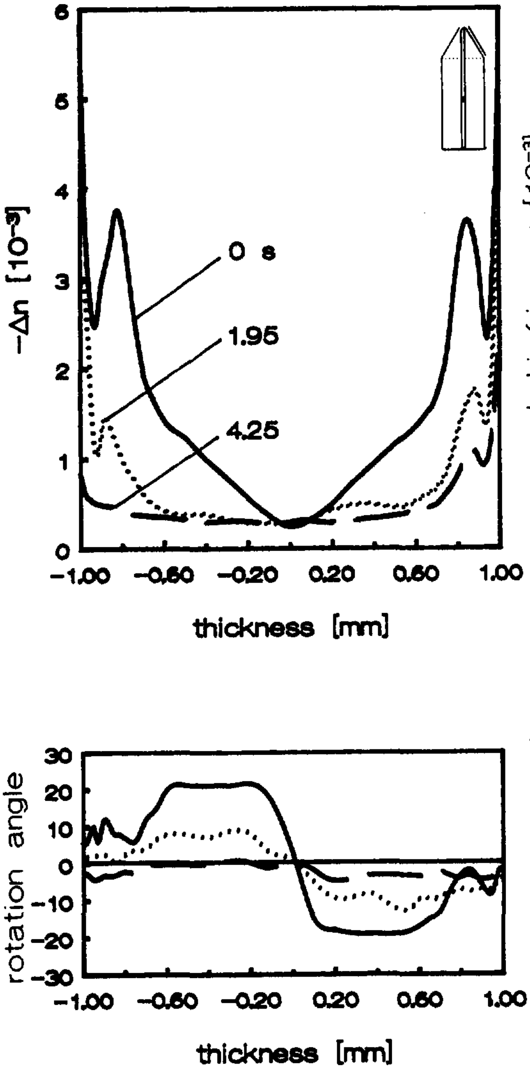

fig.5.29: Effect of heating time on birefringence distributions at 220 °C. (series A220, D220 and E220)

As was expected the heating time exerts a strong influence on the frozen-in birefringence. Fig.5.29 shows that a heating period of about 4 seconds is able to eliminate the shear maximum . The remaining birefringence level $(\Delta n \approx -5.10^{-4})$ is probably due to the effect of shrinkage during solidification (Wimberger-Friedl (1991), §3.3). Figure 5.30 shows that the peak maxima of the experiments at 185 °C, 200 °C and 220 °C steadily decrease with increasing heating time. The same observation can be made concerning the rotation angle (bottom part of fig.5.29).

In fig.5.31 the measured birefringence distributions of fig.5.29 are compared with numerical simulations. Most of the details concerning the simulation are given by Flaman (1990). In contrast to that publication, figure 5.31 contains calculations with a different, more accurate value of the pressure dependence of the viscosity. As can be seen an excellent agreement for the standard experiment was obtained. However, the influence of the heating time in the simulations is much lower than was observed. This is thought to be due to the fact that the heater was modeled as a single layer with a uniformly distributed power density. In this way the heat flux into the polymer was systematically underpredicted, resulting in too high an orientation level.

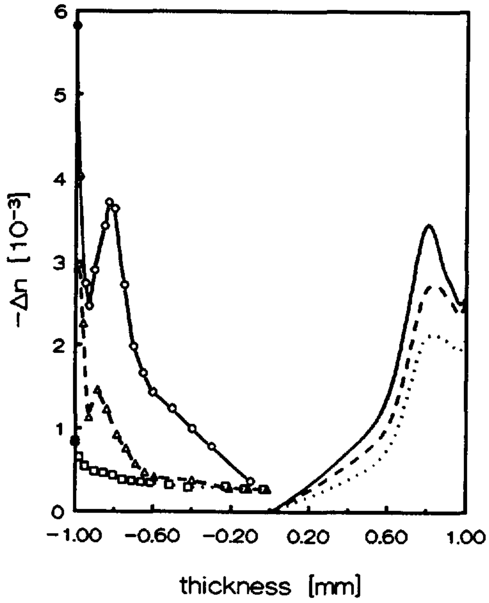

fig.5.31: Comparison between experimental (left, symbols) and numerical predictions (right) of the birefringence distribution of experiments A (-o-), D (-Δ-) and E (-□-) at 220 °C.

The effect of the heating power on the peak orientation (fig.5.32) seems to be strongly non-linear at first sight. However, after taking into account more measurements (at different axial positions), a more gradual dependency shows up, which is in better accordance with the predictions of eq.(4.11) (see fig.5.33). The scatter in fig.5.33 is due to temperature fluctuations at

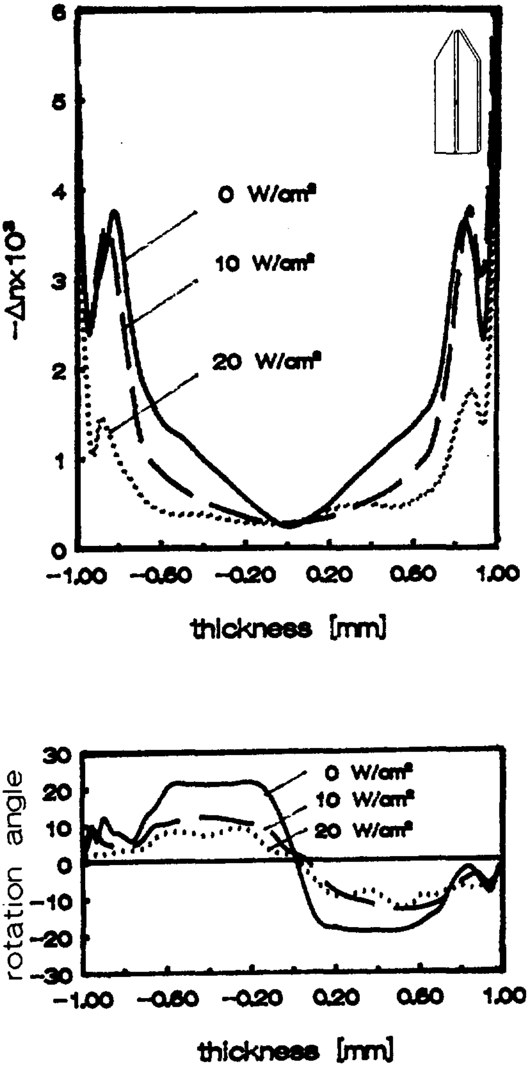

fig.5.32: Effect of power density on birefringence distributions at 220°C. The effects on the rotation angle are shown below.

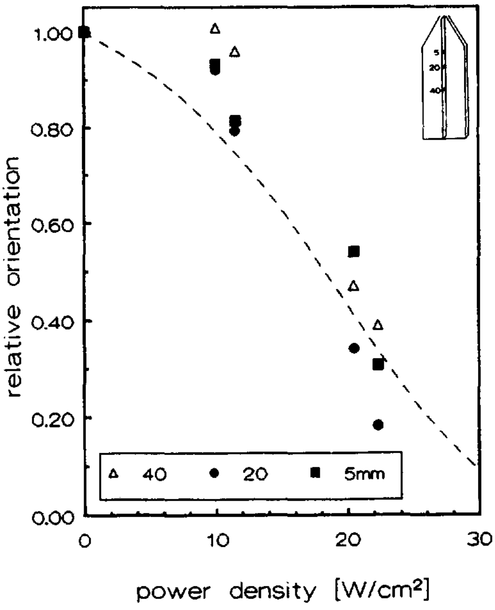

fig.5.33: Effect of power density on peak birefringence at 220 °C. The dotted line represents the expected curve (eq.4.11) ■, ● and △ denote measurements at z=5,20 and 40 mm respectively.

the heater surface. Note that we used the small difference in power density between the two mould halves to obtain several extra data points.

We therefore may conclude that the observed sharp decrease of peak birefringence for $P_A > 10$ W/cm^2, z=40 mm, is probably due to the scatter in local power density rather than a sudden increase in orientation relaxation.

The last heating parameter investigated is the delay time. As is shown in fig.5.34, the delay time certainly influences the relaxation process. If the

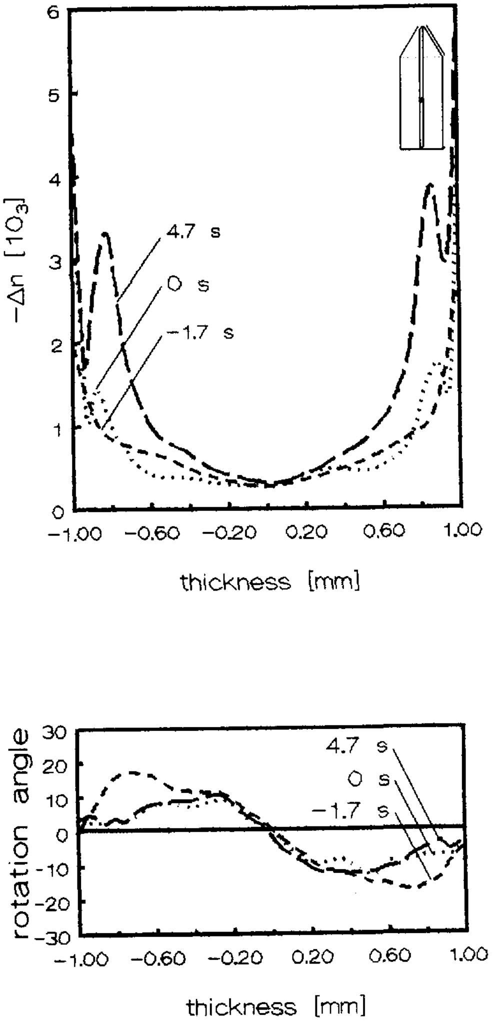

fig.5.34: Effect of delay time on birefringence distribution at 220 °C. (series F ,D and G). The effect of the rotation angle is shown below.

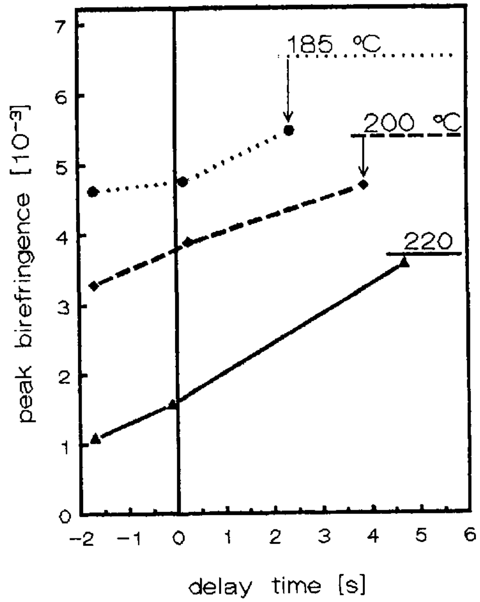

fig.5.35: Effect of delay time on peak birefringence at different T_{in}. The initial peak heights are also indicated.

heating pulse is applied during the packing stage almost no relaxation seems to occur, whereas heating during filling proves to be the most effective way to remove all orientation. Note that in this case even the local birefringence maximum near the product surface decreases considerably. A plot of the peak maxima as a function of t_d for the three different temperatures (see fig.5.35) at first sight suggests an almost linear increase of orientation with increasing delay time. On the other hand, the considerations outlined in paragraph 4.2.2 indicate the existence of a minimum birefringence near t_d=-1 and a rather sharp increase near t_d=0. These suggestions are not contradicted by the present experiments. However, in order to throw more light on this subject, more experiments with different delay times are needed.

5.4.7 Interpretation of the results

To summarize the results of the orientation measurements we can say that for our experimental system

- A passive insulation layer is not capable of decreasing the amount of frozen-in orientation;
- Heating during filling does not have much influence on the pressure needed to fill the cavity;
- Power densities of about 15 to 20 W/cm^2 are needed for effective orientation relaxation;
- Most of the orientation relaxes during the first second (if applied during the first stage of the cooling process);
- It is easier to prevent the formation of frozen-in orientation, than to try to relax it after being frozen-in;
- The most effective heating period is that which includes the filling stage;
- It is possible to decrease the orientation maximum with a factor 3 to 5 by using a 20 W/cm^2 heating pulse;
- Such a heating pulse also decreases the orientation which is frozen-in during the holding stage.

These observations can easily be explained by considering the temperature curves of the different experiments (fig.5.36). Here we plotted the calculated temperatures in the polymer, 0.2 mm under the surface, as a function of time (the corresponding equations are derived in chapter 2). The 140 ^{o}C -line is regarded as a lower limit below which the relaxation process becomes to slow to proceed. This seems more or less plausible since the

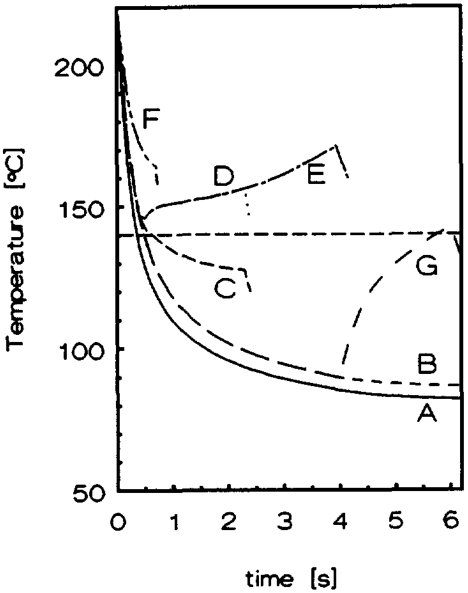

fig.5.36: Heating curves at x_1=0.2 mm of all different experiments (T_{1n}=220 °C). The letters represent the corresponding experiments.

longest relaxation time changes from about 70 to over 1000 seconds between 150 and 130 °C (§5.3.1) for 1 atm. (Note that due to dissipation and pressure effects the real relaxation times are probably much lower). Only the experiments where the temperature after heating exceeded the 140 °C -line showed a noticeable orientation relaxation. Further, it becomes clear why experiments C220 and G220 were on the verge of being effective and why the passive layer experiment (B) did not show much improvement relative to the standard experiment (A).

As a rule of the thumb, we further may state that the orientation relaxation is more or less proportional to the area above the limiting temperature: the larger the area above 140 °C, the more relaxation. However, one has to be careful with this last interpretation since the relaxation process is much more effective at higher temperatures. In chapter 4 this is worked out in a more quantitative way (eq.(4.11)). Experiment F supplies an example of this non-linearity since it has an effective heating time of only 0.7 seconds, but shows almost the same orientation relaxation as experiment D (with an effective heating time of 2 seconds).

The principle expressed above can also be applied to predictions for other materials. Obviously, one has to be very careful in selecting the discriminative temperature level. This level should be chosen such, that the local orientation relaxation time is of the same order as the orientation formation time (usually several tenths of a second). The relaxation time has to be corrected for pressure and viscous heating and compression heating influences.

5.5 Stress measurements

As was shown in the introduction, an injection moulded product not only possesses a very non-uniform orientation distribution, but also the internal stresses formed during the moulding operation are far from homogeneous. This section deals with the measurement of such stresses and the effect of a short heating pulse during the moulding process on those stresses. As a measurement method the so-called Layer Removal Method was chosen. The errors involved with this method are rather large (5 to 10%), but to date there does not seem to be an alternative method for measuring a stress distribution in polystyrene strips more accurately (a short review on stress measurement methods is given by Isayev (1987) p.257 ff).

5.5.1 The Layer Removal Technique

The Layer Removal Analysis provides a method to measure the residual stress distribution in a rectangular specimen of at least 10 cm long. In this analysis thin layers of uniform thickness are removed from one surface, thus disturbing the existing stress distribution. To re-establish equilibrium the specimen warps to a shape which closely resembles a circular arc. The measured curvatures as a function of depth can be used to calculate the stress distribution prior to layer removal.

Curvature-stress relation

The relation between the curvature and the stress distribution was first derived by Treuting and Read (1951). They assumed linear elastic material behaviour and a uniform modulus of elasticity, E. Furthermore, the stress was not allowed to vary in the plane of the specimen but only through the thickness. From the momentum balance in the strip they obtained after some algebraic manipulation an expression for the stress distribution in the z direction, σ_{zz}, as a function of the removed distance, x_r:

$$\sigma_{zz}(x_r) = \frac{E}{12(1-\nu_p^2)}\left(x_r^2.\frac{\partial\kappa^*}{\partial x_r} + 4x_r\kappa^*(x_r) - 2D.\kappa_0 \right) \qquad (5.11)$$

with

$$\kappa^*(x_r) \equiv \kappa_z(x_r) + \nu_p\kappa_y(x_r), \qquad (5.12)$$

$$\kappa_0 \equiv \kappa^*(2D)$$

The stress component in y-direction is given by eq.(5.11) with the subscripts y and z in κ^* interchanged. Note that uniaxial and biaxial stress distributions are special cases of eq.(5.11). In the first case, σ_{yy} and κ_y vanish, whereas in the second case $\sigma_{zz}=\sigma_{yy}$ and $\kappa_z=\kappa_y$. It is not difficult to show that the difference between an initially uniaxial or initially biaxial stress distribution is only reflected in the front factor of eq.(5.11).

In our case we cut our sample of 70x18x2 mm^3 from the mid section of the rectangular part of the product. Therefore, the stress distribution will still be more or less biaxial and only measurements in one direction are necessary (some experimental evidence for biaxiality is given by e.g. Isayev (1987) and Schennink (1990)).

Modifications of standard procedure

As was already said, the theory was originally developed for ideal elastic materials. However, polymer materials have a visco-elastic nature, which means that it is able to show stress relaxation and creep during the measurements and sample preparation. It is therefore advised to (Isayev 1987, Schennink 1990):

1 Store the products at low temperature (-18°C) between the moulding process and the sample preparation. In this way stress relaxation is effectively inhibited;

2 Use a sharp cutter at high speed during the removal of the subsequent layers in order to prevent undesired deformations and local heating. We used a Reichert-Jung Ultra milling machine with a diamond cutter at 1250 rpm. Schennink (1990) showed that under these conditions no additional stresses are introduced;

3 Measure the curvature as soon as possible after the milling operation in order to prevent unwanted deformation of the strips by creep. In our case, the curvature measurements were performed two minutes after the milling operation.

Furthermore, after each 7 or 8 layer removals a fresh strip was taken.

The evaluation of eq.(5.11) further demands some special care. Most of the errors involved with the layer removal method are due to the surface roughness which causes errors in the curvature distribution. The effect on the derivative in eq.(5.11) is considerably worse. These errors can be avoided partly by using the curvature difference ($\kappa-\kappa_0$) as an input value for eq.(5.11). Also the evaluation of the curvature data itself is not unambiguous. If the curvature differences versus the removed distance are fitted with a polynomial curve, the resulting stress profiles appear to be highly dependent on the polynomial degree chosen. Therefore a sliding-central-point smoothing procedure was developed, using a filter window of N_w points. Inside each window a least-squares polynomial fit is used to evaluate the central point. After that the window shifts one point to the right. As is known from Proctor and Sherwood (1980), N_w is best chosen to be approximately equal to the width of the specific peak at half height. They further suggest the polynomials to be quadratic or cubic. More details of the fitting procedure are given in Jansen and Flaman (1992b).

Curvature measurements

The curvature is in fact calculated from measurements of the height of deflection of the strip (h) as a function of the axial sample coordinate, z_s (see fig.5.37). A convex curvature is designated as positive. The height of deflection at the centre of the sample, h_0, is most suitable for calculating the curvature, κ:

$$\kappa = \frac{2h_0}{(L_c/2)^2 + h_o^2} \cong 8h_0/L_c^2 \qquad (5.12)$$

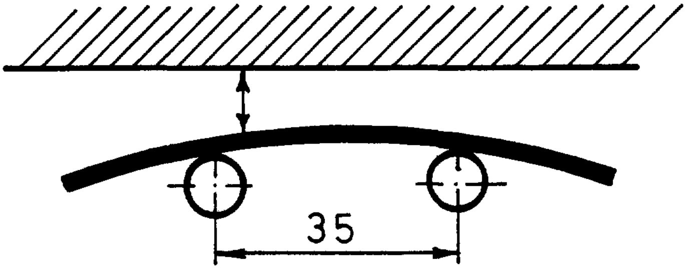

fig.5.37: Height measurement at a curved strip supported by two steel rods which are fixed at a distance L_c=35 mm.

5.5.2 Effect of heating elements on stress distribution

The measurements were performed on strips of series A200 (Standard series) and G200 (2 seconds heating in the holding stage). The reproducibility was checked by comparing the stress distribution of series A200 with the distribution of series PS55 as published by v. Hastenberg et al. (1992) (identical moulding conditions). The absolute error in the calculated stresses turned out to be about 0.25 MPa (relative error: 8 or 9%).

As can be seen from fig.5.38 the heating pulse reduced the wall stress and the compressive minimum by about a factor 2. The stresses in the core, however, virtually remained unchanged.

The interpretation of the effect of the heating element in terms of the formation pressure (see section 4.4) is rather difficult since partial stress relaxation occurs as the surface layer is remelted by the heating pulse. Furthermore, adhesion to the mould wall is not assured and slippage of the molten layer is likely to occur. For longer heating periods, however, most of the built-up stresses relax and an ab-initio start of stress formation after the heating pulse seems justified.

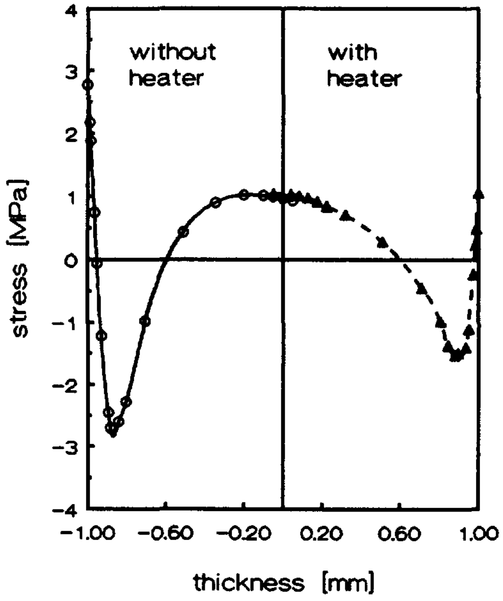

fig.5.38: Measured stress distribution of series A200 (solid line) and G200 (dashed line).

As follows from fig.5.39, the pressure in the cavity after the heating pulse is about 40% of the holding pressure peak. This indicates that, in case of an ab-initio start, the formation pressures are at least 40% lower than in the standard situation. According to the theory of section 4.4 the difference between the surface stress and the compressive stress minimum should be proportional to the maximum cavity pressure. These stress differences are for experiment A200: (2.8- -2.8)=5.6 MPa and for experiment G200: (1- -1.5)=2.5 MPa. Thus the measured stress difference decreased with a factor 2.2, which is about 45%. This supports our assumption of (almost) complete stress relaxation after heating. In contrast to this hypothesis, however, is the (small) tensile component which is still present at the surface. A possible explanation is that the adhesion to the wall is re-established shortly after the heating pulse.

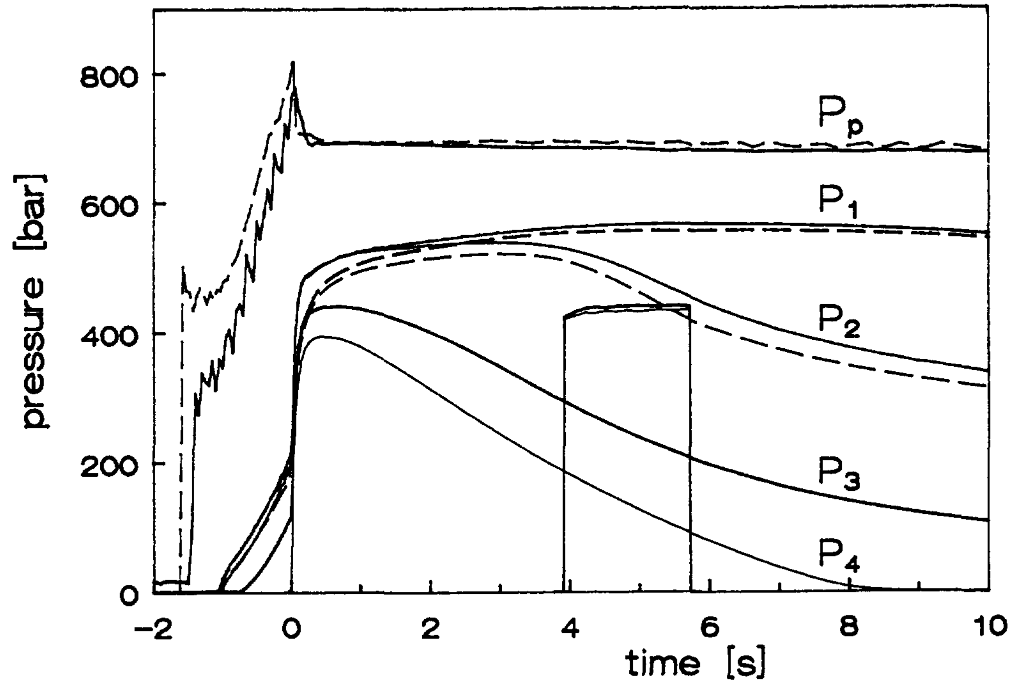

fig.5.39: Recorded pressure curves of experiment A200 (solid lines) and G200 (dashed lines). The heating pulse of G200 (in W/23 cm^2) is also included.

It is of some interest to speculate what would happen with the stress distribution if the heating pulse were applied during and shortly after the filling stage. In that case the polymer is still in its molten phase when the sharp pressure rise occurs. The stress build-up will start near the holding pressure peak and the formation pressure will gradually decrease from the mould wall towards the centre. This means that the stress distribution will have a parabola like shape and will be compressive at the surface and tensile in the core. Such a stress distribution is highly desired since compressive surface stresses suppress the sensitivity for environmental stress cracking. There is however the possibility that due to the re-establishment of adhesion to the wall, the compressive surface minimum will not be as low as expected. Further measurements or calculations are necessary to throw more light on this question.

The theory of chapter 4 (eq.(4.23)) enables a more quantitative analysis on stress formation in combination with heating elements. In that case we would need a cavity pressure curve an a solidified layer growth curve. As a first approximation a measured cavity pressure curve seems to be sufficiently accurate (remember that the pressure curves are hardly influenced by the heating elements (figs.5.17, 18 and 19)). Further, the layer growth curve is best calculated with a numerical or analytical model. Although of interest, no attempt has been made yet to perform these calculations.

Acknowledgements

The author gratefully acknowledges the many people of the Philips Research Laboratories who helped with the construction of the heating cells. AKZO Chemicals and Dupont Nemours kindly supplied the electrical conducting resin and the polyimide foils respectively. The rheological measurements were performed by B. Norder (TU Delft). The author further wishes to thank R. de Zwart and A.A.M. Flaman for their help with the injection moulding experiments and H. van Vlerken for the careful preparation of the birefringence cross sections. The Layer Removal measurements were performed by the following people of Philips PMF: C. v.Hastenberg, G. Schennink, L. Plessers and P. Wildervank.

This work was part of the IOP PCBP program of the Dutch Ministry of Economic Affairs.

CHAPTER 6

GENERAL CONCLUSIONS

What is most important for injection moulders and product engineers is to understand how the processing step influences the ultimate product properties. Since the solidification process can be considered as the driving force for non-uniformities in the orientation, stress and density state of the as-moulded product, first a detailed study of the heat transfer process was undertaken (summary in section 6.1). With the thus obtained knowledge the link between the injection moulding process and (some of) the properties of the finished part could be made (summary in section 6.2).

Experimentally it was tried to control the heat transfer such that the product quality improved (less orientation and residual stresses) without having much effect on the cycle time. For this purpose a new kind of fast-response heating elements was developed which turned out to work quite well (section 6.3).

6.1 Conclusions concerning heat transfer models

The first part of this thesis aims at the understanding of the heat transfer during injection moulding. This was done in a systematic way. Here we will only summarize the most important results.

A closed form expression was obtained for the steady state temperature distribution during the filling stage, using a perturbation technique (§3.1). This technique also allowed us to calculate the effects of viscous dissipation and compression heating on the temperature distribution (eqs.3.7 and 3.17). Comparison of (some of) these solutions with more extensive numerical solutions shows a reasonable agreement. Furthermore, with a suitable transformation (eq.3.21), the solutions for a simple rectangular cavity can be used to describe the heat transfer for arbitrary diverging flow situations.

These steady state solutions were used as a starting point for an approximate derivation of the instationary heat transfer during filling (§3.2.2). This analysis yields a useful estimate of the moment after which the instationary effects vanish (eq.3.37). Furthermore, model predictions for the instationary solidified layer thickness (eq.3.39) were found to agree reasonably well with experimental data (§3.2.4).

As was shown in section 3.3, the variation of the temperature in the flow direction rapidly vanishes after the filling stage. Therefore, the final cooling stage of a part with uniform thickness is almost identical at each axial position.

In addition to the cooling in a standard injection moulding situation, we also studied the effect of an insulation layer and a thin heating element between mould and melt (§2.2 and 2.3). The analytical solutions in the quiescent melt limit compare well with both exact numerical solutions and actual temperature measurements. The expressions for the effect of an insulation layer (or a heating element) on the cooling time (eq.2.21) and the heater surface temperature (eq.2.25a) lead to important heater design criteria (§5.1).

6.2 Conclusions concerning effects of processing history on product quality

In section 4.2 the effect of a heating element on the orientation relaxation process was studied. This resulted in a semi quantitative model (eq.2.25a) which compared well with experimentally obtained data.

Further, in sections 4.3 and 4.4 attention was paid to residual stresses arising during polymer processing. Injection moulding is an example of a constrained quenching process with varying melt pressure. It was shown that in case of the simple, but physically relevant, elastic-solid model no residual stresses arise due to constrained quenching. Therefore, in injection moulding, the melt pressure history is the most important source of residual stresses. This resulted in a simple analytical expression (eq.(4.23)), which turned out to excellently predict the shape of the the residual stress distribution. The magnitude of the predicted stresses, however, was about a factor two too high in comparison with the measured stresses. As an example, the stress distribution was used to calculate the warpage due to a small temperature difference over the thickness (eq.4.27). It turned out that this warpage was much less than warpage due to free quenching (eq.(4.19)).

6.3 Conclusions concerning experimental results with heating elements

The experiments described in chapter 5 of this thesis aim at investigation of the effect of changes in the heat transfer (viz. insulation layers and heating elements) on the product properties (such as the orientation distribution). As was shown in §5.2 the heating elements were fast enough to be of practical importance. When compared with other heaters reported in the literature, it shows that our heating elements were actually about 10 times faster in heating and cooling. A typical heating curve, measured at the heater surface, shows a heating (or cooling) rate of about 350 ^{o}C/s during the first 0.2 seconds and about 15 ^{o}C/s afterwards.

For the specific injection moulding conditions (see §5.3) and material (PS 678E, Dow Chemicals) it was found that:

- there is no effect of a (0.1 mm thick) insulation layer on the orientation distribution;
- the effect of an insulation layer or a heating element on the filling pressure is negligibly small;
- however, heating pulses of about 20 W/cm^2 during 2 seconds, show a large effect on the orientation relaxation (about a factor 3 or 4);
- such a heating pulse reduces the residual stresses near the product surface with (at least) a factor of about 2;
- a heating pulse applied during the filling stage has the largest effect on the orientation relaxation;
- a heating pulse of 10 W/cm^2 appears to be too weak to cause orientation relaxation;
- a heating pulse of 4 seconds (20 W/cm^2) removes almost all frozen-in orientation;
- (small) temperature inhomogeneities at the heater surface somewhat disturb the uniform orientation relaxation;
- the experiments did not give a clue to the (long term) wear resistance of the heater surfaces, nor were they suited to show the effect on the cooling time.

Note that the use of the surface heating elements used is not restricted to applications which benefit by the reduction of frozen-in orientation and stresses (as was the main research objective here). Other application are for example: improvement of surface quality of foamed and fiber filled products; increase of flow length; injection moulding of thin products; reduction of weld lines; separation of (hot) injection stage and (cold) cooling stage; moulding with shorter cycle times and equal (or improved) product quality (lower mould temperatures increase the cooling process while surface heating during filling controls the product quality).

6.4 Checks for numerical models

Nowadays, numerical simulation programs are quite popular in the field of polymer processing. They are flexible with regard to geometry, boundary and inlet conditions and comparison with experimental observations is easily achieved by a suitable choice of the constitutive equation. However, because of the large flexibility, the testing of such programs becomes a major task. Here the analytical solutions, obtained for several limiting cases, are indispensable.

Further, if one decides to rely upon existing numerical codes rather than writing them oneself, it is often difficult to obtain an unprejudiced judgment of the performance of these codes.

The aim of this section, therefore, is to list a few, relatively simple, tests which are useful for checking the heat transfer part of numerical programs. One should be aware that, although some of the tests seem to be self-evident, they are not always passed by commercially available simulation packages. It is recommended to start testing with simple geometries such as a line-gated rectangular cavity or a circular pipe.

1 The solidified layer thickness can never exceed the one given by eq.(2.7) (requirements: constant thermal parameters λ, ρ, c_p and uniform initial temperature). All other contributions to the energy equation (convection, viscous dissipation or other heat sources) tend to increase the temperature and thus to decrease the solidified layer growth. If the wall temperature increases with time because of the finite thermal conductivity of the mould the solidified layer growth is also suppressed.

2 The solidified layer thickness is (to a good approximation) proportional to $(T_s-T_w)/(T_{in}-T_w)$ (requirements: D_s not too large, T_w constant and constant thermal conductivity in the solidified layer). This even holds in the instationary case and for a temperature dependent viscosity. In the limiting case as discussed in section 3.1 (steady state and constant thermal parameters, wall/initial temperature and viscosity), deviations from the proportionality can be calculated with eq.(3.14).

3 The difference between the steady state temperature field during channel flow and that during pipe flow is always positive and is given by eq.(3.19). Near the wall ($\hat{r}\ll1$) it should apply that

$$\tilde{T}^{\mathrm{channel}} - \tilde{T}^{\mathrm{pipe}} = \frac{\hat{r}}{2}\left(1 + \frac{\varepsilon}{2}\left(\frac{\alpha-1}{10} + \frac{1}{2} + \frac{1}{8\Gamma(4/3)}\right)\right) + \frac{1}{2}\hat{r}^2\left(\frac{\alpha-1}{10} + \frac{1}{2} + \frac{1}{\varepsilon\Gamma(4/3)}\right) + O(\hat{r}^3/\varepsilon)$$

4 Numerical programs are usually applied to geometries which are more complex than a simple rectangular or cylindrical shape, whereas analytical solutions are (mostly) only available for those simple cases. In case of steady state heat transfer, however, the solution of the temperature field in a diverging channel should follow the theory of §3.1.6 (requirements: temperature independent viscosity and thermal parameters, small angle of divergence, constant wall temperature and pressure drop). This probably also holds for transient situations and non-power-law fluids.

5 The temperature profile after complete solidification should decay exponentially since the higher order terms in eq.(3.44) soon vanish. (requirements: $t>D^2/a$, constant thermal parameters and wall temperature).

6 A numerical simulation of the effect of a heating element on the temperature field (based on the set of differential equations (2.10) and (2.24)) should satisfy eq.(2.36). This even holds if convection and dissipation terms are present (requirements: temperature independent thermal parameters, viscosity and heat source).

REFERENCES

Abramowitz M, Stegun IA (1972) Handbook of mathematical functions. Dover, New York

Alles H, Philipon S, Agassant JF, Vincent M (1986) Experimental and theoretical study of the filling stage of a rectangular plaque: application to a spiral mold, Pol Proc Eng 4:71-96

Bird RB et al. (1987), Dynamics of polymeric liquids; Vol.I Fluid mechanics, 2nd ed., Wiley and sons New York.

Baaijens FPT (1991), Calculation of residual stresses in injection molded products. Rheol Acta 30:284-299

Buchholz H (1953) Die Konfluente Hypergeometrische Funktion. Springer, Berlin p.37 Wales JLS (1972) Some aspects of orientation in injection moulded objects. Polym Eng Sci 12:358-363

Carslaw HS and Jaeger JC (1988), Conduction of heat in solids, 2nd ed., Ch. 12.8, Oxford Science Publications, Clarendon Press, Oxford

D'Ans Lax (1967), Taschenbuch für Chemiker und Physiker, Band 1, 3. Auflage, Springer Verlag, pp.I-701

Delphy U, Wintergerst S (1972), Spritzgießen mit veränderlichen Werkzeugtemperatur, Kunststoffe 62:209-211

Dietz W et al. (1978), Orientation development and relaxation in injection molding of amorphous polymers, Polym Eng Sci 18:273-281

Douven LFA (1991), Towards the computation of properties of injection moulded products: flow- and thermally induced stresses in amorphous thermoplastics. PhD thesis, Eindhoven Technical Univ

Ehringhaus A (1938), Ein Drehkompensator aus Quartz mit großen Meßbereich und bei hoher Meßgenauigkeit, Z Kristallogr 38:394-406

Feynman RP et al. (1989), The Feynman lectures on physics: commemorative issue. Addison-Wesley publ company, California

Flaman AAM (1990), Build-up and relaxation of molecular orientation in injection moulding. PhD Thesis, Eindhoven Technical Univ

Flaman AAM and Jansen KMB (1993), The influence of surface heating on the birefringence distribution in injection moulded parts, Polym Eng Sci (To be published)

Goslinga J (1980), The determination of residual stresses in plastics pipes. PhD Thesis, TH Twente

Greener J (1986), Pressure-induced densification in injection molding. Polym

Eng Sci 26:534-542.

v. Hastenberg CH et al. (1992), The measurement of thermal stress distributions along the flow path in injection-molded flat plates, Polym Eng Sci 32:506-515

Isayev AI ed. (1987), Injection and compression molding fundamentals, Marcel Dekker, New York

Janeschitz-Kriegl H (1977), Injection mouldig of plastics: some ideas about the relation between mould filling and biregringence, Rheol Acta 16:327-339

Janeschitz-Kriegl H (1979), Injection mouldig of plastics. II Analytical solution of heat transfer problem, Rheol Acta 18:693-701

Janeschitz-Kriegl H (1983), Polymer melt rheology and flow birefringence, Springer Verlag, Berlin

Jansen KMB and van Dam J (1992), An analytical solution for the temperature profiles during injection molding, including dissipation effects, Rheol Acta 31:

Jansen KMB and Flaman AAM (1992a), Reduction of orientation in injection moulded products by means of fast heating elements, Part 1: Heater construction, Nat.Lab. technical note 174/92

Jansen KMB and Flaman AAM (1992b), Reduction of orientation in injection moulded products by means of fast heating elements, Part 2: Injection moulding experiments, Nat.Lab. technical note 175/92

Jansen KMB (1993), Heat transfer in injection moulding systems with insulation layers and heating elements, Int J Heat Mass Transfer (Submitted for publication)

Jansen KMB and Flaman AAM (1993a), Construction of fast response heating elements for injection moulding applications, Polym Eng Sci (Submitted for publication)

Jansen KMB and Flaman AAM (1993b), The influence of surface heating on the birefringence distribution in injection moulded parts. Polym Eng Sci (accepted for publication)

Jansen KMB (1993b), Effect of geometry on steady state heat transfer for laminar flow of power law fluids, Rheol Acta (submitted for publication)

Johannaber F (1985), Injection molding machines: A user's guide. Hanser Verlag, München

Johnson LI (1963), Modern Plast. 40:111

Kim BH, Suh NP (1986), Low Thermal Inertia Molding. Polym Plast Technol Eng 26:23-44

Kim BH, Suh NP (1987), A study of isothermal simple shear flow followed by nonisothermal stress relaxation in a Low Thermal Inertia Molding. Polym Plast Technol Eng 2

Kim BH and Roth C, Critical J-integral value of injection molded polycarbonate using a Low Thermal Inertia Mold. Polym Plast Technol Eng 27:467-485

Kreyszig E (1988), Advanced engineering mathematics, 6th ed, Wiley and Sons, New York

Landau LD and Lifshitz EM (1986), Theory of elasticity (Course of theoretical physics Vol.7 3rd ed), Pergamon press Oxford

Liou MJ (1987), Minimizing residual stresses in molded parts, Ph.D. Thesis Massachusetts Institute of Technology

Luke YL (1969), The special functions and their approximations; Vol.I, Academic Press, New York

Meistner BJ (1989) in: Styrene Polymers, 2nd ed. reprinted from Encyclopedia of Polymer Science and Engineering, Vol.16, Wiley and Sons, p.122

Menges G et al. (1974), Spritzgußwerkzeuge met wärmedämmende Formnestbeschichtigungen, Plast Verarbeiter 25:279

Laven J (1985), Non-isothermal capillary flow of plastics related to their thermal and rheological properties. PhD Thesis, Delft Univ of Technology

Lévêque MA (1928), Les lois de la transmission de la chaleur par convection. Ann mines 13:201,305,381

Newman J (1969), Extension of the Lévêque solution. J Int Heat Transfer 91:177-178

Oberbach K (1980), Kunststoff-Kennwerte für Konstrukteure, Carl Hanser Verlag, Wien

Olver FWJ (1974), Asymptotics and special functions. Academic Press, New York

Pearson JRA, Richardson SM (1983), Computational analysis of polymer processing. Applied Science Publishers, London

Pearson JRA (1985), Mechanics of polymer processing, Ch.19:Injection Moulding. Elseviers Appl Sci Publ, London

Proctor A, Sherwood PMA (1980), Smoothing of digital X-ray photoelectron spectra by an extended sliding least-squares approach, Anal Chem 52:2315-2321

Richardson SM (1979), Extended Lévêque solutions for power law fluids in pipes and channels. Int J Heat Mass Transfer 22:1417-1423

Richardson SM (1983), Injection moulding of thermopastics: freezing during mould filling. Rheol Acta 22:223-236

Ryan ME, Chung TS (1980), Conformal Mapping analysis of injection mold filling. Pol Eng Sci 20:642-651

Schennink GGJ (1990), Thermal stresses in amorphous polymers (in Dutch), Doktoraalverslag, Twente University

Stevenson JF (1976), Heat and mass transfer in radial flow. Chem Eng Sci 31:1225-1225

Struik LCE (1990), Internal stresses, dimensional stabilities and molecular orientations in plastics, Wiley and Sons, Brisbane

Throne JL (1979), Plastics process engineering. Marcel Dekker, New York

Titomanlio G, Drucato V and Kamal MR (1987), Mechanism of cooling stress build-up in injection molding of thermoplastic polymers, Intern.Polymer Processing 1:55-59

Treuting RG and Read WT (1951), A mechanical determination of biaxial residual stress in sheet materials, J Appl Phys 22:130-143

Van Wijngaarden H, Dijksman JF, Wesseling P (1982) Non-isothermal flow of a molten polymer in a narrow rectangular cavity. J Non-Newtonian Fluid Mech 11:175-199

VDMA (1986), Kenndaten für die Verarbeitung thermoplastischer Kunststoffe: Thermodynamik, Hanser Verlag, Munchen

Wadhwa RR, Kim BH (1988), Experimental results of LTIM. I length of filling, Polym Plast Technol Eng 27:509-518

Wales JLS (1972), Some aspects of orientation in injection moulded products. Polym Eng Sci 12:358-363

White JL (1979), Some relations between injection molding conditions and the characteristics of vitrified molded parts, Polym Eng Sci 19:558

Wimberger-Friedl R (1990), Analysis of the birefringence distributions in compact disks of polycarbonate, Polym Eng Sc 30:813-820

Wimberger-Friedl R (1991), Orientation, stress and density distributions in injection-moulded amorphous polymers determined by optical techniques, PhD Thesis Eindhoven Technical University

Wu JP and White JL (1991), Study of birefringence character of injection- and compression-molded polycarbonate and its interpretation, Polym Eng Sci 31:652-660

Wübken G (1974), Einfluß der Verarbeitungs Bedingungen auf der innere Struktur thermoplastischer Spritzgußteile ..., Ph.D. Thesis Aachen

Zonneveld R (1969), Internal TNO report nr.KRI202/'69

SUMMARY

Injection moulding is an important industrial process for manufacturing thin walled polymer products. During this process plastic granules are melted and injected into a cold mould. The combined flow and cooling during the injection stage produce a thin subsurface layer which contains a relatively high amount of frozen-in orientation. In addition, the solidification in combination with the pressure history causes a far from uniform residual stress distribution. Both effects affect the quality of the moulded product and are often undesirable.

The aim of this thesis is to understand and control the heat transfer during the moulding process.

In order to reduce the frozen-in orientation and residual stresses, both thin insulation foils and active heating elements may prove helpful. The effects of these alternatives on the temperature history are discussed in chapter 2.

Chapter 3 discusses the effect of the polymer flow on the heat transfer. Several expressions are derived for the contributions of viscous dissipation, compression heating and cavity geometry on the temperature profiles during injection moulding. For the most relevant solutions some easy to use approximations are given.

The results of chapter 2 are used in chapter 4 to estimate the effect of the heating elements on the orientation relaxation. In chapter 4 it is furthermore shown that residual stresses in injection moulded products are of a different origin than stresses in extruded products, resulting in markedly different warpage behaviour.

In the experimental part, chapter 5, the effects of thin insulation layers and fast-response heating elements on the frozen-in orientation distribution in moulded products are studied. The effect of the insulation layers appears to be negligibly small. The heating elements, which were especially designed for application in injection moulding machines, follow the heating characteristics as predicted in chapter 2. Both the heating up and the cooling down of the heaters appear to be extremely fast (80 ^{o}C temperature difference in the first 0.3 seconds). Therefore, the effect of such heating elements on the total cycle time is small, which is rather important from a

practical (or economical) point of view. Furthermore, with a heating pulse of two seconds the orientation maximum is seen to decrease by about a factor of 3, while for the residual surface stresses the reduction is about a factor of 2. This seems to be sufficiently high to ensure the desired improvement in product quality.

SAMENVATTING

Spuitgieten is een veelgebruikte techniek om polymeergranulaat tot een bruikbaar produkt om te vormen. Bij dit proces wordt het granulaat eerst opgesmolten en vervolgens in een gekoelde matrijs gespoten. Tijdens het inspuiten wordt dus al een stollaag gevormd. In deze oppervlaktelaag blijkt een veel grotere hoeveelheid oriëntatie te worden ingevroren dan in de kern. Behalve deze anisotropie in de oriëntatie resulteert het stollingsproces (in kombinatie met het drukverloop) ook nog in een inhomogene spanningsverdeling. Beide effekten hebben over het algemeen een nadelige invloed op de kwaliteit en levensduur van het produkt.

Doel van dit onderzoek was dan ook het afkoelproces (en dan met name de stollaagvorming) beter te begrijpen en aktief te beïnvloeden.

Beïnvloeding van het afkoelproces is mogelijk met een dunne, warmteremmende laag op de matrijswand of met een klein, snel werkend verwarmings-elementje. Het effekt van beide alternatieven op het temperatuurverloop wordt in hoofdstuk 2 behandeld.

In hoofdstuk 3 wordt wat preciezer ingegaan op het effekt van de stroming op de warmteoverdracht. Zo worden uitdrukkingen afgeleid voor de effekten op de temperatuurprofielen van de viskeuze opwarming, kompressiewarmte en de geometrie. Voor de meest relevante oplossingen is steeds geprobeerd een eenvoudig te hanteren benadering te vinden.

Met behulp van de kennis uit hoofdstuk 2 worden in hoofdstuk 4 enige voorspellingen gedaan over het effekt van verwarmingselementjes op de oriëntatierelaxatie. Ook op de vorming van inwendige spanningen wordt uitvoerig ingegaan. Het blijkt dat de restspanningen in spuitgietprodukten volgens een wezenlijk ander mechanisme ontstaan dan in b.v. geëxtrudeerde produkten. Ter illustratie wordt het kromtrekken ten gevolge van inhomogeen koelen voor beide processen doorgerekend.

In het experimentele deel, hoofdstuk 5, wordt beschreven wat het effekt is van dunne, warmteremmende lagen en verwarmingselementjes op de ingevroren oriëntatie in spuitgietprodukten. Het effekt van de passieve lagen blijkt verwaarloosbaar klein. De verwarmingselementjes, die speciaal voor deze toepassing ontworpen zijn, blijken precies op te warmen volgens de in hoofdstuk 2 afgeleide formules. De snelle respons (80 ^{o}C in de eerste 0,3

sekonden) zorgt ervoor dat het effekt op de cyklustijd gering is, hetgeen van groot ekonomisch belang is. Met een verwarmingspuls van slechts 2 sekonden vermindert het oriëntatiemaximum met ongeveer een faktor 3, terwijl de inwendige spanningen in de oppervlaktelaag met een faktor 2 afnemen. Dat lijkt ruim voldoende om de gewenste verbetering in de produktkwaliteit te realiseren.

CURRICULUM VITAE

Kaspar Jansen werd op 13 juli 1964 geboren te Oss. Hij behaalde zijn VWO diploma in 1982 aan het Niels Stensen College te Utrecht. Van 1982 to 1987 studeerde hij Scheikundige Technologie aan de Universiteit Twente. Zijn stage volgde hij in Barreiro (Portugal) van april tot juni 1986. Hij hield zich tijdens zijn afstudeerperiode bezig met spontane scheurvorming in gespuitgiete polyetheen kratten. In januari 1988 begon hij aan de Technische Universiteit Delft in de vakgroep TMS met een promotieonderzoek dat leidde tot dit proefschrift. Een deel van zijn promotietijd, namelijk van november 1990 tot november 1991, heeft hij bij het Philips Natuurkundig Laboratorium in Eindhoven gewerkt aan de ontwikkeling van verwarmingselementjes voor het gebruik in spuitgietmachines. Sinds juli 1992 is hij werkzaam als toegepast onderzoeker aan de Technische Universiteit Delft in de vakgroep TMS.

DANKWOORD

Graag wil ik op deze wijze iedereen bedanken die op enigerlei wijze heeft bijgedragen aan het tot stand komen van dit proefschrift.

Met name noem ik daarbij Paul van der Schoot voor zijn kritische opmerkingen en de vele waardevolle diskussies. Jaap van Dam en Abe Posthuma de Boer ben ik zeer erkentelijk voor hun hulp bij het schrijven van de publikaties waaronder ik ook dit proefschrift reken. Gerard de Vos, Nol van Keeken en Ben Norder wil ik bedanken voor hun hulp bij het opzetten van de spuitgietexperimenten en het uitvoeren van de reologische metingen.

De periode die ik werkzaam ben geweest aan het Philips NatLab heb ik als zeer stimulerend ervaren. Ik wil dan ook graag Ton Flaman bedanken voor zijn begeleiding, Geert Hannen voor het uitvoeren van de warmtegeleidingsmetingen alsmede de vele mensen in de werkplaatsen voor hun hulp bij de konstruktie van de verwarmingselementen. Verder wil ik nog Rene de Zwart bedanken voor zijn hulp bij de spuitgietexperimenten en met name Christ van Hastenberg en Gerald Schennink voor hun hulp bij het doen van de Layer Removal metingen.

Tenslotte wil ik ook nog de firma's Akzo, Dow Chemicals en Dupont Nemours bedanken voor het beschikbaar stellen van de diverse materiaalmonsters.